

One-Dimensional Turbulence: From Extreme Reynolds Number Turbulence to Hypersonic Turbulent Boundary Layers

by

Pranav Nath

A thesis
presented to the University of Waterloo
in fulfillment of the
thesis requirement for the degree of
Doctor of Philosophy
in
Mechanical and Mechatronics Engineering

Waterloo, Ontario, Canada, 2025

© Pranav Nath 2025

Examining Committee Membership

The following served on the Examining Committee for this thesis. The decision of the Examining Committee is by majority vote.

External Examiner: Xiang Yang
Associate Professor, Dept. of Mechanical Engineering,
Pennsylvania State University

Supervisor: Jean-Pierre Hickey
Associate Professor,
Dept. of Mechanical and Mechatronics Engineering,
University of Waterloo

Internal Members: Sean D. Peterson
Professor, Dept. of Mechanical and Mechatronics Engineering,
University of Waterloo

Kyle J. Daun
Professor, Dept. of Mechanical and Mechatronics Engineering,
University of Waterloo

Internal-External Member: Brian McNamara
Professor, Dept. of Physics and Astronomy,
University of Waterloo

Author's Declaration

I hereby declare that I am the sole author of this thesis. This is a true copy of the thesis, including any required final revisions, as accepted by my examiners.

I understand that my thesis may be made electronically available to the public.

Abstract

Turbulence remains one of the most important unsolved problems in classical physics. The difficulty of arriving at a complete understanding of turbulence is rooted in the non-linear and multi-scale nature of the phenomenon. Although fluid mechanical turbulence is governed by the deterministic Navier-Stokes equations, there is no unified theory to obtain a generalized closed form solution for arbitrary turbulent flow configurations. Direct Numerical Simulations (DNS), Large Eddy Simulations (LES) and Reynolds-Averaged Navier-Stokes (RANS) solvers utilize different approaches to arrive at a solution, but each method has complications and limitations of its own.

The description of turbulence as a superposition of coherent structures has provided unique insights into the phenomenon. The possibility of representing turbulence from the statistical and structural viewpoints provides an opportunity to explore models that can provide alternative frameworks combining the features of these two viewpoints.

This work explores the use of dimensionality reduction which couples with a structural and statistical approach to model turbulence. Even though dimensionality reduction is a simplified representation of the complex physical reality, the model retains its usefulness if it captures the essence of the non-linear and multi-scale nature of turbulence. Establishing this simplified model, while retaining the main features of the complex fluid flow, is the primary objective of this work. The one-dimensional turbulence (ODT) method originally proposed by Kerstein [78] is the foundation of this work, which utilizes geometric mapping of properties at multiple spatio-temporal scales in the domain, to represent three-dimensional turbulent eddies. The use of the one-dimensional approach is particularly favourable when the chosen flow configuration exhibits a characteristic direction of variation, which is often the case with the self-similar canonical flows that form the core of turbulence theory.

The developed model builds on the foundational ODT model to address two building block flow configurations of enormous importance in turbulence literature: the homogeneous isotropic turbulence (HIT) and the turbulent boundary layer (TBL). Both of these flows have been the subject of extensive DNS studies, but the extreme computational cost

of the simulations is prohibitive at extreme Reynolds numbers. Extreme Reynolds numbers flows are of paramount importance in many scientific and engineering applications. In addition, the high-Reynolds number simulations are also needed to propose and establish turbulence theory, since idealized turbulence should approach the vanishing viscosity limit.

In this work, we develop a fully-compressible Eulerian ODT solver to study different aspects of canonical high-Reynolds number turbulent flows. This thesis comprises several journal articles, published or under revision for publication at the time of submission of this thesis, that address the following aspects:

- the study of homogeneous isotropic turbulence at high Reynolds numbers up to $Re_\lambda = 5428$, with descriptions of high-order statistics and phenomenology of extreme events,
- an analysis of the key features of one-dimensional turbulence model with the Townsend's Attached-Eddy Model, and
- the study of compressible turbulent boundary layers at hypersonic conditions $M \approx 5.86$, with cold walls at wall-to-recovery temperature ratio as low as 0.26.

The developed methodology shows significant promise in extending the state-of-the-art turbulence simulations to high Reynolds numbers, which is made possible by the computational cost reduction of ODT. The multi-scale nature of ODT captures classical features of homogeneous isotropic turbulence in terms of turbulent energy spectrum, energy flux spectra, normalized dissipation rate and intermittency characteristics. Identifying the salient aspects of Attached-Eddy hypothesis in the ODT model, we establish the importance of probability distribution for eddies alongside the formulations for eddy-induced velocities and displacements. The developed compressible ODT model is also used for prediction of compressible turbulent boundary layer. The model produces the mean statistics of velocity and temperature profiles at hypersonic conditions, agreeing with DNS results, along with the characterization of temperature fluctuations.

Acknowledgements

First and foremost, I would like to thank Prof. Jean-Pierre Hickey for giving me an opportunity to work on turbulence, which I have been most passionate about. The liking towards turbulence was instilled in me while undertaking the course on turbulence taught by him. I thank him tremendously for sharing a wealth of knowledge and expertise in turbulence modelling and providing continuous support during the course of the studies.

I greatly thank all the members of my examining committee for their time invested in reading my thesis. I thank Prof. Sean Peterson for giving me the opportunities to engage with students, which helped me to delve deeper into the concepts of fluid mechanics and keep my research interests invigorated. I am thankful to Prof. Kyle Daun who had inspiring discussions on the mathematical approaches to investigate complex phenomena in the context of inverse analysis.

My sincere gratitude to Prof. Umesh R. Kadhane, who has been a guiding presence over the years. I am deeply thankful for the enriching discussions we have had and for his inspiring passion for both science and life.

I am thankful to my parents, Surinder Nath and Rajni Nath, and to Kavita and Piyush, for their unwavering support throughout this journey. Heartfelt thanks to Shilpa, Athira and Katrine, for their uplifting company, and to Nipin, Jeswin, Annapurna, Ashwini and Ryley, for the memorable trips and support through the years. I deeply appreciate the many enriching discussions with Pablo on philosophy and other topics.

Dedication

This thesis is dedicated to my parents, for their love and support.

Table of Contents

Examining Committee Membership	ii
Author's Declaration	iii
Abstract	iv
Acknowledgements	vi
Dedication	vii
List of Figures	xiii
List of Tables	xix
List of Abbreviations	xx
List of Symbols	xxii
1 Introduction	1
1.1 High-Reynolds number turbulence modelling	2
1.2 Computational cost of state-of-the-art DNS	4

1.3	Dimensionality reduction to model turbulence	6
1.3.1	One-dimensional turbulence	6
1.3.2	Modelling complex flows and compressibility effects in ODT	7
1.4	Scientific contributions of the thesis	9
1.5	Outline of the thesis	10
2	Turbulence in canonical flows	12
2.1	A summary of turbulence characteristics	13
2.1.1	Multi-scale nature of turbulence	13
2.1.2	Characteristics of turbulence	15
2.2	Structural aspects of turbulence	16
2.3	Idealized turbulence - HIT	18
2.3.1	Energy spectra	18
2.3.2	Normalized dissipation rate	20
2.3.3	Structure functions	21
2.3.4	Intermittency	21
2.3.5	Extreme events and stretched-exponentials	24
2.3.6	Substructures in shear layers	25
2.4	Turbulent boundary layers	26
2.4.1	Incompressible TBL profiles	27
2.4.2	Attached-eddy model	28
2.4.3	Wall-scalings in compressible regime	30

3	Methodology	32
3.1	Standard Incompressible ODT model	32
3.1.1	View of the flow from ODT perspective	32
3.1.2	Overall structure of ODT model	34
3.1.3	Basic construct of ODT algorithm	35
3.1.4	Constitution of an eddy event	36
3.1.5	Eddy sampling and acceptance	43
3.1.6	Time-stepping procedure	45
3.1.7	Adaptive meshing	45
3.1.8	Benchmarking with turbulent boundary layer	46
3.1.9	Attempts to introduce compressibility effects to standard ODT	49
3.2	Development of compressible ODT model	49
3.2.1	Inadequacy of standard ODT model	50
3.2.2	Measure-preservation in eddy events	51
3.2.3	Mathematical formulation	51
4	High-order statistics and extreme fluctuations in stationary turbulence via one-dimensional turbulence	56
4.1	Introduction	57
4.2	Model formulation	59
4.2.1	Simplified governing equations	59
4.2.2	Stochastic eddies to model turbulence	63
4.2.3	Generating sustained turbulence	65
4.3	Results	66

4.3.1	Details of simulations	66
4.3.2	Validation and theoretical considerations	69
4.3.3	Reynolds number effects	73
4.3.4	Extreme dissipation events	74
4.4	Compressibility effects	85
4.5	Discussion	87
5	Features of the Attached-Eddy hypothesis in One-Dimensional Turbulence models of turbulent boundary layers	91
5.1	Introduction	92
5.2	Theoretical modelling framework	95
5.2.1	AEM: Eddies at multiple scales	95
5.2.2	ODT: Stochastic turbulence modelling	98
5.3	Application to turbulent boundary layer	102
5.3.1	Capturing the logarithmic mean velocity profile	105
5.3.2	Reynolds stress reconstruction	112
5.4	Discussion	116
6	Predicting the hypersonic turbulent boundary layers with one-dimensional turbulence	119
6.1	Introduction	120
6.2	Model formulation	123
6.2.1	Governing equations	123
6.2.2	Turbulence model	124
6.2.3	Set-up of the ODT simulation domain	128

6.3	Results	129
6.3.1	Mean-statistics obtained at $T_w/T_r \approx 0.73$	130
6.3.2	Prediction of compressible TBL profiles in flows over cold-walls . . .	134
6.3.3	Turbulent energy transport	136
6.3.4	Statistics of fluctuating thermodynamic quantities	138
6.4	Discussion	142
7	Conclusions	145
7.1	Future work	148
	Letters of copyright permissions	149
	References	163
	APPENDICES	184
A	Algorithms for the reduced-ODT model	185
A.1	Mean-velocity profile	185
A.2	Reynolds normal stresses	193
A.3	Reynolds shear stresses with attached eddies	198
A.4	Reynolds stresses with both attached and detached eddies included	203

List of Figures

1.1	Progress in the DNS simulations in terms of Re_λ achieved over the years. The line represents a curve-fit approximation of the maximum Re_λ DNS simulation through the decades.	5
1.2	Schematic of a single clockwise eddy on scalar field that initially has uniform concentration gradient. (a)Initial concentration isopleths (vertical lines) and concentration profile $c(x)$ (heavy line) parallel to the initial concentration gradient. (b) Concentration isopleths and concentration profile after eddy is imposed [77].	8
1.3	Mapping of variable $v(x)$ to represent effect of a turbulent eddy.	8
2.1	Energy cascade from the largest scales L to the smallest scales η , where L_{EI} and L_{DI} demarcate the inertial region from energy-containing and dissipation regions, respectively. P_i refers to the input energy at the largest scales.	14
2.2	Structure of a transverse jet in cross-flow [42].	17
2.3	Evolution of coherent structures in planar wake [53].	17
2.4	TKE spectra at $Re_\lambda = 82$ using the developed model.	20
2.5	Intermittency observed in dissipation-rate variation averaged over the entire domain with time for $Re_\lambda = 929$	22

2.6	PDF of the velocity derivative with stretched tails (solid) compared with a Gaussian PDF (dashed).	25
2.7	Mean-velocity profile (solid) at $Re_\tau = 1000$ from DNS results of Lee and Moser [92]. The dashed line shows the theoretical solution for log-layer from equation (2.17).	27
2.8	Hierarchy of eddies produces the logarithmic layer in AEM.	29
3.1	Linear eddies in ODT representing turbulent stirring for turbulent boundary layer flow with underlying flow represented by dashed arrows. The ODT domain is oriented along the dominant gradient which is in wall-normal direction.	33
3.2	Schematic of ODT method, with specific details pertaining to each block indicated by corresponding section numbers in this thesis.	37
3.3	Triplet mapping in an eddy event. The representation of the eddy in colour scale shows the continuity in the post-eddy velocity profile (blue refers to the minimum and red is the maximum value of velocity).	39
3.4	Normalized mean-velocity profiles from ODT (solid) and DNS results [92] (dashed) with (a) logarithmic and (b) linear z^+	47
3.5	Variation of normalized root-mean-square velocity fluctuations. The positive z^+ values represent the results obtained from the ODT model, while negative z^+ values indicate the DNS results for the turbulent boundary layer. To enhance the intuitive presentation of DNS data, the results are flipped along the vertical axis, resulting in negative z^+ values. DNS results from Ref. [92].	48
3.6	Complications that arise in Lagrangian framework.	50
3.7	Eddy event construction for compressible flows depicted for the case of a turbulent boundary layer.	53
3.8	Sod shock-solution in the compressible model developed.	55

4.1	Triplet-map applied to the variable $q(x)$	64
4.2	(a) Convergence of TKE spectrum with C parameter, and (b) TKE spectrum at $Re_\lambda = 929$ with $C = 10$: —, from ODT, - -, extrapolated and —, theoretical scaling (see equation 4.11).	70
4.3	TKE spectrum with a case with domain size much larger than the forcing length scale at $Re_\lambda = 82$. The energy scaling of different regions, namely, at the region of length scales larger than the forcing length scales (shown by the vertical dashed line at $kL_f = 2\pi$), the inertial and dissipation range are depicted.	72
4.4	(a) Normalized energy spectrum at $Re_\lambda = 218, 355, 491, 929, 1361, 1745$ and 5428 (Re_λ increasing in the direction of the arrow), and (b) normalized dissipation rate D^* (comparative results from Ref.[62]).	75
4.5	Energy-flux spectrum normalized with the mean dissipation rate. Solid lines depict ODT results and the dashed lines represent DNS results from Ref. [62].	76
4.6	Overlapping TKE spectra with an η -normalized coordinate. The green dashed line shows k^{-5} scaling. $Re_\lambda = 5428$ has been shown in grey as it shows slight difference in characteristics from the remaining curves, which may be attributed to the insufficient run-time of the simulation.	76
4.7	PDF of (a) the velocity derivative and (b) dissipation rate.	78
4.8	PDF of the dissipation rate in log-log plots. The vertical axis colors correspond to the respective plotted cases in (b).	79
4.9	Stretched-exponential functions for dissipation rate PDF. Symbols show the stretched-exponential approximations to the PDFs.	80
4.10	Normalized probability distribution functions of δu^L for (a) ODT at $Re_\lambda = 491$ and (b) DNS at $Re_\lambda = 460$ at fixed values of separation distance computed as $2^n \Delta x$, where n varies from 0 (\sim Kolmogorov scales) to 9 (\sim energy containing large scales) and Δx is the cell size (comparative results from Ishihara <i>et al.</i> [62]).	81

4.11	Normalized second-order longitudinal structure functions versus normalized separation distance. Solid lines depict ODT results and the dashed lines represent DNS results from Ishihara <i>et al.</i> [62].	82
4.12	Higher-order structure functions and their exponents. (a) The extension of the plateau region for the exponent ζ_4 with increase in Re_λ , and (b) increase in ζ_p as p increases from 1 to 6 (along the direction of the arrow) for $Re_\lambda = 929$. The horizontal lines in (b) correspond to the ζ_p values of 0.49 ($p = 1$), 0.83 ($p = 2$), 1.07 ($p = 3$), 1.26 ($p = 4$) and 1.4 ($p = 5$).	83
4.13	Intermittency in the structure-function exponents of ODT, compared with DNS results from Iyer <i>et al.</i> [69]. $\zeta_{(p,0)}$ denote the scaling exponents for longitudinal structure functions.	84
4.14	Velocity (a, b: top) and velocity derivative (a, b: bottom) in two extreme dissipation events for $Re_\lambda = 929$, at times t_e^1 (12.05 T_{11}) and t_e^2 (13.09 T_{11}), within the x -range (normalized with L_f) depicted by the vertical dashed lines. The profiles immediately before and after the extreme event are also shown at times t_- and t_+ , which are in immediate vicinity of the studied event. The inverse eddy time scale of the invoked eddies at these extreme events are shown in (c), where individual eddies are identified by an index.	86
4.15	(a) Positive correlation of extreme dissipation with eddies at large $1/\tau$ and clustering density. (b) Scaling of computational cost as a function of Re_λ	89
5.1	Representative vorticity distribution or intensity functions $\psi(z/l)$ of AEM.	96
5.2	Representation of the triplet-map in ODT.	100
5.3	Velocity profile obtained from ODT simulation of channel flows using the F-ODT algorithm at $Re = 22,000$, where $Re = U_\infty \delta_c / \nu$, U_∞ is the free-stream velocity and ν is the kinematic viscosity. DNS results from Graham <i>et al.</i> [49].	103
5.4	(a) Contours of $g(z_o, l)$ as defined in equation (5.17) for turbulent boundary layer flow and (b) $g(z_o, l)$ corresponding to three different eddy start locations, from the R-ODT formulation.	106

5.5	Vorticity distribution and transformed terms of equation (5.30) show similar behaviour to descriptions of third category of type-A eddy in AEM [131]. m refers to the ratio of δ_1 to the eddy size l considered.	109
5.6	Mean streamwise-velocity profiles $\langle u_1 \rangle$ obtained for four different arbitrary initial conditions normalized with the streamwise velocity at start of log-layer $U_o(z = 100\delta_\nu)$ from the R-ODT formulation at $C = 2$ exhibit linear regions close to the wall. A line fitted to the straight section of the produced profiles are shown in red.	111
5.7	Transverse normal stress profile for two R-ODT cases and an F-ODT case at $Re = 22,000$. Experiments (symbols) from Wei and Willmarth [179] and DNS (dashed-line) results from Graham <i>et al.</i> [49]. The region between the two vertical dashed lines refers to the transition region between the buffer layer and the log-law region.	113
5.8	Reynolds shear stress variation in the boundary layer for two R-ODT cases and an F-ODT case at $Re = 22,000$. AE refers to R-ODT with only wall-attached eddies, and AE & DE refers to R-ODT with both attached and detached eddies. Experimental data is from Wei and Willmarth [179]. . . .	115
5.9	Variation of $\Delta u_1(z)$ with wall-normal distance to explain the evolution of shear Reynolds stresses in the R-ODT formulation with logarithmic (a) and linear (b) z^+ , at $Re = 22,000$	116
6.1	Conceptual illustration of the ODT domain in a turbulent boundary layer (top) and the representation of the triplet-map applied to the variable $q(z)$	125
6.2	Comparison of ODT simulations with different C parameters at $T_w/T_r \approx 0.73$. The DNS results from Zhang <i>et al.</i> [192] are shown in solid black and the dashed line in (a) corresponds to the von Kármán's law of the wall.	131
6.3	Comparison of ODT simulations with different Z parameters at $T_w/T_r \approx 0.73$. The DNS results from Zhang <i>et al.</i> [192] are shown in solid black and the dashed line in (a) corresponds to the von Kármán's law of the wall.	132

6.4	Comparison of ODT simulation results at T_w/T_r values of 0.26 (blue), 0.45 (green) and 0.73 (red) in solid lines with $C = 15$ and $Z = 100$. The DNS results from Zhang <i>et al.</i> [192] are shown in dashed lines with T_w/T_r values of 0.25 (blue) and 0.75 (red). The black dashed line in (a) corresponds to the von Kármán’s law of the wall.	135
6.5	Variation of normalized TKE production rate with wall-normal distance for $T_w/T_r \approx 0.26$ (blue) and 0.73 (red).	137
6.6	Variation of Pr_t with wall-normal distance, where the dashed black line shows $Pr_t = 1$. The colored lines are the ODT results (solid) and DNS (dashed) results from Zhang <i>et al.</i> [192], for $T_w/T_r = 0.26$ (blue) and 0.73 (red).	139
6.7	Normalized probability distribution function of $T(z)$ for (a) $T_w/T_r \approx 0.73$ and (b) $T_w/T_r \approx 0.26$	140
6.8	Normalized probability distribution function of dT/dz for (a) $T_w/T_r \approx 0.73$ and (b) $T_w/T_r \approx 0.26$	141
6.9	Spectrum of pressure fluctuations near wall compared with Liepmann spectrum [93] using the analytical formulation of Grasso <i>et al.</i> [50].	143

List of Tables

4.1	List of cases of HIT in the present study. D^* is evaluated using the energy spectrum with the inertial range extrapolated below $k = 6$. The terms in the parentheses are normalizing factors used for the respective quantities.	69
6.1	List of cases of compressible TBL in the present study with a domain length $L = 0.05$, $L_{min} = 1.5 \times 10^{-5}$ and $T_w/T_r \approx 0.73$	130
6.2	List of cases of compressible TBL in the present study with a domain length $L = 0.05$	134

List of Abbreviations

AEM Attached-Eddy Model

DL Darrieus-Landau

DNS Direct Numerical Simulations

F-ODT Full-ODT

HIT Homogeneous Isotropic Turbulence

HLLC Harten-Lax-van Leer-Contact

LEM Linear-Eddy Model

LES Large-Eddy Simulation

NS Navier-Stokes

ODT One-Dimensional Turbulence

R-ODT Reduced-ODT

RANS Reynolds-Averaged Navier-Stokes

RM Richtmeyer-Meshkov

RSH Refined-Similarity Hypothesis

RSM Reynolds Stress Models

RT Rayleigh-Taylor

STI Shock-Turbulence Interaction

TBL Turbulent Boundary Layer

TKE Turbulent Kinetic Energy

WENO Weighted Essentially Non-Oscillatory

List of Symbols

A_c notional cross section area normal to the ODT domain

b_i Coefficient of absolute of kernel function J for i^{th} velocity component

c_i Coefficient of kernel function K for i^{th} velocity component

C_{KE} proportionality constant in production rate equation

C ODT turbulence intensity parameter

C_p proportionality constant in the equation for structure function of order p

c speed of sound

df degrees of freedom

d_i Coefficient of kernel function during forcing for i^{th} velocity component

\mathbb{D} departure term for probability density in AEM

dx_{min} minimum grid size

D normalized dissipation rate

E total energy

E_{kin} kinetic energy change associated with an eddy

$E(k)$ turbulent kinetic energy spectrum

E_{pe} potential energy term

E_{vp} viscous penalty term

e internal energy

\mathcal{F}_i function for velocity induced by eddy in AEM

f triplet-map function

g_1 probability density for eddy start location

g_2 probability density for eddy size

\hat{g}_i probability associated with an eddy Φ_i

g_o probability density for eddy with the eddy-start location fixed at the wall

g joint probability density of eddy of specific size and start location

H Heaviside step function

I_{ij} intensity functions in AEM

J absolute value of kernel function

K kernel function

\hat{k} turbulent kinetic energy

K_o Kolmogorov constant

k_t thermal conductivity

k wave-number

L_ϵ integral length scale

l eddy size

L_f forcing length scale

l_{KE} length scale of kernel event

L_{min} minimum eddy size

L system length scale

M Mach number

\mathcal{M} molecular mass

M_t turbulent Mach number

N number of grid points

p_e eddy acceptance probability in ODT

P_H AEM eddy acceptance probability density

\mathcal{P} turbulence production rate

Pr_t turbulent Prandtl number

P pressure

P' pressure fluctuation

p order of structure function

Q_i available energy in i^{th} velocity component

q_i heat flux along the i^{th} direction

\hat{q}_j probability associated with a state X_j

\mathbb{Q} characteristic velocity scaling in AEM

Re_λ Taylor microscale Reynolds number

Re_τ friction Reynolds number

R_{KK} sum of variances of three velocity components

\mathbf{r} displacement vector

S velocity-derivative skewness

T_{11} integral time scale

T' temperature fluctuation

T temperature

$\hat{T}(k)$ energy transfer function

t_{KE} time scale of kernel event

T_r recovery temperature

T_w wall temperature

t time

$\bar{\bar{u}}_i$ post kernel transformation i^{th} velocity component

\bar{u}_i post triplet-map i^{th} velocity component

$u_{i,k}$ change induced in the i^{th} velocity component using the kernel function

u'_i fluctuation of i^{th} velocity component

u_i i^{th} velocity component

U_o characteristic-velocity scale

\mathcal{U} velocity-scale

U_τ friction-velocity scale

\mathbf{u} velocity vector

V_i induced i^{th} velocity component by AEM eddies

\mathbf{x} position vector

x ODT domain axis (unless otherwise stated)

Z ODT viscous penalty parameter

η Kolmogorov length scale

α parameter to relate y-derivative to x-derivative in HIT study

β parameter to relate z-derivative to x-derivative in HIT study

δ_c boundary layer thickness considered in AEM

ΔE_i energy change induced by eddy

δ_{ij} Kronecker delta

δ_ν viscous wall unit

δ_1 smallest eddy size considered in AEM

Δt_{eddy} eddy-sampling time interval

Δt_e mean eddy-sampling time

Δt_{solve} time interval between two flow solutions

$\langle (\delta u_r^L)^p \rangle$ p^{th} order longitudinal structure function

ϵ turbulence dissipation rate

ζ_p scaling exponent for p^{th} order structure function

Γ vorticity distribution profile in AEM
 γ_s exponent of stretched-exponential function for dissipation rate
 γ specific-heat ratio
 κ_t thermal diffusivity
 Λ eddy rate
 $\hat{\Lambda}$ averaged eddy rate
 λ_r eddy distribution rate
 λ_s second viscosity coefficient
 λ Taylor length scale
 μ_i intermittency exponent
 μ dynamic viscosity
 ν kinematic viscosity
 Ω vorticity induced by eddies
 ω ODT parameter for energy redistribution
 Φ_i eddy event denoted by index i
 $\Pi(k)$ Energy flux spectra
 ψ contribution to mean-flow property in turbulent boundary layer by individual eddies
 Ψ mean-flow property in turbulent boundary layer
 $\bar{\rho}$ post triplet-map density
 ρ density

σ_{ij} component (i^{th} row and j^{th} column) of the stress tensor

τ_w wall shear-stress

τ eddy time-scale

Θ difference between local temperature and wall temperature

θ scalar variable

ξ logarithmic transformation variable used in AEM

$\langle(\cdot)\rangle$ mean of a variable (\cdot)

$(\cdot)^+$ variable (\cdot) scaled as per wall-scaling normalization factors

$(\cdot)'_{rms}$ root-mean square fluctuation of a variable (\cdot)

$(\cdot)_{TL}$ variable (\cdot) transformed as per the scaling by Trettel and Larsson

$(\cdot)_{VD}$ variable (\cdot) transformed as per van Driest scaling

Chapter 1

Introduction

Turbulence refers to the seemingly random fluctuating motions in a fluid flow [8] and the instantaneous velocity, pressure, and density fields are governed by the Navier-Stokes (NS) equations. Turbulence can be observed commonly in flowing water, chimney smoke, and strong wind movements, as well as in advanced scientific disciplines ranging from aerospace vehicles to astrophysical phenomena [16], such as supernova explosions and interstellar clouds. Due to the overwhelming existence of turbulence in nature and the absence of a generalized solution of the NS equations [61], great emphasis has been placed on understanding and predicting turbulence.

The Reynolds number [142, 143] is the most representative non-dimensional number used to describe turbulence and represents the ratio of inertial to viscous forces in the flow. A flow is turbulent at high Reynolds number when the inertial forces dominate over dissipative, viscous forces. The Reynolds number can also be used to represent the ratio between the largest and smallest length scales in a turbulent flow field. Practical flows occur at high Reynolds numbers and this thesis focuses on modelling the turbulence in these high Reynolds number flows.

1.1 High-Reynolds number turbulence modelling

Turbulence simulations at high Reynolds number are indispensable for predictive modelling of flows in aerospace, automotive components, atmospheric turbulence, and astrophysics. Flows in these applications exhibit a large spatiotemporal scale separation and require reliable fluid flow computations or detailed experiments to be able to characterise the role of turbulence [102]. High-Reynolds number turbulence is also important to be studied in its own right, as Dr. Richard Feynmann correctly pointed out that “*turbulence is the most important unsolved problem of classical physics.*” Over 60 years later, this quote remains as true as ever. Thus, the understanding of high-Reynolds number turbulence is of interest given its foundational importance to physics.

Since the analytical solution to the Navier-Stokes equations remains mathematically intractable [136], the numerical solution of the discretized equations can be used to study turbulence. The computational solutions of the NS equations must contend with the specific challenges brought on by multi-scale nature of turbulence:

1. Direct Numerical Simulations (DNS) solve the NS equations by resolving all the length and time scales [126, 146] of the turbulence; for this reason, computational costs limit the DNS studies to the Reynolds numbers [18, 7] corresponding to a moderate scale separation. The non-locality and non-linearity of the convective terms in the NS equations demands a very fine spatiotemporal resolution, thus leading to extreme computational cost to adequately resolve the turbulence. Recent DNS simulations, enabled by a continuous rise in computational capabilities, approach high Reynolds numbers (up to Taylor-scale Reynolds number of about 2500) [186], however, the method is still limited to canonical geometries. A significant increase in Reynolds number from the current DNS capabilities requires the use of modelling approximations [102], as is done in other approaches outlined below.
2. Large-Eddy Simulation (LES) reduces the computational requirement for practical systems by introducing models for the smaller scale turbulence [159, 97, 26] at the subgrid scales, and solves for filtered variables which account only for the motions

with scales larger than a specific cut-off. Hence, the large-scale turbulence is directly simulated, while small scales are represented by subgrid-scale models; thus reducing the scale separation of the problem and, concomitantly, the computational cost of the problem. In wall-bounded turbulent flows, the computational cost of the highly anisotropic near-wall turbulence may be further reduced through the use of wall modelling [90].

3. Reynolds-Averaged Navier-Stokes (RANS) remains the tool of choice for industrial computations with shorter turnaround time as compared to LES. In RANS, the *effect* of turbulence on the mean flow is modelled instead of resolving the scales of turbulence. The commonly used RANS models rely on the Boussinesq assumption that allows us to represent the Reynolds stresses of the turbulence as an effective eddy viscosity. The two-equation models use a combination of turbulence quantities—either Turbulent Kinetic Energy (TKE) (\hat{k}) and dissipation rate (ϵ) [72, 91], or the TKE (\hat{k}) and the variable $\omega = \epsilon/\hat{k}$ [180]—to characterize the state of turbulence in the computational domain. A one-equation model, extensively used in aerodynamic applications, was developed in Ref. [161]. Although RANS is computationally affordable, these models introduce simplifications and assumptions that lead to inaccuracies, especially for complex flows. For example, the RANS models are not particularly effective at handling curved boundaries [189, 177] due to their inadequate representation of different components of the Reynolds stress tensor. Advanced Reynolds Stress Models (RSM) use complex sub-models to solve the transport of individual components of the Reynolds stress tensor; although not as robust as one- or two-equation models, RSM can improve RANS predictions in complex flows [37].

Out of the methods listed above, DNS alone represents NS turbulence without introducing modelling assumptions, and thus is used as a benchmark for assessing the performance of the turbulence models used in this work.

1.2 Computational cost of state-of-the-art DNS

DNS directly solves the discretized, time-dependent NS equations and must resolve all relevant time and length scales of the turbulent flow; this leads to simulations requiring an exorbitant computational cost even at modest Reynolds numbers. Given the computational costs, DNS is often used to simulate the most idealized cases of turbulent flows, such as Homogeneous Isotropic Turbulence (HIT).

In HIT, we define the Reynolds number based on the Taylor length scale λ as $Re_\lambda = u'\lambda/\nu$, where ν is the kinematic viscosity and u' is the root-mean-square velocity fluctuation. The total number of grid points to resolve all the scales from the largest scale L to the smallest length scale η (which is shown to be the Kolmogorov length scale in Chapter 2) scales with $N^3 \approx Re_\lambda^{9/2}$ for a three-dimensional DNS simulation, where N is the number of grid points along one dimension. The computational cost scales as $N^4 \approx Re_\lambda^6$ as the maximum time step of the simulation scales with the grid size. The largest DNS simulation to date was conducted by Yeung *et al.* [185] and requires $32,768^3 \approx 32$ trillion grid points to achieve $Re_\lambda \approx 2500$. The increase in Re_λ by a factor of 2 requires the cost to increase by 2^6 , thus demanding a steep rise in computational capabilities. It is evident that a massive rise in computational cost increases the Re_λ only moderately. Figure 1.1 shows the progress of the DNS simulations of HIT over the decades in terms of Re_λ achieved. Despite the drastic improvements in computational power that have led to a significant rise in simulated Re_λ in the last two decades, the trend will not continue indefinitely as the silicon chips encounter physical limits when their sizes approach atomic scales [172]. Thus, to enhance the modelling capability for extreme-Reynolds number turbulence, there is a need to explore alternative approaches that can extend the reach of existing computational capabilities to higher Reynolds numbers.

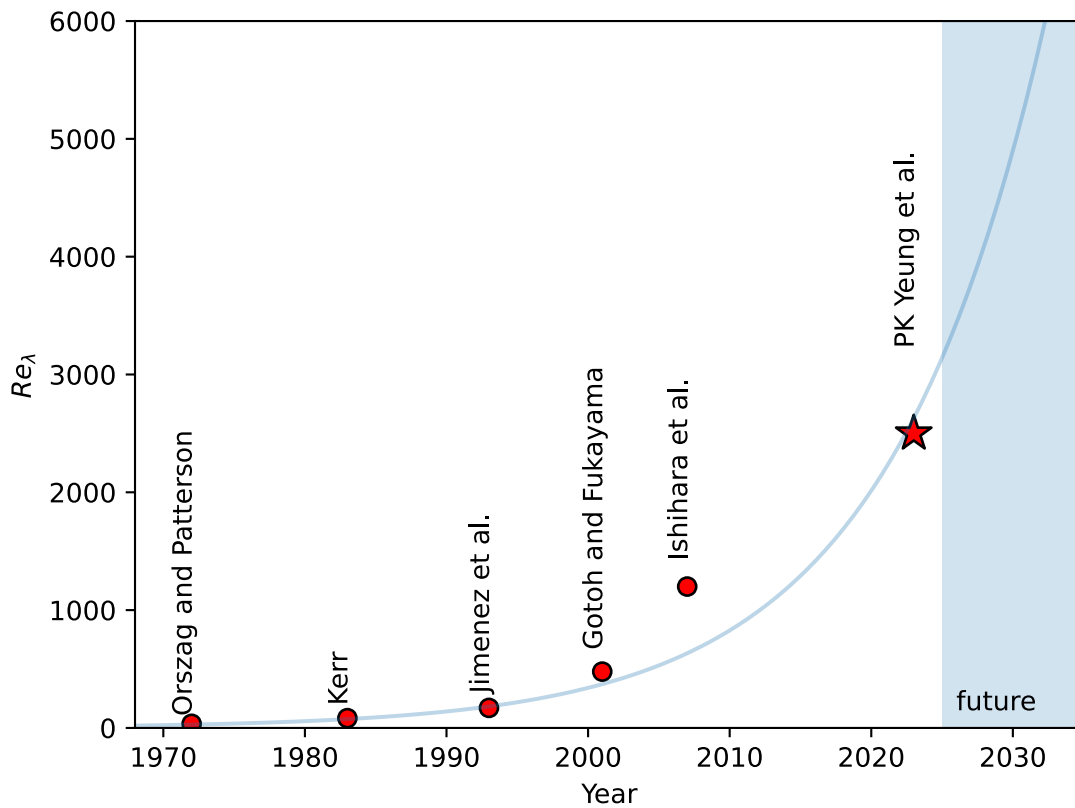


Figure 1.1: Progress in the DNS simulations in terms of Re_λ achieved over the years. The line represents a curve-fit approximation of the maximum Re_λ DNS simulation through the decades.

1.3 Dimensionality reduction to model turbulence

A model is a simplified representation of a complex reality, and is aimed at understanding the key features of the phenomenon being observed. The introduced simplifications are justified if the essential elements of the phenomenon being studied are retained, while neglecting the secondary and less relevant aspects. Preserving the central feature of turbulence, that is its multi-scale nature resulting from the non-linearity of the governing equations, modelling assumptions can be made to enable study of high Reynolds number turbulence.

Although turbulence is inherently three-dimensional, its representation along one spatial dimension reduces the degrees of freedom of the problem, which helps to counter the steep increase in computational cost with increasing Re_λ . A one-dimensional analogue of turbulence should produce the proven turbulence characteristics and accurately represent all the spatio-temporal scales of the problem, albeit along one direction in space. The dimensionality reduction provides important insights into the high-Reynolds number turbulence, while incorporating the multi-scale nature of turbulence, despite relying on some key modelling assumptions to account for the effects of three-dimensional eddies on a one-dimensional domain. Most canonical flows in turbulence studies, such as HIT, turbulent boundary layers, channel, and jet flows, demonstrate self-similar nature along one characteristic dimension. Hence, lending credibility to the approach of dimensionality reduction to advance the understanding of such flows.

1.3.1 One-dimensional turbulence

The One-Dimensional Turbulence (ODT) method, originally formulated by Kerstein [78], uses a combination of statistical and structural approaches to model turbulence along a single dimension. ODT resolves all the scales of the turbulence using one-dimensional stochastic eddies that distort the underlying fluid flow. This method is built on a structural view of the turbulence interactions by stochastically modelling the distribution of turbulent eddies while deterministically defining their effects on the single dimension of the flow. The

three-dimensional turbulent eddies are represented using the ODT eddies, which constitute pre-defined measure-preserving mappings.

The ODT method has its roots in Linear-Eddy Model (LEM) which was also developed by Kerstein [77] to model the mixing by turbulent stirring. Instantaneous rearrangement events are superimposed over the deterministic fluid flow to emulate the effects of individual eddies over the concentration field in LEM (see figure 1.2). The distortion of the concentration field is generalized to apply to all the flow properties in ODT. Rearrangement events are performed on a single dimension as a Markovian process [79], where sequential eddies affect the flow properties. Flow profiles are compressed and rearranged to represent a turbulent eddy by using a mapping shown in figure 1.3. The mathematical formulation of the triplet map is described in Chapter 3.

The initial LEM formulation by Kerstein [77] was expanded to incorporate the two-way coupling of the flow variables and the scalar concentration profiles [78]. This involves accounting for the influence of post-eddy flow properties in the implementation of subsequent eddies. The ODT framework was further extended to include variable density flows and incorporate cylindrical and spherical symmetry, which is encountered in some canonical flows [6, 95]. A recent milestone in the development of ODT is the release of an open-source code by Stephens and Lignell [169], which represents the culmination of a decade-long effort in advancing ODT.

1.3.2 Modelling complex flows and compressibility effects in ODT

The application of the one-dimensional ODT approach in studying dynamic phenomena such as the Rayleigh-Taylor (RT) instabilities [46], the Darrieus-Landau (DL) instability [74] and the Richtmeyer-Meshkov (RM) [73, 45] instability demonstrates its potential in handling complex flow physics. Rayleigh-Taylor instability modelling involves considering the impact of gravity acceleration on density-stratified fluids. Darrieus-Landau instability involves the acceleration of varying-density fluid caused by thermal expansion at the flame front, while turbulence is generated by the passage of a shockwave over a contact discontinuity in the Richtmeyer-Meshkov instability. Although these phenomena inherently

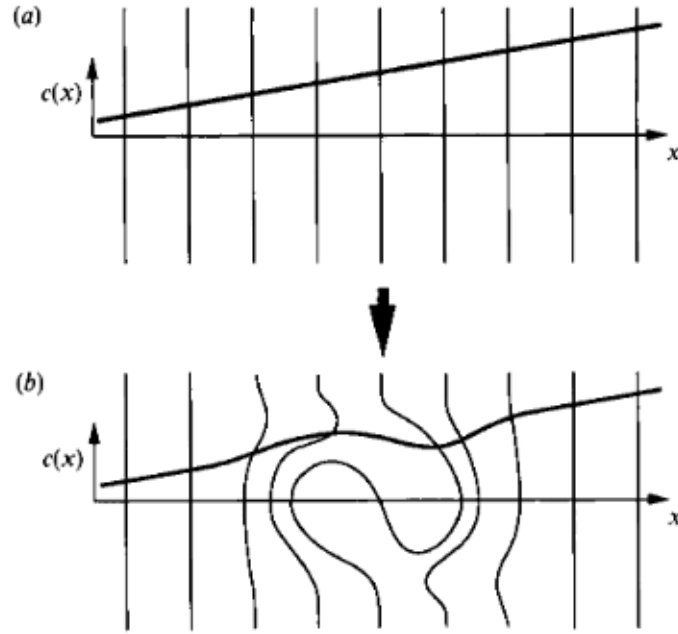


Figure 1.2: Schematic of a single clockwise eddy on scalar field that initially has uniform concentration gradient. (a) Initial concentration isopleths (vertical lines) and concentration profile $c(x)$ (heavy line) parallel to the initial concentration gradient. (b) Concentration isopleths and concentration profile after eddy is imposed [77].

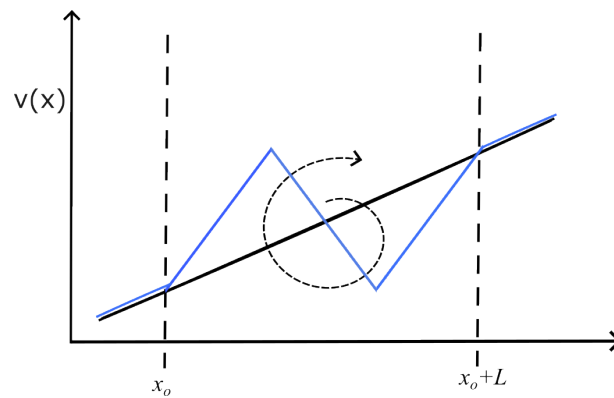


Figure 1.3: Mapping of variable $v(x)$ to represent effect of a turbulent eddy.

possess three-dimensional characteristics, ODT has shown promise in providing reduced-dimensional, lower-order models. Multiple studies on homogeneous turbulence and turbulent boundary layers have shown a significant ability of ODT framework to construct low-cost models [78, 44, 85].

Modelling turbulence becomes more challenging when compressible effects are prominent. As the Mach number of a flow increases, compressibility effects lead to a strong coupling between continuity, momentum, and energy equations. This coupling has a substantial impact on both the mean and fluctuating quantities. In compressible flows, the relative dominance of heat and momentum transfer plays an important role and scalings are often used to map the compressible flow profiles to the well-known incompressible turbulence behaviour. High-speed flows exhibit significant fluctuations in both the thermodynamic variables (pressure, density, and temperature) and the hydrodynamic variables (velocity). Therefore, a carefully designed approach for modelling compressible turbulence is essential. We extend the incompressible ODT model to a fully compressible formulation that allows simulation of high-speed flows.

1.4 Scientific contributions of the thesis

- **Development of a Eulerian framework for compressible ODT** (chapter 3). The original formulation of ODT is Lagrangian and does not adapt well for use in compressible flows. Hence, we couple the energy equation alongside the continuity and momentum equations. The ODT turbulence model is modified to operate over conservative properties for enabling coupling of momentum and heat transport in a unified framework.
- **Characterized the turbulence of HIT at extreme Reynolds number** (chapter 4). We show the validity of ODT in exploring intermittency and high-Re turbulence. The developed model is used to generate turbulence by large-scale forcing at different Reynolds number by adjusting the smallest length scale represented. The collected

statistics are used to evaluate turbulent kinetic energy spectrum, dissipation rate characteristics, high-order structure functions and their scaling exponents.

- **Developed a mathematical framework to show the equivalency of ODT and Attached-Eddy Model (AEM) for high-Reynolds number turbulent boundary layer flows** (chapter 5). We study the ODT methodology and reduce it to its essential elements to establish equivalence with the AEM. The nature of eddy occurrence probabilities and vorticity distribution of the simplified ODT are compared with quantities in AEM. The variation of resultant Reynolds stresses in the Turbulent Boundary Layer (TBL) profile are analysed with DNS results for benchmarking.
- **Built a systematic framework to study hypersonic boundary layer turbulence at extreme Reynolds numbers** (chapter 6). The compressible ODT model is further applied to model zero pressure-gradient turbulent boundary layers at $M \approx 5.86$ at different conditions of cooled walls, which are relevant for practical applications. The mean-statistics of velocity and temperature obtained are compared with DNS results, while providing insights into statistics of temperature fluctuations.

1.5 Outline of the thesis

This thesis is manuscript-based and comprises of several chapters, sequentially moving from background theory and methodology, to application of the developed modelling framework to the different canonical turbulent flows. Chapter 2 describes the background theory of aspects of turbulence that are studied, namely, the energy cascade in HIT, extreme dissipation events, intermittency, the structural aspects of turbulence, turbulent boundary layer profiles and wall-scalings. Chapter 3 describes the theoretical framework of the ODT method and the specific contributions towards the development of a fully compressible ODT scheme.

Chapters 4, 5, and 6 are a series of individual articles that are at different stages of

publication in peer-reviewed journals at the time of submission of this thesis. The contents of chapter 4 have already been published, whereas the articles corresponding to chapters 5 and 6 are under revision. Chapters 4, 5 and 6 are self-contained, first introducing the specific problem in context of existing literature, explaining the specific methodology, which is followed by the results and discussions. Even though these chapters address different problems, each chapter follows from the previous chapter logically. Chapter 4 studies the idealized form of turbulence–HIT. The turbulence on interaction with a wall is studied next in context of the AEM in chapter 5. The insights gained from chapter 5 lead to the adoption of the current model to compressible TBL in chapter 6. Some sections of the methodology repeat in Chapters 4, 5 and 6, to present the modifications specific to the context of each problem, while making each chapter stand-alone.

Finally, chapter 7 presents the findings in an integrated manner and proposes recommendations for future work.

Chapter 2

Turbulence in canonical flows

This chapter briefly describes the background theory of different aspects of turbulence, which are addressed in the studies conducted in subsequent chapters of the thesis.

Turbulence can be understood using statistical, structural, and deterministic viewpoints [19]. The statistical perspective sees turbulence as a stochastic process and relies on statistical tools to characterize it. The flow is quantified in terms of probability distributions, averages, correlations, and spectra. In contrast, the structural viewpoint considers turbulence as a composition of individual turbulent eddies. This approach aims to identify and study coherent structures within the flow, focusing on their organization, interactions, and effects on the overall turbulence dynamics. The deterministic approach focuses on the stability and transition of flows. It involves analysing the flow equations and performing stability analyses to understand the conditions that lead to flow instabilities and the subsequent transition to turbulence. This work primarily deals with the first two elements: the statistical and structural views of turbulence.

2.1 A summary of turbulence characteristics

2.1.1 Multi-scale nature of turbulence

Turbulent flows are characterized by the presence of multiple length- and time-scales ranging from small-scale, dissipative eddies to large-scale turbulent motion. The small-scale turbulence is isotropic and the often anisotropic, large-scale motions are influenced by the boundary conditions of the flow [136]. The separation of the scales is a function of the Reynolds number, where high Reynolds number flows exhibit turbulent energy distributed over wider range of scales.

The concept of *energy cascade*, originally introduced by Richardson [144], states that the energy added at the largest scales of the system is transferred to progressively smaller scales by inviscid processes and is finally dissipated due to viscous forces at the smallest scales, see figure 2.1. Turbulence is understood to consist of coherent regions of length scale l , known as *eddies*, with the associated velocity and time scales defined as $\mathcal{U}(l)$ and $\tau(l) = l/\mathcal{U}(l)$. The largest eddies, at the system length-scale L , are unstable and breakdown into smaller eddies. These smaller eddies in turn break into further smaller eddies, until the smallest eddies, which are stable, are dissipated by viscous mechanisms [136]. Since the amount of energy transferred among the different scales remains constant when the turbulence is in equilibrium, the rate of dissipation, ϵ , at the smallest scales can be estimated to scale with the rate of transfer from the largest scale, given by $\mathcal{U}(L)^3/L$. In equilibrium, the aforementioned energy transfer rate equals the energy transfer across the intermediate scales. Kolmogorov's seminal work [87] provided the foundation for quantifying the smallest length scales and defined the characteristic scales of the eddies in turbulent flows. With the underlying hypothesis that the velocity scale $\mathcal{U}(l)$ and time scale $\tau(l)$ of an eddy decrease with the eddy size l , Kolmogorov postulated the following three hypotheses for high-Reynolds number turbulence [87].

1. **Local isotropy:** The turbulent motions at the smallest scales are statistically isotropic. The anisotropy at the largest scales linked to the boundary conditions and mean flow variations is lost as energy is transferred to smaller scales.

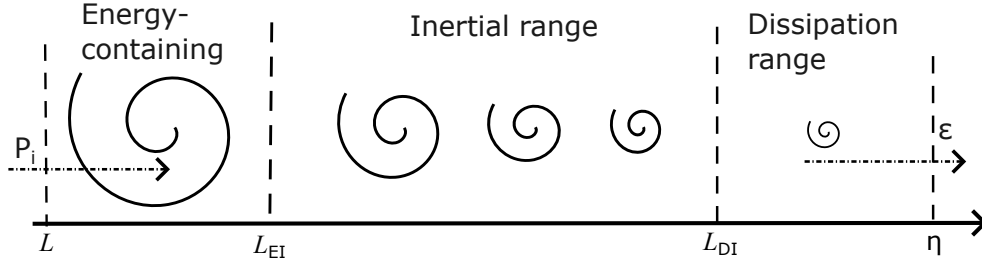


Figure 2.1: Energy cascade from the largest scales L to the smallest scales η , where L_{EI} and L_{DI} demarcate the inertial region from energy-containing and dissipation regions, respectively. P_i refers to the input energy at the largest scales.

2. **First similarity hypothesis:** The energy transfer rate at intermediate scales is equal to the dissipation rate ϵ , and the statistics of the smallest scales signified by the Kolmogorov length scale η have a universal nature determined solely by ϵ and kinematic viscosity ν .

$$\begin{aligned}
 \eta &\equiv (\nu^3/\epsilon)^{1/4} \\
 \mathcal{U}_\eta &\equiv (\nu\epsilon)^{1/4} \\
 \tau_\eta &\equiv (\nu/\epsilon)^{1/2}
 \end{aligned}
 \tag{2.1}$$

As a by-product of these definitions, the Reynolds number based on η is given by $Re_\eta = \mathcal{U}_\eta\eta/\nu$, which is unity.

3. **Second similarity hypothesis:** For scales of motion l such that $\eta \ll l \ll L$, the statistics of motion depend only on ϵ and are independent of ν .

$$\begin{aligned}
 \mathcal{U}(l) &\equiv (l\epsilon)^{1/3} \\
 \tau(l) &\equiv (l^2/\epsilon)^{1/3}
 \end{aligned}
 \tag{2.2}$$

The intermediate range between the largest scales and the Kolmogorov scales is known as the inertial range, and by this hypothesis, the velocity and time scales of eddies in the inertial range are directly proportional to the eddy size l .

2.1.2 Characteristics of turbulence

The Reynolds decomposition of the velocity field provides a framework for analysing turbulent flows [143]. The application of the Reynolds decomposition to the NS equations can be used to derive the evolution equation of the TKE and other turbulent stresses, as will be shown.

The three-dimensional velocity field can be decomposed into the mean $\langle u_i \rangle$ and the fluctuating components u'_i , the Reynolds decomposition is given as:

$$u'_i(\mathbf{x}, t) = u_i(\mathbf{x}, t) - \langle u_i(\mathbf{x}, t) \rangle, \quad (2.3)$$

where, $i = 1, 2$ and 3 refer to the velocity components along the x, y and z directions, respectively. The Reynolds decomposition applied to the continuity equation for incompressible flows $\nabla \cdot \mathbf{u} = 0$ reveals that the divergence of both the mean velocity field $\nabla \cdot \langle \mathbf{u} \rangle$ and fluctuating velocity field $\nabla \cdot \mathbf{u}'$ is zero for incompressible flows.

Applying the Reynolds decomposition to the momentum equation, one arrives at the RANS equations.

$$\rho \frac{\partial \langle u_i \rangle}{\partial t} + \rho \frac{\partial \langle u_i \rangle \langle u_j \rangle}{\partial x_j} = -\frac{\partial \langle P \rangle}{\partial x_i} + \frac{\partial}{\partial x_j} \left(\mu \frac{\partial \langle u_i \rangle}{\partial x_j} - \rho \langle u'_i u'_j \rangle \right) \quad (2.4)$$

Here, ρ and P are the density and pressure, respectively, while μ refers to the dynamic viscosity of the fluid. Equation 2.4 resembles the classical NS equations, with the addition of the term $\rho \langle u'_i u'_j \rangle$, which represents the turbulent Reynolds stresses. The Reynolds stress tensor, $\rho \langle u'_i u'_j \rangle$, has indices i and j ; the diagonal terms ($i = j$) are the turbulent normal stresses and the off-diagonal terms ($i \neq j$) are the turbulent shear stresses. Equation (2.4) on rearrangement and substitution of Reynolds decomposition of velocity gives the well-known TKE equation (\hat{k} denotes the TKE):

$$\begin{aligned} \frac{\partial \hat{k}}{\partial t} + \frac{\partial \langle u_j \rangle \hat{k}}{\partial x_j} = & \underbrace{-\langle u'_i u'_j \rangle \frac{\partial \langle u_i \rangle}{\partial x_j}}_{\text{Production}} - \underbrace{\frac{\partial}{\partial x_j} \left(\frac{1}{\rho} \langle u_j P' \rangle \right)}_{\text{Pressure diffusion}} + \underbrace{\frac{\partial}{\partial x_j} \left(\frac{1}{2} \langle u'_j u'_i u'_i \rangle \right)}_{\text{Turbulent transport}} \\ & - \underbrace{\left(\mu \frac{\partial^2 \hat{k}}{\partial x_j^2} \right)}_{\text{Viscous diffusion}} - \underbrace{\mu \left\langle \frac{\partial u'_i}{\partial x_j} \frac{\partial u'_i}{\partial x_j} \right\rangle}_{\text{Dissipation}} \end{aligned} \quad (2.5)$$

The terms that constitute the TKE equation, namely, the production, transport, viscous diffusion, and dissipation, remain at the core of the analysis of different turbulent flows in this work.

2.2 Structural aspects of turbulence

The existence of hierarchical structures in turbulence characterizes its multi-scale nature [155]. The turbulent flow can be understood as a multi-scale superposition of energy-containing coherent structures, which are the building blocks of turbulence. These structures exist over considerable length and time scales, are recurrent and can be seen as regions of concentrated vorticity [39]. The structural perspective of turbulence views the flow as interacting coherent structures while ignoring the incoherent part as noise [71]. The coherent structures are shown to provide a pathway for flow control strategies [153].

The complex nature of these vortical structures, including hairpin agglomerations, horseshoe vortices, ring vortices, is depicted in figure 2.2 from the study by Fric and Roshko [42] on a jet impinging on a cross-flow. Brown and Roshko [13] showed large-scale structures in turbulent mixing layers that are primarily two dimensional, originating from the rollers that arise due to the instability of a laminar shear layer [54]. Hickey *et al.* [52] studied the universality of wake structures in the far-field and investigated the dependence of the far-wakes to the initial conditions and the transitional effects, see figure 2.3. Another canonical flow where significant progress has been made in the studies of coherent structures is turbulent boundary layers. Zhou *et al.* [194] studied individual hairpin vortex-structures in the mean-turbulent flow and investigated the mechanism of creation of new coherent hairpin vortices from the primary structure. Lozano-Durán and Jiménez [101] showed the existence of some larger self-similar eddies that attach to the wall across the logarithmic layer. Vortex clusters [28] and three-dimensional self-similar objects [99] have been shown to exist in the logarithmic region of the turbulent boundary layer.

Several approaches have been taken to understand the vortex dynamics that makes up the coherent structures. For identifying the vortex cores, Hunt *et al.* [60] used the

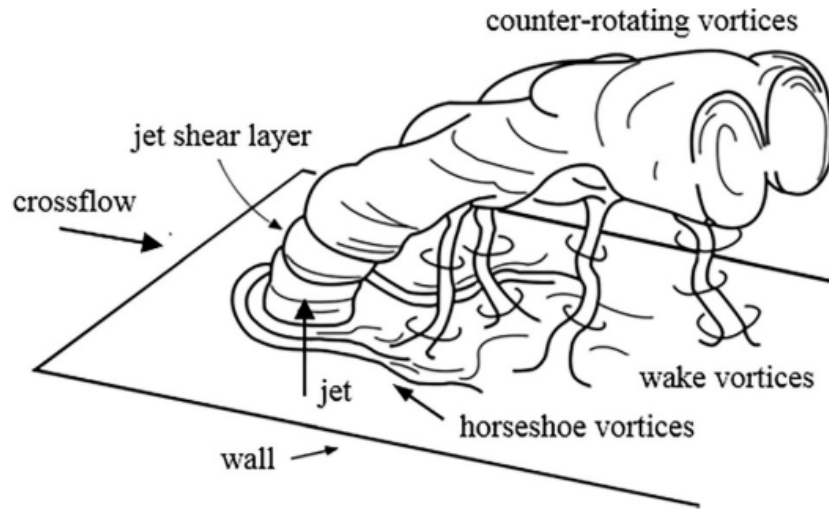


Figure 2.2: Structure of a transverse jet in cross-flow [42].

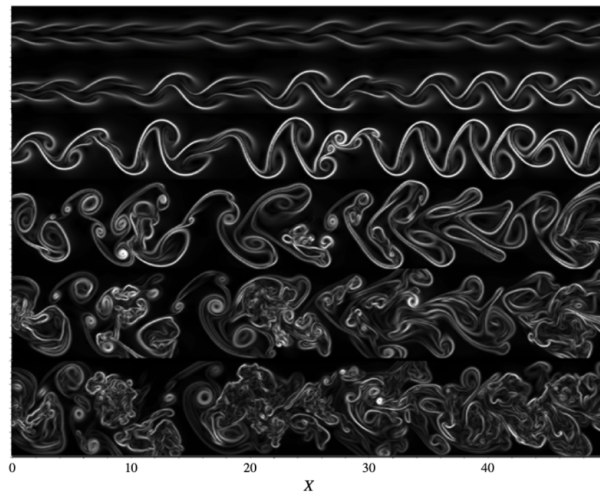


Figure 2.3: Evolution of coherent structures in planar wake [53].

second invariant of the velocity-gradient tensor. This criteria was later refined by Jeong and Hussain [70] who characterized vortex core by the (second) eigenvalue of the sum of the squares of the rate-of-strain and vorticity tensors, which represents the local pressure minima.

2.3 Idealized turbulence - HIT

Canonical flows such as HIT and turbulent boundary layers have undergone extensive research over the years and many of their reported turbulence characteristics are used for benchmarking the developed model in this work.

HIT is the most idealized and canonical turbulent flow characterized by turbulence that is both homogeneous and isotropic. As the turbulence characteristics must be the same in all directions, there can be no boundary constraining the turbulent flow in HIT. Although HIT is very difficult to experimentally recreate, the insights gained can play an important role in understanding the fundamental characteristics of turbulent flows. The universality of the small-scale turbulence statistics is one such fundamental characteristic and investigating it is a major challenge in modern turbulence studies [66]. Such an analysis of small-scale statistics requires a sufficiently high Reynolds number so that small scales are not contaminated by the influence of boundary conditions or large-scale forcing often used to generate HIT.

Typical DNS simulations of HIT are performed in a triply periodic box with equal number of grid points along the three dimensions. Due to the periodicity, NS equations can be efficiently solved using spectral methods with time-marching schemes [66, 62, 67].

2.3.1 Energy spectra

The mean statistics of the generated turbulence are most commonly represented by the TKE spectra (see figure 2.4), a theoretical solution of which was originally given by Kol-

mogorov [87] as:

$$E(k) = K_o \langle \epsilon \rangle^{2/3} k^{-5/3}. \quad (2.6)$$

The Kolmogorov constant $K_o = 1.62$ for the three-dimensional turbulence [163] and k is the wave-number. Here, the dissipation rate for three-dimensional turbulence is expressed as:

$$\langle \epsilon \rangle = 15\nu \left\langle \left(\frac{\partial u_1}{\partial x_1} \right)^2 \right\rangle \quad (2.7)$$

The TKE spectrum $E(k)$ when normalized by $\langle \epsilon \rangle^{2/3} k^{-5/3}$, known as the compensated energy spectrum, is constant $\approx K_o$ as per the theoretical solution from equation (2.6). The constancy of the compensated TKE spectrum is clearly observed as a flat profile in the inertial region when the Reynolds number is sufficiently large, as seen in the DNS results of Ishihara *et al.* [67]. The energy transfer amongst the scales is quantified by the energy flux spectra $\Pi(k)$ in terms of the energy transfer function $\hat{T}(k) = 2\nu k^2 E(k)$, using:

$$\Pi(k) = \int_k^\infty \hat{T}(k) dk. \quad (2.8)$$

The inertial range turbulence, when statistically steady, exhibits $\Pi(k) = \langle \epsilon \rangle$, thus the energy transport across intermediate scales equals the dissipation rate.

The energy spectrum has also been reported to show a universal scaling with the wave-number in the dissipation range. A functional form of the energy spectrum is identified in the high-wave-number range above a cut-off value that delimits the dissipation range [109, 65]. Schumacher [151] shows a slow exponential decay of the TKE spectra in the dissipation range, which is attributed to the increasing fluctuations at the sub-Kolmogorov scales. A combination of exponential functions was later introduced by Khurshid *et al.* [82], where one of the exponentials is associated with the intermittent interactions with the eddies at larger length scales. The dissipation spectrum scaling is shown in figure 2.4 alongside the scalings for the other regions of the TKE spectrum.

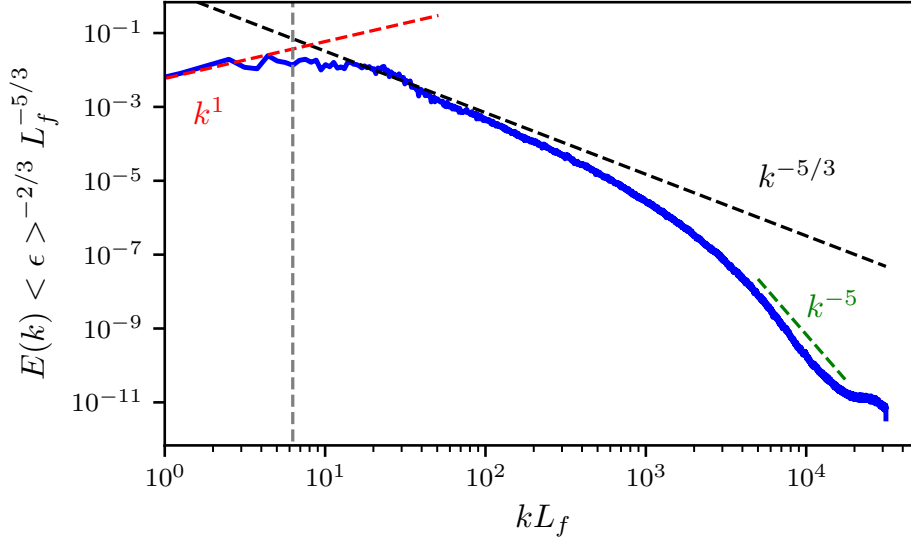


Figure 2.4: TKE spectra at $Re_\lambda = 82$ using the developed model.

2.3.2 Normalized dissipation rate

The dissipation rate $\langle \epsilon \rangle$ exhibits a dependence on the integral length scale L_ϵ and the velocity-fluctuation magnitude u' in a particular HIT realization. However, the normalized dissipation rate, D , defined as $D = \langle \epsilon \rangle L_\epsilon / u'^3$, exhibits a universal behaviour. As the Reynolds number increases to infinity, the normalized dissipation rate is observed to approach a finite limit at $D \approx 0.5$ [162, 164], even though the viscosity approaches zero. This limiting behaviour highlights the difference of a fluid flow with very small viscosity when compared to a completely inviscid flow. The parameter D typically shows values > 0.5 , and approaches 0.5 when the Taylor scale Reynolds number, Re_λ , is greater than about 400 [62]. Thus, a large scale separation is necessary to observe the limiting behaviour of D .

The normalized dissipation rate was found to be higher for decaying turbulence compared to forced turbulence by Bos *et al.* [11]. The value of D was also found to be different for different flows and initial conditions by Burattini *et al.* [15], except for HIT, where the

simulation setup plays a negligible role and the evaluation of the turbulence quantities is independent of the effects of flow boundaries.

2.3.3 Structure functions

Turbulent structure functions provide a valuable characterization of the energy cascade in physical space. They are computed using the difference in velocity at two points, \mathbf{x} and $\mathbf{x} + \mathbf{r}$, in space, given as:

$$\langle \delta u_{ij} \rangle = \langle [u_i(\mathbf{x} + \mathbf{r}, t) - u_i(\mathbf{x}, t)][u_j(\mathbf{x} + \mathbf{r}, t) - u_j(\mathbf{x}, t)] \rangle \quad (2.9)$$

The longitudinal structure functions are computed with the velocity components along the direction \mathbf{r} , and the transverse structure functions use the velocity components normal to the \mathbf{r} direction. The p^{th} -order structure function is given as:

$$\langle \delta u_{ii}^p \rangle = \langle (u_i(\mathbf{x} + \mathbf{r}, t) - u_i(\mathbf{x}, t))^p \rangle \quad (2.10)$$

The p^{th} -order structure function, $\langle \delta u_{ii}^p \rangle$, scales with the separation distance r as $\langle \delta u_{ii}^p \rangle \propto r^{\zeta_p}$, where ζ_p is the scaling exponent. The derived scaling exponents from experiments [4, 157, 173, 195] and simulations [76, 47, 48, 68, 69] have been widely reported to establish the universality of turbulence in terms of high-order structure functions. The scaling exponents can be used to determine the intermittency characteristics of turbulence, which we describe in the next section.

2.3.4 Intermittency

Unlike many other stochastic processes, turbulence is characterized by its non-Gaussian behaviour. Extreme gradients are intermittently observed in high-Reynolds number turbulence, see figure 2.5. Although these extreme events are rare, their dynamic importance cannot be overlooked in high-Reynolds number turbulence. Such intermittency effects are typically quantified by studying the higher-order structure functions.

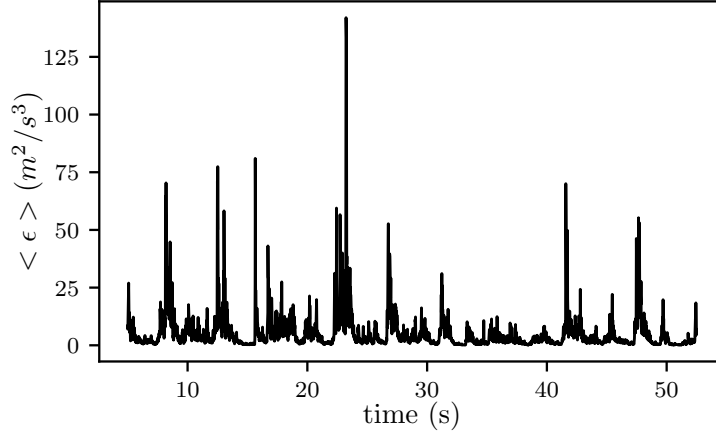


Figure 2.5: Intermittency observed in dissipation-rate variation averaged over the entire domain with time for $Re_\lambda = 929$.

Kolmogorov in his seminal work [87] hypothesized that the characteristics of the inertial range of turbulence is determined only by the mean dissipation rate $\langle \epsilon \rangle$ and separation distance r , which, by dimensional analysis, gives an expression for structure functions:

$$\langle \delta u^p(r) \rangle = C_p (\langle \epsilon \rangle r)^{p/3} \quad (2.11)$$

The prediction from equation (2.11) holds true for the second-order structure function ($p = 2$), and $\langle \delta u^2(r) \rangle$ is observed to scale with $(\langle \epsilon \rangle r)^{2/3}$ [149]. However, the scaling exponents for higher-order structure functions deviate from $p/3$, often referred to as anomalous scaling. Dubrulle [36] studies the mechanism of anomalous scaling in scale invariant systems. The discrepancy was later addressed in the Refined-Similarity Hypothesis (RSH) by Kolmogorov [88] and Oboukhov [125], and signifies the intermittency effects. Defining the instantaneous dissipation rate as ϵ_o and average dissipation rate of a sphere of radius r as ϵ_r , Kolmogorov [88] provided the scalings:

$$\begin{aligned} \langle \epsilon_o^2 \rangle / \langle \epsilon \rangle^2 &\sim (L/\eta)^{\mu_i}, \\ \langle \epsilon_r^2 \rangle / \langle \epsilon \rangle^2 &\sim (L/r)^{\mu_i}, \quad \text{if } \eta < r \ll L. \end{aligned} \quad (2.12)$$

Here, L is the energy-containing length scale and μ_i is the intermittency exponent and is positive. The value of μ_i has been experimentally determined to be 0.25 ± 0.05 [166]. RSH states that the statistics of $\delta u(r)$ depend on the local dissipation rate ϵ_r rather than the mean dissipation rate $\langle \epsilon \rangle$. The small-scale ($r \ll L$) statistics of the velocity difference $\delta u(r)$ conditioned on ϵ_r depend on ϵ_r and ν universally. The dependence is restricted to ϵ_r alone at intermediate scales $\eta \ll r \ll L$.

$$\langle \delta u^p(r) | \epsilon_r \rangle = C_p (\epsilon_r r)^{p/3} \quad (2.13)$$

The unconditioned mean structure function can be expressed as:

$$\langle \delta u^p(r) \rangle = \langle \langle \delta u^p(r) | \epsilon_r \rangle \rangle = C_p \langle \epsilon_r^{p/3} \rangle r^{p/3} \quad (2.14)$$

Substituting $\langle \epsilon_r \rangle$ from equation (2.12) gives a prediction of $\langle \delta u^6(r) \rangle$ as:

$$\langle \delta u^6(r) \rangle = C_6 \langle \epsilon \rangle^2 \left(\frac{L}{r} \right)^{\mu_i} r^2 = C_6 \langle \epsilon \rangle^2 L^{\mu_i} r^{2-\mu_i} \quad (2.15)$$

With $\mu_i = 0.25$, the exponent of r for $p = 6$ becomes $\zeta_6 = 1.75$. When $p = 3$, using $\langle \epsilon_r \rangle = \langle \epsilon \rangle$, we get the equation for the third-order structure function $\langle \delta u^3(r) \rangle$ to be identical with equation (2.11), thus showing no intermittency effects with $\mu_i = 0$ and $C_3 = -4/5$ (same as Kolmogorov 4/5 law [86]). With the conjecture that ϵ_r is log-normally distributed [88, 125] and from equation (2.12), the moments $\langle \epsilon_r^m \rangle / \langle \epsilon \rangle^m$ can be evaluated. This provides a generic expression of the scaling exponent for the p^{th} -order structure function as:

$$\zeta_p = \frac{p}{3} \left(1 - \frac{\mu_i(p-3)}{6} \right) \quad (2.16)$$

In equation (2.16), the second term in the brackets can be seen as the intermittency effect. Mandelbrot [105] argued that the log-normality of the local dissipation rate $\langle \epsilon_r^m \rangle$ was inconsistent and this causes deviations in the scaling exponents measured for high values of p . Ishihara *et al.* [64] highlighted that the non-zero value of the second term does not ensure the existence of intermittency, and can be attributed to the finite Reynolds number effects. Ishihara *et al.* [64] also reported a dependence of C_2 on the Reynolds number.

2.3.5 Extreme events and stretched-exponentials

Investigating small-scale turbulence is challenging and DNS is the classical tool of choice for characterizing extreme events. Small-scale turbulence at high-Reynolds number exhibits short-lived intense vorticity regions [188]. Sreenivasan and Meneveau [167] infer that the multi-fractal nature of the dissipation rate renders the mean-dissipation rate insufficient to capture the small-scale turbulence dynamics.

The non-Gaussian behaviour and the extended tails of the probability distribution functions of turbulence quantities are often used to quantify intermittency characteristics [62]. Figure 2.6 shows the extended tails of the PDF of velocity-derivative—similar to the ones observed in dissipation rate PDFs. The tail regions correspond to the regions of extremely high dissipation rate localized in space and time which are rare, with decreasing probabilities of occurrence for higher values of dissipation rate. The extended PDF tails make significant contributions to the higher-order structure functions [136], and are tied to the increased intermittency effects seen at high values of structure-function order p . The strong connection of the dissipation rate to intermittency has been shown by Sreenivisan and Antonia [165]. Nelkin [123] and Yeung *et al.* [187] among other works considered the comparison of scaling exponents for dissipation rate with enstrophy.

The resolution requirement has been deemed important in determining the structure of small-scale turbulence [183, 30]. The effect of the resolution on the PDF tails and the multifractal nature of the scalar dissipation rate was also investigated by Schumacher *et al.* [152]. Yeung *et al.* [187] highlighted the stringent requirements for the right estimation of the occurrence probability of extreme dissipation events. Sufficient resolution in space and time is recommended for further smaller fractions of the Kolmogorov length scale, along with reduced Courant numbers.

The PDFs of locally averaged dissipation rate show extended tails [21], which have been studied to establish universality of small-scale turbulence. Well-resolved simulations are often used to approximate the obtained PDFs of the dissipation rate using exponential functions termed as *stretched-exponentials* [43]. Luévano [103] utilized a maximum entropy principle to derive the stretched-exponentials. Yeung *et al.* [187] quantified the impact of

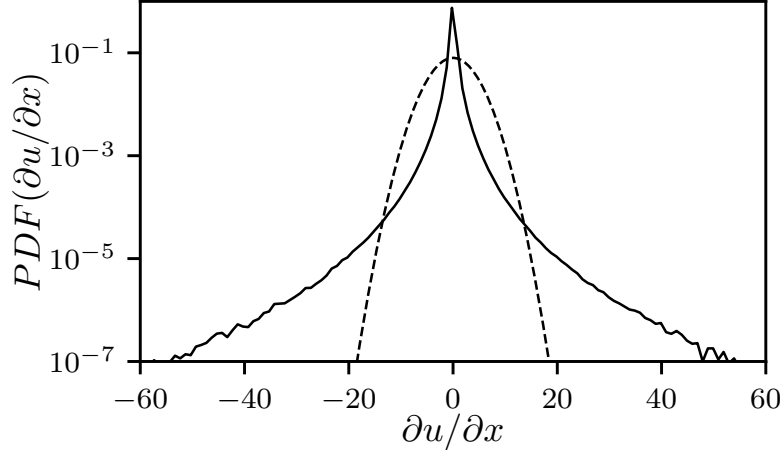


Figure 2.6: PDF of the velocity derivative with stretched tails (solid) compared with a Gaussian PDF (dashed).

spatial and temporal resolution errors on the stretched-exponentials. The universality of the stretched-exponentials is valuable for benchmarking the nature of small-scale turbulence.

2.3.6 Substructures in shear layers

Elsinga *et al.* [38] show that the analysis of extreme events and dissipation rate PDFs requires addressing significant local shear layers in the flow. The shear layer structure plays a role in the Reynolds-number dependence of the dissipation PDF and its tails. The shear layers are thin and intermittent regions of elevated dissipation rate against a background of turbulence with lower dissipation. Ishihara *et al.* [63] show up to ten times the increase in the dissipation rate inside the shear layers compared to the mean of the flow. When the Reynolds number is very high $Re_\lambda \approx 1000$, sublayers develop within the original shear layers. If the Reynolds number associated with these inner shear layers reaches $Re_\lambda \approx 1000$, then further inner structures develop. Analysing such extreme

Reynolds numbers is limited by the state-of-the-art computational capabilities, however, such a hierarchy of substructures inside structures is probable. The breakdown of the shear layer is different from the Kelvin-Helmholtz instabilities where the smaller vortices are not at a different structural scale [38]. The substructures can be seen as individual entities that possess the qualities of a different HIT region at the corresponding Reynolds number.

2.4 Turbulent boundary layers

Wall-bounded turbulence is another important canonical flow that has been studied extensively. The interaction of turbulence with solid boundaries plays an important role in practical applications by influencing the coefficient of friction and heat transfer at the wall.

Some of the initial characterization of wall-bounded turbulence was undertaken in channel flows [124, 141]. The pioneering DNS of Kim *et al.* [83] provided a database for low Reynolds number wall-bounded turbulence, which helped in development of improved RANS models [145]. The Reynolds number of the generated wall-bounded turbulence was restricted to $Re_\tau < 500$ for earlier DNS studies [104, 148], and Moser *et al.* [118] extended the resolution to $Re_\tau = 590$. Here, the Reynolds number is defined based on the friction velocity $U_\tau = \sqrt{\tau_w/\rho}$ such that, $Re_\tau = \delta U_\tau/\nu$, where δ and ν are the boundary layer thickness and kinematic viscosity, respectively. τ_w is the wall shear stress, calculated using the velocity gradients at the wall and ρ_w is the fluid density at the wall. DNS simulations have, over the years, progressed for simulating high-Reynolds number turbulence at Re_τ values from 1900 [27], 2003 [56], 4200 [100], and up to 5200 [92].

First, we introduce the well-known wall-scalings followed by a description of a structural approach to wall-bounded turbulence, namely the AEM. Subsequently, the transformations that relate the compressible wall-bounded turbulence to the incompressible regime wall-scalings are discussed.

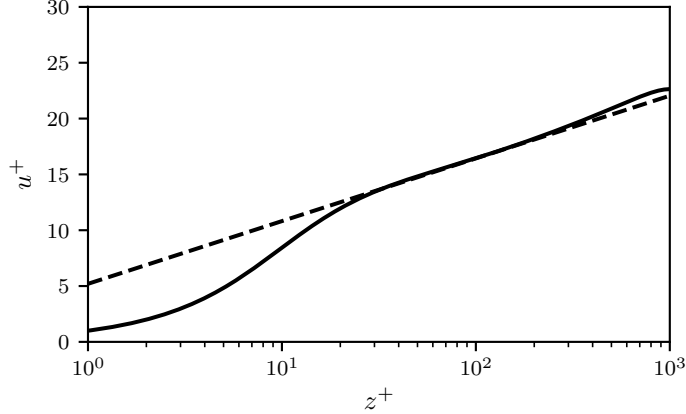


Figure 2.7: Mean-velocity profile (solid) at $Re_\tau = 1000$ from DNS results of Lee and Moser [92]. The dashed line shows the theoretical solution for log-layer from equation (2.17).

2.4.1 Incompressible TBL profiles

The mean streamwise velocity, given as $u^+ = u/U_\tau$, plotted against the wall-normal distance scaled in inner-wall units ($z^+ = z/\delta_\nu$), exhibits a linear-logarithmic region approximately between $30 \leq z^+ \leq 500$. Here, $\delta_\nu = \nu/U_\tau$ is the viscous wall unit. The wall is situated at $z^+ = 0$ and the viscous sublayer exists at $z^+ \leq 5$, see figure 2.7. The logarithmic layer can be reconstructed using the von Kármán equation [176]:

$$u^+ = \frac{1}{K_v} \ln(z^+) + B \quad (2.17)$$

Here, the von Kármán constant $K_v \approx 0.41$ and the constant $B \approx 5.2$ [59, 12]. The shear and normal Reynolds stresses are also computed from the DNS simulations. The mean velocity profile can be used to determine the temperature scaling in the incompressible regime. Temperature can be treated as a passive scalar when flow Mach number is small, since the incompressibility assumption is valid and the energy equation is decoupled from the momentum equation. In such cases, the mean-temperature profiles can be determined

in a manner analogous to the velocity-scaling of equation (2.17) [75], using:

$$\Theta^+ = \frac{1}{K_t} \ln(z^+) + B_t. \quad (2.18)$$

Here, $\Theta = T - T_w$, and the constants $K_t = 0.459$ and $B_t \approx 5.78$ [135, 133].

2.4.2 Attached-eddy model

Despite the high-Reynolds number and high-resolution TBL data available from DNS solutions, a few models of wall-bounded turbulence exist [112]. The pioneering work by Townsend [170] in this regard represented wall-bounded turbulence as a well-organized formation of randomly distributed eddies attached to the wall. AEM models are based on Townsend's hypothesis and provide a mechanism to model the generation of logarithmic region of the TBL [131].

AEM considers the eddy structure in the logarithmic region and beyond, and this eddy structure is unaffected by the viscous processes near the wall. Though the AEM hypothesis considers eddies attached to the wall, the eddies do not physically touch the wall. The model can be presumed to represent the effect of proximity of the wall to each eddy. The eddies are self-similar, their geometry scales with the distance of their centres to the wall at a constant energy density, and they have a fixed characteristic velocity scale. Considering the eddy height to be h_e , the location of the eddy at the wall ($z = 0$) being $\mathbf{x}_e = (x_e, y_e, z_e = 0)$, and the characteristic velocity scale U_o , the velocity field is given as:

$$u_i(x) = U_o \mathcal{F}_i \left(\frac{\mathbf{x} - \mathbf{x}_e}{h_e} \right), \quad (2.19)$$

The original hypothesis by Townsend [170] does not restrict the eddy structure, shapes or their organization, but only provides the functional relationship of the velocity field, given in equation (2.19) using functions \mathcal{F}_i . The eddies contribute to the Reynolds stresses weighted by the probability of occurrence of the eddy of a given size h_e :

$$\frac{u'_i u'_j}{U_o^2} = \int_{\delta_1}^{\delta} P_H(h_e) I_{ij} \left(\frac{z}{h_e} \right) dh_e, \quad (2.20)$$

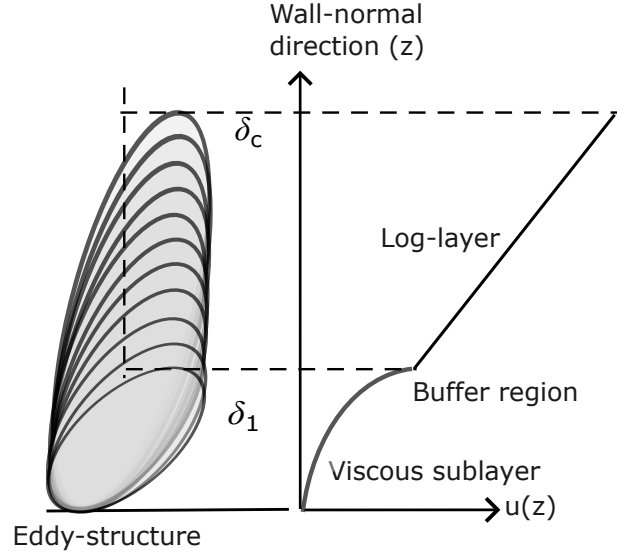


Figure 2.8: Hierarchy of eddies produces the logarithmic layer in AEM.

where, u'_i refers to the fluctuation in the i^{th} velocity component, and δ_1 and δ are the smallest and largest eddy sizes considered, respectively. $P_H(h_e)$ is the probability density for occurrence of an eddy of size h_e . I_{ij} is the intensity function that defines the contribution from each eddy to the Reynolds stresses, given as:

$$I_{ij} = \int_{\infty}^{\infty} \mathcal{F}_i \left(\frac{\mathbf{x}}{h_e} \right) \mathcal{F}_j \left(\frac{\mathbf{x}}{h_e} \right) d \left(\frac{x}{h_e} \right) d \left(\frac{y}{h_e} \right) \quad (2.21)$$

Townsend further made inferences on the magnitudes of the intensity functions by substituting the no-penetration condition on the wall, setting $\mathcal{F}_3(0) = 0$. This followed by the deduction of the forms of Reynolds stress profiles, and leading to the two important conclusions: (i) the characteristic velocity scale U_o equals the friction-velocity scale U_τ , and (ii) the population density of eddies is inversely proportional to the eddy size, and hence to the distance of their centres from the wall.

Although the analysis from Townsend did not specify the eddy-shapes, subsequent works considered specific geometries of the self-similar eddies, for example, the Λ -vortex in Ref. [130, 131] and Π -vortex in Ref. [131]. These works use the Biot-Savart law to reconstruct velocity fields from the vortex lines that constitute the eddies.

With the strong footing of AEM methods to model the wall-bounded turbulence, we explore the ODT method, which shares dominant features with the AEM model (see chapter 5), to approach the development of a model towards compressible TBL.

2.4.3 Wall-scalings in compressible regime

The wall-scalings for wall-bounded turbulence in the incompressible regime are not directly applicable to compressible TBL. Markov's hypothesis [117] states that the mean streamwise velocity profiles in the compressible TBL can be mapped to their incompressible counterparts, thus recovering the universal law of the wall.

Van Driest [174] first introduced a velocity transformation and extended the validity of Prandtl's mixing length assumption to the compressible regime, showing that the mean shear is a Mach number-independent function:

$$\frac{\partial \langle u \rangle_{VD}^+}{\partial z^+} = \sqrt{\langle \rho \rangle^+} \frac{\partial \langle u \rangle^+}{\partial z^+}, \quad (2.22)$$

where, $\langle \rho \rangle^+ = \langle \rho \rangle / \langle \rho \rangle_w$. Integrating equation (2.22) gives an expression for the transformed velocity profile:

$$\langle u \rangle_{VD}^+ = \frac{1}{U_\tau} \int_0^{\langle u \rangle^+} \sqrt{\langle \rho \rangle^+} d\langle u \rangle. \quad (2.23)$$

The van Driest scaling works well for adiabatic flows [134], however, it does not perform well in flows with non-zero heat transfer with compressibility effects [171, 175]. Trettel and Larsson [171] unified the transformations for the mean velocity and Reynolds stress and define the velocity scaling as:

$$\langle u \rangle_{TL}^+ = \int_0^{\langle u \rangle^+} \sqrt{\langle \rho \rangle^+} \left(1 + \frac{1}{2} \frac{1}{\langle \rho \rangle} \frac{d\langle \rho \rangle}{dz} z - \frac{1}{\langle \mu \rangle} \frac{d\langle \mu \rangle}{dz} z \right) d\langle u \rangle^+, \quad (2.24)$$

which shows much better collapse to the DNS results [192] in the viscous sublayer region as compared to the van Driest transformation. Zhang *et al.* [193] used a viscosity-weighted transformation for the mean-velocity profile and introduced the equilibrium of production and dissipation rate across the inner layer of the TBL. Griffin *et al.* [51] generalized

the approach of Zhang *et al.* [193] to diabatic flows and report applicability of the introduced scalings to different types of wall-bounded turbulence. The gradient of a semi-local Reynolds number was introduced in the wall-scalings from van Driest in Patel *et al.* [129]. Younes and Hickey [190] utilized the vorticity transport in the boundary layer and reported a collapse of profiles at supercritical pressures.

Although significant progress has been made in the mean-velocity scalings in the compressible regime, the scalings of the mean temperature for the compressible TBL have not received as much attention. Recently, Cheng and Fu [24] developed a new scaling showing an improved collapse for channel flows with adiabatic walls and high Mach number TBL with cold walls, compared with van Driest-type and semilocal scalings. The extension of the wall-scalings to compressible TBL with cold-walls is crucial for studying flow over cooled surfaces of hypersonic vehicles.

Chapter 3

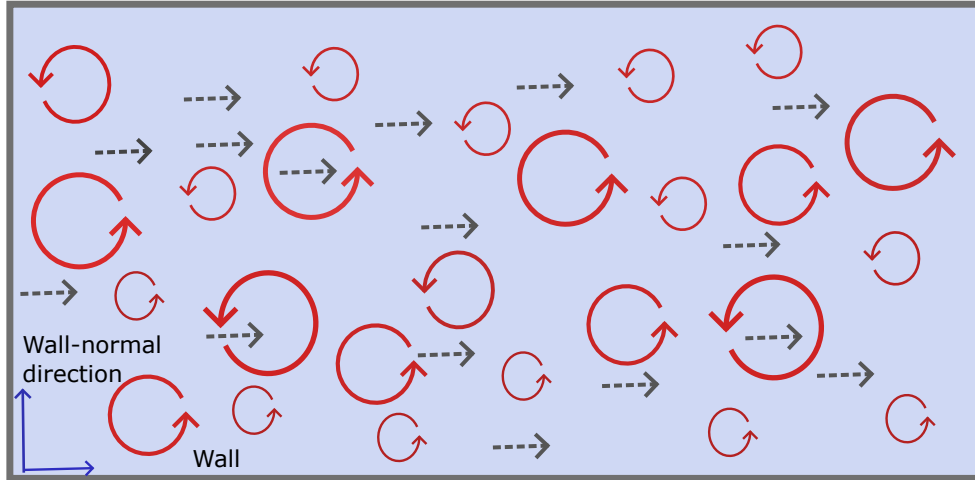
Methodology

3.1 Standard Incompressible ODT model

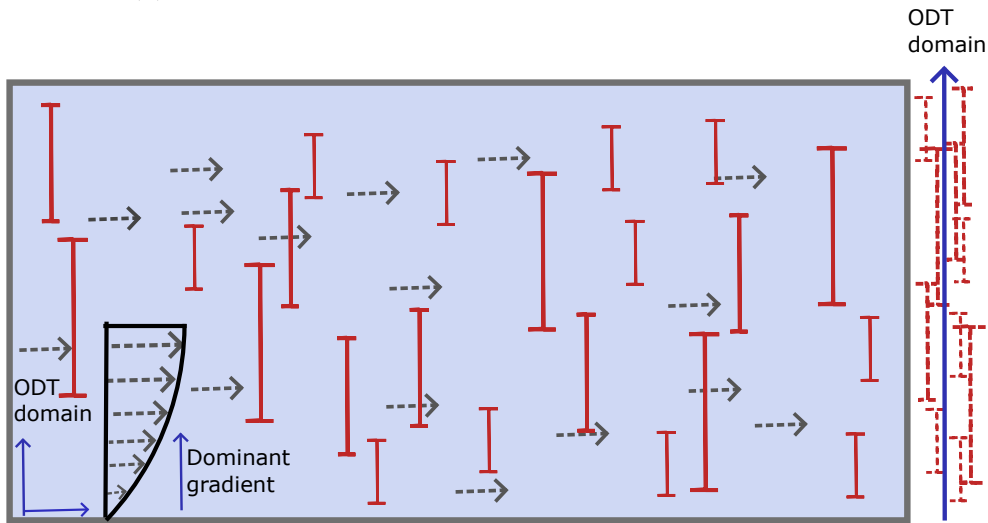
With the final objective of modelling compressible flows with the one-dimensional turbulence approach, we start with a description of the incompressible formulation.

3.1.1 View of the flow from ODT perspective

ODT superimposes turbulent eddies on an underlying base flow to model the turbulence. Due to the limitations of ODT's one-dimensional approach, it cannot incorporate three-dimensional realistic eddies. Instead, linear eddies are introduced to induce turbulent mixing which occurs predominantly along the direction of the dominant velocity gradient. For example, in the case of a turbulent boundary layer, the linear eddies align with the wall-normal direction, which corresponds to the dominant gradient of the mean flow. Hence, the linear eddies cause one-dimensional rearrangements of fluid properties along the ODT domain. Figure 3.1 visually depicts the linear eddies in turbulent boundary layer flow.



(a) Turbulent eddies in planar channel flow shown in red.



(b) Equivalent linear eddies in planar channel flow shown in red vertical bars. The linear eddies are applied over the one-dimensional ODT domain shown on the right.

Figure 3.1: Linear eddies in ODT representing turbulent stirring for turbulent boundary layer flow with underlying flow represented by dashed arrows. The ODT domain is oriented along the dominant gradient which is in wall-normal direction.

3.1.2 Overall structure of ODT model

(a) Underlying fluid flow

ODT model can represent either temporal flows, where flow evolves along the domain in time, or spatial flows, where the flow evolves in space in a direction normal to the ODT domain. In this work, we focus on the temporal flows, due to their relevance to the conducted studies.

Incompressible flow equations are solved in the ODT domain. For velocity, we utilize equation (3.1), and for scalars (such as temperature or other variables relevant to physical processes), we employ equation (3.2). The velocity equation applies to all velocity components, but is formulated using only one independent spatial variable, x , which represents the position along the ODT domain. The variable \mathbf{u} is the velocity along the ODT domain and θ is a scalar that is transported by the fluid. P and ρ represent the pressure and density, respectively. Diffusive coefficients are given by ν (kinematic viscosity) and κ_t (thermal diffusivity). u_i is the i^{th} component of the velocity and δ_{ij} is the Kronecker delta function.

$$\frac{\partial u_i}{\partial t} = \nu \frac{\partial^2 u_i}{\partial x^2} - \frac{1}{\rho} \frac{\partial P}{\partial x} \delta_{i1} \quad (3.1)$$

$$\frac{\partial \theta}{\partial t} = \kappa_t \frac{\partial^2 \theta}{\partial x^2} \quad (3.2)$$

A Lagrangian approach has been classically used as it simplifies the calculation of inter-cell fluxes. At each time step, the cell walls move with local speeds. In this system, mass flow does not occur through the cell boundary via convection and any mass transfer is solely caused by viscous diffusion. The cell-wall movements account for the advective terms in the NS equations.

(b) Superimposed turbulent stirring

In ODT, turbulent eddies in actual flows are represented as linear eddies as described in section 3.1.4. These linear eddy events involve rearranging the fluid segments along

the ODT domain. A predefined mapping known as *triplet-mapping* is used to simulate turbulent stirring, introducing higher wave numbers within the domain. Each eddy event is considered as an instantaneous occurrence. However, the total number of eddies is controlled by limiting the eddy acceptance. This ensures that the number of eddies between two flow evolution time steps remains limited.

3.1.3 Basic construct of ODT algorithm

A brief account of the different elements involved in the ODT model is provided below. We present a schematic of the solution procedure in figure 3.2.

1. Initialize the domain and set boundary conditions.
2. Solve fluid flow with governing equations. Compute fluxes and propagate the solution in time.
3. Sample an eddy and choose its size and position.
4. Check if the eddy is to be accepted. ODT domain variables like density and velocity are used for making the eddy acceptance decision, but their values are not updated until the eddy is implemented in step 5.
 - (a) Perform a triplet map at the proposed eddy location.
 - (b) Compute the energy change induced by the eddy.
 - (c) Find the eddy time scale that scales with the energy computed from the previous step.
 - (d) Compute the probability of acceptance of the eddy.
 - (e) Use the acceptance-rejection method to check if the proposed eddy is to be accepted.
5. If the proposed eddy is accepted, perform the triplet map and compute the energy change induced. This involves an identical repetition of steps 4(a) and 4(b). The ODT domain variables are updated only at this stage.

6. Perform energy redistribution based on the available energy from the previous step. This introduces isotropy in the system.
7. Irrespective of the case whether eddy is accepted or not, increment the simulation time by eddy sampling time Δt_{eddy} .
8. Solve for base flow intermittently between eddy implementations based on adequate flow-solution time step Δt_{solve} .
9. Adapt the mesh when the flow is solved or when an eddy is invoked.
10. End the simulation when the final time is reached.

3.1.4 Constitution of an eddy event

(a) Triplet map to represent an eddy

The triplet mapping is the mechanism in the ODT model that represents folding effects and compressional straining. The mapping increases the strain in the flow domain by making three compressed copies of the velocity profile. The three profiles are shrunk into the same total domain length of the eddy, thus increasing the spatial gradients in the flow. The middle part is reversed to maintain continuity in the field that is being rearranged. The mapping is designed to satisfy the measure-preservation and introduces no discontinuities as a result of the transformation. All velocity moments are conserved by the mapping. The triplet mapping $f(x)$ is described in the following equation:

$$f(x) = x_o + \begin{cases} 3(x - x_o), & x_o \leq x \leq x_o + \frac{1}{3}l \\ 2l - 3(x - x_o), & x_o + \frac{1}{3}l \leq x \leq x_o + \frac{2}{3}l \\ 3(x - x_o) - 2l, & x_o + \frac{2}{3}l \leq x \leq x_o + l \\ x - x_o, & \text{otherwise} \end{cases} \quad (3.3)$$

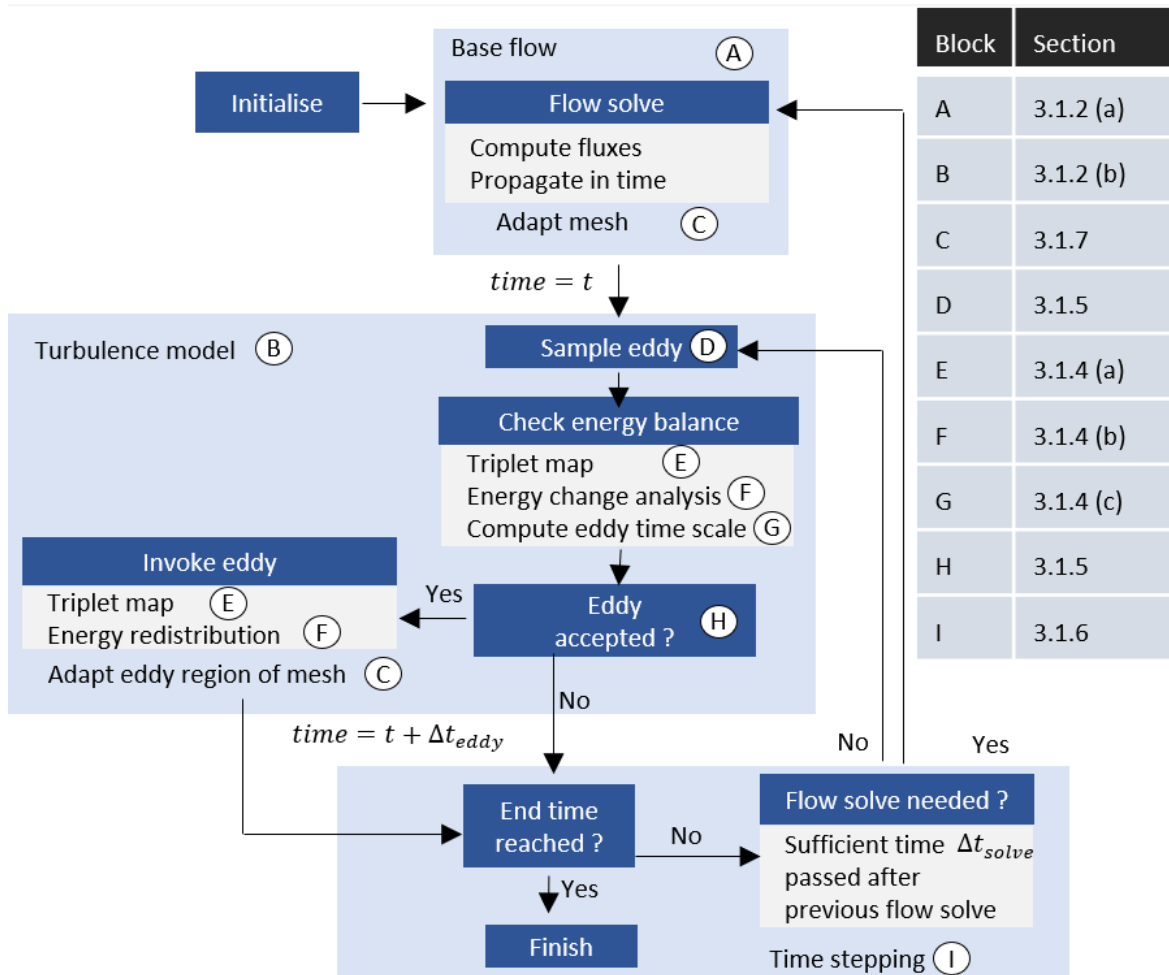


Figure 3.2: Schematic of ODT method, with specific details pertaining to each block indicated by corresponding section numbers in this thesis.

Here, x is the coordinate along the ODT-line, and x_o and l refer to the eddy start location and the eddy size, respectively.

The kernel function is defined as $K(x) = f(x) - x$, and it integrates to zero ($\int K(x)dx = 0$), which becomes instrumental in preserving momentum and energy when the eddy is invoked. The scalar variables outside the eddy are not affected by the eddy event map. The same mapping is used for all state variables in the state vector. The mapping occurs in such a way that the reverse mapping is always continuous. This means that any two fluid elements adjacent post-map are reasonably close to each other before the mapping. However, the reverse is rarely true, and the forward map is usually discontinuous. Figure 3.3 depicts the triplet mapping that transforms the profiles in an eddy event.

(b) Energy transfer formulation

An eddy event comprises two processes. First, a triplet map $f(x)$ transforms the domain with a rearrangement of fluid elements and associated scalar variables. Second, the post-map kernel transformation ($c_i K(x)$) applies only to the velocity components, causing the energy redistribution between them.

$$\left. \begin{aligned} u_i(x) &\longrightarrow u_i(f(x)) + c_i K(x) \\ \theta_i(x) &\longrightarrow \theta_i(f(x)) \end{aligned} \right\} \quad (3.4)$$

The capability to handle low-Mach number flows with variable density is also available in the classical ODT model. However, the effects of compressibility on the flow solution are not included. In case of variable density flows, a third term is introduced in the velocity map to add a degree of freedom (where $J(x) = |K(x)|$) for the energy change, which is shown in equation (3.5).

$$u_i(x) \longrightarrow u_i(f(x)) + c_i K(x) + b_i J(x) \quad (3.5)$$

The energy is redistributed post-triplet map via the term with the kernel function. In addition, momentum is altered due to the third term in the velocity transformation.

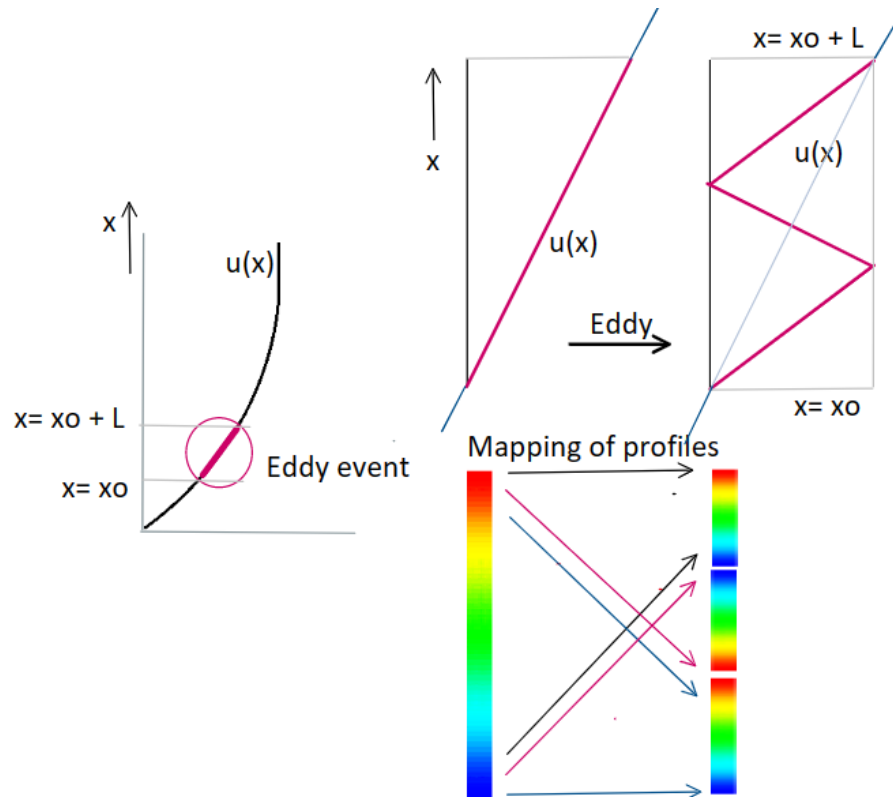


Figure 3.3: Triplet mapping in an eddy event. The representation of the eddy in colour scale shows the continuity in the post-eddy velocity profile (blue refers to the minimum and red is the maximum value of velocity).

An energy balance pertaining to the kernel transformation is used to evaluate the coefficients c_i and b_i . We represent post-map density and velocity profiles after the map as $\bar{\rho}$ and \bar{u}_i , respectively, and the velocity profiles after the kernel transformation as $\bar{\bar{u}}_i$. The energy change in the post-triplet-map transformation of the eddy event for the i^{th} component of the velocity, per unit the notional cross-sectional area normal to the ODT domain, is given as:

$$\Delta E_i = \frac{1}{2} \int_{x_o}^{x_o+l} \bar{\rho}(\bar{\bar{u}}_i^2 - \bar{u}_i^2) dx, \quad (3.6)$$

Substituting expressions for modified velocity profiles, we get:

$$\Delta E_i = \frac{1}{2} \int_{x_o}^{x_o+l} \bar{\rho}((\bar{u}_i + c_i K + b_i J)^2 - \bar{u}_i^2) dx \quad (3.7)$$

Defining the terms F_i and G for conciseness, the energy change can be expressed as follows. F_i and G are described in equations (3.10) and (3.11), and other necessary definitions are provided here.

$$\Delta E_i = F_i c_i + G c_i^2 \quad (3.8)$$

$$H = \frac{\rho_K}{\rho_J} \quad (3.9)$$

$$F_i = \rho_{iK} - H \rho_{iJ} \quad (3.10)$$

$$G = \frac{1}{2}(H^2 + 1)\rho_{KK} - H\rho_{JK} \quad (3.11)$$

$$b_i = -H c_i \quad (3.12)$$

In the equations presented above, we represent the integrals involving densities and/or velocities using simplified notations, which are described as follows.

$$\begin{aligned} \rho_K &= \int \bar{\rho} K(x) dx & \rho_{KK} &= \int \bar{\rho} K^2(x) dx \\ \rho_J &= \int \bar{\rho} J(x) dx & \rho_{JK} &= \int \bar{\rho} J(x) K(x) dx \\ \rho_{iK} &= \int \bar{\rho} \bar{u}_i(x) K(x) dx & \rho_{iJ} &= \int \bar{\rho} \bar{u}_i(x) J(x) dx \end{aligned}$$

Solving equation (3.8) gives an expression for c_i in terms of desired energy change ΔE_i ,

$$c_i = \frac{1}{2G} \left(-F_i + \text{sgn}(F_i) \sqrt{F_i^2 + 4G\Delta E_i} \right), \quad (3.13)$$

where, the function $sgn(F_i)$ selects the physical branch of the solution of equation (3.8). This ensures that c_i approaches zero when the energy change ΔE_i is negligible. Maximizing the energy transfer, we arrive at the expression for the available energy in the i^{th} velocity component Q_i , which is given as:

$$Q_i = \frac{F_i^2}{4G} \quad (3.14)$$

The energy transfer due to the kernel function tends to drive the flow towards isotropy in the ODT framework, and intercomponent energy transfer is given in terms of a parameter ω in equation (3.15). A value of $\omega = 1$ leads to the highest energy transfer to the other two velocity components, while $\omega = 0$ represents zero energy transfer. $\omega = 2/3$ leads to the equipartition of energy into the three velocity components.

$$\Delta E_i = \omega \left(\frac{Q_j}{2} + \frac{Q_k}{2} - Q_i \right) \quad (3.15)$$

Substituting the energy change for the i^{th} velocity component from equation (3.15) and the maximum energy content from equation (3.14) into equation (3.13), we get the final expression for c_i :

$$c_i = \frac{1}{2G} \left(-F_i + sgn(F_i) \sqrt{(1 - \omega)F_i^2 + \frac{\omega}{2}F_j^2 + \frac{\omega}{2}F_k^2} \right) \quad (3.16)$$

The resulting c_i can be used to evaluate b_i using equation (3.12).

(c) Eddy time-scale

To assign a time scale τ to the eddy under consideration, we consider the kinetic energy associated with the eddy that scales as:

$$\frac{1}{2}m \cdot u^2 \approx \frac{1}{2}\langle \rho \rangle (lA_c) \frac{l^2}{\tau^2} = \frac{1}{2} \frac{\rho_{KK}}{KK} (lA_c) \frac{l^2}{\tau^2}, \quad (3.17)$$

where, $\langle \rho \rangle = \rho_{KK}/(KK)$ represents the average density in the eddy region and $KK = \int_{x_o}^{x_o+l} K^2(x)dx$. The velocity scale is given by l/τ and the affected volume is defined as

lA_c , where l is the eddy size and A_c is the notional cross-sectional area normal to the ODT domain. The eddy kinetic energy per unit area A_c is given by:

$$E_{kin} = \frac{1}{2} \frac{\rho_{KK}}{KK} \frac{l^3}{\tau^2}, \quad (3.18)$$

which, on rearrangement, gives an expression for the time scale (τ) of an eddy with start location x_o , length l , at an instant of time t :

$$\frac{1}{\tau} = \sqrt{\frac{2KK}{\rho_{KK}l^3} E_{kin}} \quad (3.19)$$

Hence, each eddy is an instantaneous event, but has a characteristic time scale associated with it. E_{kin} scales with the available energy of the specified velocity component ($i = 1$ in this case), which is given as:

$$E_{kin} \sim Q_1'' = Q_1 + \Delta E_1 = (1 - \omega)Q_1 + \frac{\omega}{2}(Q_2 + Q_3) \quad (3.20)$$

The available energy has a strong dependence on $(1/l^2) \int_{x_o}^{x_o+l} u_i(f(x))K(x)dx$, which is particularly elevated if a small-scale eddy applies on a high velocity gradient region. More terms are added to E_{kin} to account for other sources or sinks of energy, for example the terms E_{vp} and E_{pe} , which represent the viscous penalty and a potential energy term, respectively, and we get:

$$\frac{1}{\tau} = \sqrt{\frac{2KK}{\rho_{KK}l^3} (E_{kin} - ZE_{vp} - E_{pe})}. \quad (3.21)$$

Here, the viscous penalty is given by $E_{vp} = \mu^2/(2\rho_{eddy}l)$, where, ρ_{eddy} represents the average density within the considered eddy, μ is the dynamic viscosity, and Z is a parameter used to adjust the viscous penalty. E_{vp} affects eddy selection but not the implementation of a selected eddy. E_{vp} sets the lower limit on the allowable eddy size as defined in Ref. [6], thus adding a second mechanism for viscous dissipation in addition to the viscous diffusion terms in the governing equations. The viscous penalty coefficient, Z , is set to zero if small eddy suppression is to be omitted.

A potential energy term E_{pe} is used in ODT formulations to model the effect of other forces involved in the system. The term E_{pe} can be used to increase the eddy acceptance with or without direct addition of energy in the post-triplet map velocity transformation by adding E_{pe} in the expression for c_i in equation (3.16). Direct energy addition is introduced if an external mechanism takes part in the flow physics. For example, unsteady dilatation has been accounted for using the E_{pe} term [74].

We introduce a notation for a function $\chi(x_o, l; t)$ of an eddy, which has a start location x_o , length l , and applies instantaneously over a frozen-in-time flow state at time t . For example, $\tau(x_o, l; t)$ is the time-scale of an eddy that extends from x_o to $x_o + l$, computed at an instant of time t .

3.1.5 Eddy sampling and acceptance

We introduce the rate of the eddy distribution, denoted as $\lambda_r(x_o, l; t)$, which represents the number of eddies per unit length of domain, per unit eddy size in a unit time. Therefore, $\lambda_r(x_o, l; t)dl$ represents the number of eddies within the size range from l to $l + dl$, per unit length along the ODT line, per unit time. By employing dimensional arguments, we establish a relationship between the eddy rate distribution and the eddy size, as well as the mean eddy time-scale, given as:

$$\lambda_r(x_o, l; t) = \frac{1}{l^2 \tau(x_o, l; t)} \quad (3.22)$$

The eddy time-scale τ is a physical parameter influenced by instantaneous parameters such as velocity $u(x, t)$, and changes with the evolution of the system. The eddy rate (Λ) is defined as the average number of eddies per unit time (including eddies of all sizes and start locations), and this can be calculated as:

$$\Lambda(t) = \int_{x_o} \int_l \lambda_r(x_o, l; t) dx_o dl \quad (3.23)$$

The ratio $\lambda_r(z_o, l; t)/\Lambda(t)$ gives an instantaneous joint probability density function for the occurrence of an eddy of size l and start location x_o , and requires computation of

$\tau(x_o, l; t)$ for each eddy considered. In principle, the eddies could be sampled via a discrete Poisson process at the rate $\Lambda(t)$, depending on the instantaneous system state, and the admittance of the eddy could be tested based on the joint PDF given by $\lambda_r(z_o, l; t)/\Lambda(t)$. However, continually re-evaluating $\Lambda(t)$ and $\tau(z_o, l; t)$ at each time-varying frozen flow state is computationally too expensive, and we use an indirect method to sample eddy position.

The probability density of the eddy occurrence is rather factored into two *guessed* probability distributions, $g_1(z_o)$ and $g_2(l)$, for eddy start locations and sizes, respectively. These distributions can be arbitrary, but subject to some weak constraints, such as limitations on the eddy size. In the standard ODT model, the position x_o is uniformly sampled in the domain and the eddy size distribution is set as (with $s = 1$):

$$g_2(l) = \frac{c_1}{l^{s+1}} \exp\left(-\frac{c_2}{l^s}\right). \quad (3.24)$$

Here, the parameters c_1 and c_2 are set to approximately achieve the desired flow-specific eddy-size distribution. The guessed distributions g_1 and g_2 have negligible influence on attained simulation results.

A probability for eddy acceptance is defined using the eddy rate distribution λ_r and guessed distributions for eddy start location and size, g_1 and g_2 , respectively:

$$p_e = \frac{\lambda_r(x_o, l; t) dx_o dl \Delta t_e}{g_1(x_o) g_2(l) dx_o dl} = \frac{\lambda_r(x_o, l; t) \Delta t_e}{g_1(x_o) g_2(l)}. \quad (3.25)$$

Here, Δt_e is the mean eddy-sampling time interval, which is typically chosen to be small enough so that eddies are sampled at a rate much higher than the prescribed rate $\Lambda(t)$. Using expression for $\lambda_r(x_o, l; t)$ from equation (3.22) and introducing the ODT parameter C to modify the turbulence intensity, the sampled eddy is then subject to an acceptance-rejection method based on the probability:

$$p_e = \frac{C \Delta t_e}{g_1(x_o) g_2(l) l^2 \tau}, \quad (3.26)$$

The two-step procedure of discrete sampling of eddies followed by the acceptance-rejection procedure produces the physically prescribed ensemble of eddies. The two-step procedure approximately attains the required eddy statistics if it is ensured that Δt_e is much lower than the inverse of net eddy rate Λ [6].

3.1.6 Time-stepping procedure

The simulation begins at $t = 0$ with the fluid flow initial conditions. Subsequently, the eddy sampling procedure takes place and the time progresses according to the eddy sampling time step Δt_{eddy} . The Poisson process randomly selects Δt_{eddy} with a mean value of Δt_e (as displayed in equation (3.27)). It is important to note that the eddy time-step differs from the eddy time-scale, which is utilized for computing the eddy acceptance probability.

$$\Delta t_e = K_e P_{avg} \frac{L^2}{\nu N^3} \quad (3.27)$$

The constants K_e and P_{avg} are determined based on the required numerical accuracy, while L represents the length of the domain. The variable ν represents the kinematic viscosity, and N denotes the number of grid points.

Regardless of whether the eddy is accepted or not, the simulation time is increased by the value of Δt_{eddy} . As the simulation time progresses, we check if a sufficient amount of time has passed since the last update of the NS equations. The time interval between two consecutive flow advancements is denoted by Δt_{solve} (see equation 3.28). The NS equations are then advanced over the time interval Δt_{solve} .

$$\Delta t_{solve} = \frac{dx_{min}^2}{\nu}, \quad (3.28)$$

where, dx_{min} is the minimum grid size.

3.1.7 Adaptive meshing

Adaptive meshing plays a crucial role in ODT and is necessary to enhance resolution in regions where an eddy is present. The presence of an eddy leads to abrupt changes in profiles, which justify the need for an increased local resolution.

The adaptive meshing mechanism consists of two fundamental components. Firstly, there is the grid density, which ensures a fixed number of grid points per unit arc length of the profile. This approach guarantees a higher grid resolution in areas with steep gradients.

The second aspect of adaptation involves the splitting and merging of cells. This occurs when a cell size exceeds the maximum limit, falls below the minimum allowable cell size, or differs from its neighboring cells by a factor of 2.5 or more. Cell splitting and merging help maintain the desired grid characteristics. While these steps ensure a suitable distribution of grid points, excessive adaptation can result in numerical transfers of variables that are not physically meaningful. These numerical transfers occur as a result of interpolation or summation of flow variables after cell splitting or merging, respectively.

The detailed description of the original ODT adaptation algorithm can be found in the work by Lignell *et al.* [94].

3.1.8 Benchmarking with turbulent boundary layer

We utilize ODT to simulate the velocity profile in an incompressible channel flow. The flow is driven by a constant pressure gradient between two infinite parallel plates, and the flow variables exhibit characteristic changes in the wall-normal direction. In this context, linear eddies oriented perpendicular to the wall represent the turbulent shearing of the flow in that particular direction.

In the simulation of planar channel flow, two infinite plates are considered, separated by a distance of 2 m along the z -axis. A pressure gradient of -0.0025 Pa/m is applied along the x -direction. The kinematic viscosity is set to $5.0 \times 10^{-5}\text{ m}^2/\text{s}$, and the density of the fluid is assumed to be 1 kg/m^3 .

The ODT line is set along the z -direction, and the specific model parameters are set as: $C = 350$, $Z = 7$ and $\omega = 0.66667$. The initial grid consists of 200 nodes. All the velocity components are set to zero at both walls of the channel. The simulation is initialized with a parabolic streamwise-velocity profile, and zero wall-normal and spanwise velocities. However, the solution is found to be independent of the assumed initial velocity profiles. The ODT simulation is carried out for a total duration of 10,000 seconds and on average each simulation takes approximately 360 seconds of CPU time.

Comparison of results with DNS data

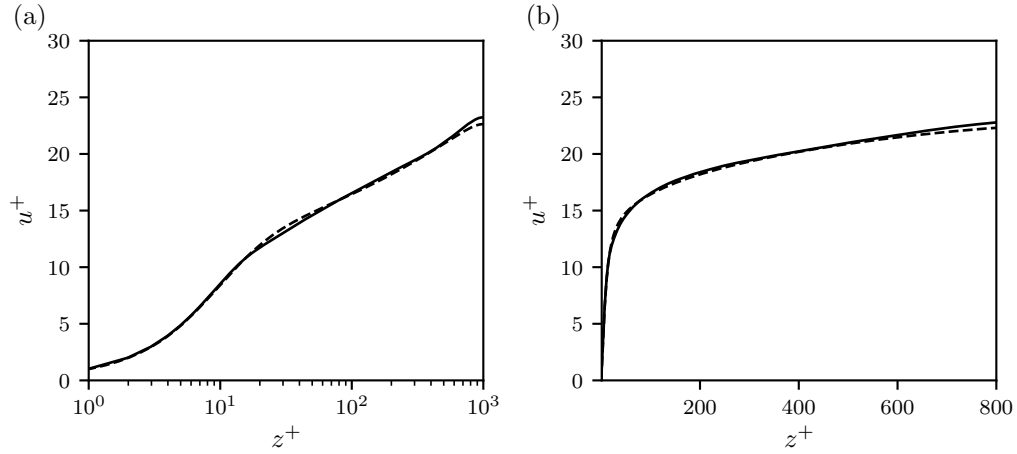


Figure 3.4: Normalized mean-velocity profiles from ODT (solid) and DNS results [92] (dashed) with (a) logarithmic and (b) linear z^+ .

We compare the results from the ODT model with the DNS results for channel flow simulations at a Reynolds number (Re_τ) of 1000 [92]. The ODT simulation generates multiple sets of velocity data at predefined intervals, which are used to compute the mean streamwise velocity profile in the wall-normal direction, along with the root-mean square velocity fluctuations. Figure 3.4 compares the ODT results with that from DNS. The mean-velocity profiles from ODT exhibit a remarkable similarity to the values obtained from high-fidelity DNS simulations, despite the fact that the ODT requires only a fraction of the computational time needed by the DNS. Figure 3.5 compares the ODT predictions for root-mean-square velocity fluctuations and the corresponding DNS results. Notably, it is observed that the root-mean-square velocity fluctuations for the v and w components are equal in ODT, in contrast to the DNS results, which can be attributed to the absence of three-dimensional effects in ODT.

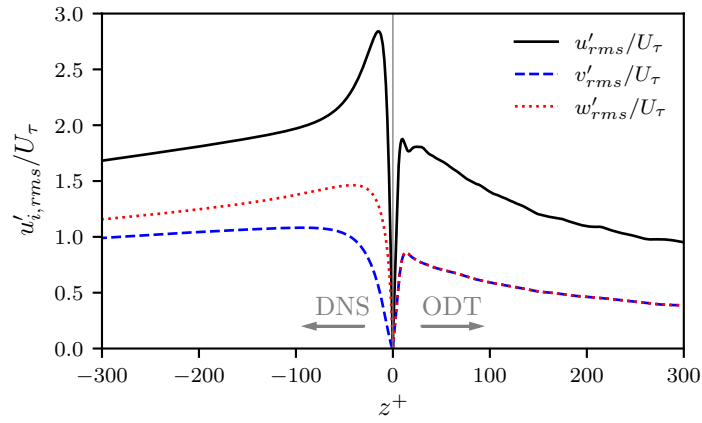


Figure 3.5: Variation of normalized root-mean-square velocity fluctuations. The positive z^+ values represent the results obtained from the ODT model, while negative z^+ values indicate the DNS results for the turbulent boundary layer. To enhance the intuitive presentation of DNS data, the results are flipped along the vertical axis, resulting in negative z^+ values. DNS results from Ref. [92].

3.1.9 Attempts to introduce compressibility effects to standard ODT

Jozefik *et al.* [73] utilized the ODT approach to model RM instability, while introducing some compressibility effects. The ODT model used in their study was not fully compressible and pressure changes were computed based on volume variations resulting from cell expansion or contraction. RM instability refers to the amplification of turbulence when a shockwave passes through a sharp density change at a contact discontinuity. The researchers [73] employ a model of RM instability within the framework of the sod-shock tube problem, where the ODT domain is aligned in the streamwise direction. By considering the interaction of a wall-reflected shock with the contact discontinuity, a turbulent mixing zone is created. This phenomenon is represented using a potential energy formulation in the pseudo-compressible framework.

3.2 Development of compressible ODT model

The classical, incompressible ODT algorithm has matured since Kerstein's seminal work on the topic. With the continual increase in the interest for high-speed, multi-physics flows, the classical formulations must be adapted to tackle these new problems. Building on the theoretical framework presented in section 3.1, this section discusses the modifications and additions to the ODT algorithm carried out in this work for use in compressible flow problems.

Gao *et al.* [45] extended the work by Jozefik *et al.* [73] to achieve a fully compressible solution and applied the method to study the Shock-Turbulence Interaction (STI) in the context of the RM instability. Chen *et al.* [20] utilized the fully compressible formulation to model compressible turbulent boundary layers.

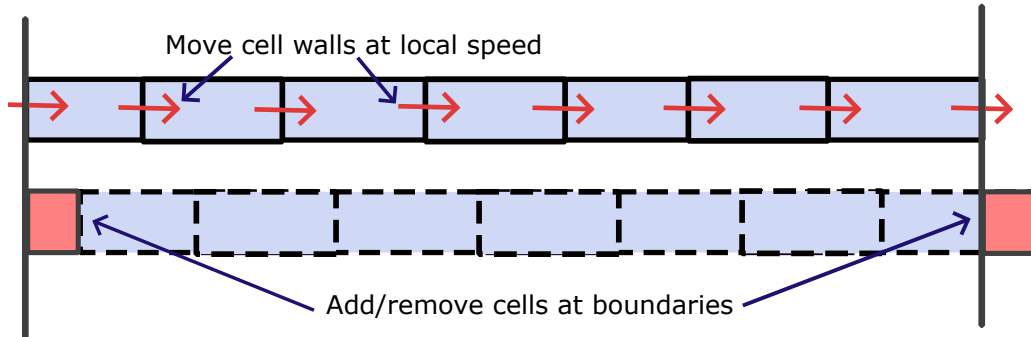


Figure 3.6: Complications that arise in Lagrangian framework.

3.2.1 Inadequacy of standard ODT model

The standard ODT method, designed for incompressible flows, employs a Lagrangian framework to solve for the underlying flow occasionally interrupted by stochastic eddy events. In this Lagrangian approach, the cell boundaries are moved using locally computed velocities, allowing for mass transfer only through diffusion and preventing advective transfer across cell faces.

The extension of the Lagrangian approach to compressible flows encounters certain difficulties. Accurately modelling compressible flows requires capturing sharp discontinuities, which are often accompanied by rarefaction phenomena. Jozefik *et al.* [73] attempted to incorporate compressibility in a pseudo-compressible Lagrangian solver, but the treatment of volume change was approximate. Adapting well-known algorithms such as approximate Riemann methods to the Lagrangian framework, which are better suited for compressible flows, is a non-trivial task that necessitates extensive numerical investigations. Moreover, handling inflow and outflow conditions in the Lagrangian approach requires adding or removing cells at boundaries (shown in figure 3.6). This process is prone to errors and inconsistencies. Therefore, to address these limitations, ODT has been enhanced by developing a fully compressible model based on an Eulerian framework in the present work.

3.2.2 Measure-preservation in eddy events

In the standard ODT framework, the triplet map preserves the measures of each variable separately. In compressible ODT, we use the map on conservative variables to match the conservative nature of the flow solution. By applying the triplet map to conservative variables, we achieve the same outcome as by mapping individual primitive variables. This is because a specific set of conservative variables corresponds to a unique set of primitive variables. Focussing only on conservative variables for eddy events reduces the number of operations required. Furthermore, it is reasonable to consider that eddies cause turbulent transfer of conservative variables and it is appropriate to model conservative eddies in the compressible ODT framework.

3.2.3 Mathematical formulation

The compressible flow equations are solved within the one-dimensional ODT domain. To construct the compressible flow model, we develop a combination of the Weighted Essentially Non-Oscillatory (WENO) 5th-order scheme and the Harten-Lax-van Leer-Contact (HLLC) solver, based on the work of Houim and Kuo [55]. In the ODT modelling, partial derivatives are only considered along the ODT line. Stresses are computed using simplified deviatoric stress components, employing a one-dimensional approximation, while heat transfer relies on the local temperature gradient. Here, T is the temperature, μ is the dynamic viscosity, k_t is the thermal conductivity, σ_{ij} is the ij^{th} component of the stress tensor and q_i represents the heat flux along the i^{th} direction.

$$\frac{\partial \rho}{\partial t} + \frac{\partial(\rho u_1)}{\partial x} = 0 \quad (3.29)$$

$$\frac{\partial(\rho u_1)}{\partial t} + \frac{\partial(\rho u_1^2)}{\partial x} = -\frac{\partial P}{\partial x} + \frac{\partial \sigma_{11}}{\partial x} \quad (3.30)$$

$$\frac{\partial(\rho u_2)}{\partial t} + \frac{\partial(\rho u_1 u_2)}{\partial x} = \frac{\partial \sigma_{21}}{\partial x} \quad (3.31)$$

$$\frac{\partial(\rho u_3)}{\partial t} + \frac{\partial(\rho u_1 u_3)}{\partial x} = \frac{\partial \sigma_{31}}{\partial x} \quad (3.32)$$

$$\frac{\partial(\rho(e + u^2/2))}{\partial t} + \frac{\partial(\rho u_1(e + u^2/2))}{\partial x} = -\frac{\partial(Pu_1)}{\partial x} - \frac{\partial q_x}{\partial x} + \frac{\partial(u_1\sigma_{11})}{\partial x} + \frac{\partial(u_2\sigma_{21})}{\partial x} + \frac{\partial(u_3\sigma_{31})}{\partial x} \quad (3.33)$$

$$\sigma_{21} = \mu \frac{\partial u_2}{\partial x}, \quad \sigma_{31} = \mu \frac{\partial u_3}{\partial x}, \quad \text{and } \sigma_{11} = 2\mu \frac{\partial u_1}{\partial x} + \lambda_s \frac{\partial u_1}{\partial x}, \quad (3.34)$$

$$q_x = -k_t \frac{\partial T}{\partial x} \quad (3.35)$$

The variation in μ with temperature T is given by a power law, for example, $\mu \sim T^{3/4}$, and the second coefficient of viscosity is given by $\lambda_s(T) = -2/3 \mu(T)$.

The simulation is advanced with the eddy sampling time Δt_{eddy} and the flow solution is carried out intermittently based on the desired time interval between two flow-advancements Δt_{solve} . We find the characteristic speeds of information propagation based on flow velocity (u) and the isentropic speed of sound (c). The time step for the flow solution is chosen by defining an acoustic time-scale corresponding to the maximum speed of information propagation ($|u|+|c|$) and the minimum cell size.

We adopt a similar approach to implement eddies as described in the context of incompressible ODT. However, in the compressible ODT framework, the eddies are conservative, as depicted in figure 3.7. As a result, the triplet map is applied over conservative variables, enabling the direct representation of turbulent transport of mass, momentum, and energy. This approach allows us to capture the collective behaviour of these variables instead of considering them individually as primitive variables such as density, velocity, and temperature.

In this study, improvements have been made to the algorithm responsible for merging and splitting cells in the ODT framework. The original ODT method ensures conservation of mass and momentum during cell merging. To enhance the computational accuracy of the compressible flow model, we introduced the preservation of total energy (including enthalpy and kinetic energy).

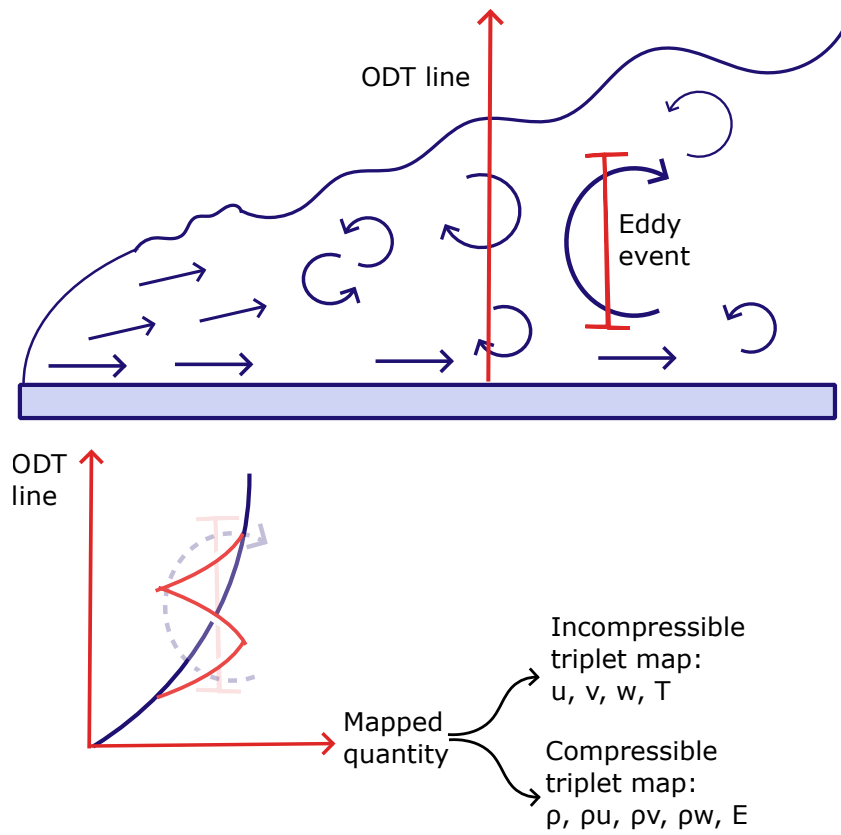


Figure 3.7: Eddy event construction for compressible flows depicted for the case of a turbulent boundary layer.

Validation of compressible flow model

We verify the flow model by simulating the classical Sod shock-tube problem [160]. The domain configuration and the initial conditions are based on the work of Jozefik *et al.* [73], with the domain length of 1 m , and a jump in the thermodynamic properties of stagnant air is initialized at $x = 0.5 m$. The initialized temperature of air is 300 K throughout the domain and the pressure jumps from 100 kPa to 10 kPa across the discontinuity.

Since the pressure drops from left to right across the discontinuity in the initialized condition, a shock and a rarefaction wave originate at the location of the discontinuity. The shock wave moves to the right and the rarefaction wave in turn travels to the left. A contact discontinuity also develops as represented by a density jump in between the regions of the shock and the rarefaction wave. We compute the propagation of the shock wave, the contact discontinuity and the rarefaction wave, and show a close match with the results of Jozefik *et al.* [73] in figure 3.8. Pressure, density, and velocity profiles are compared 0.4 ms after the initialization.

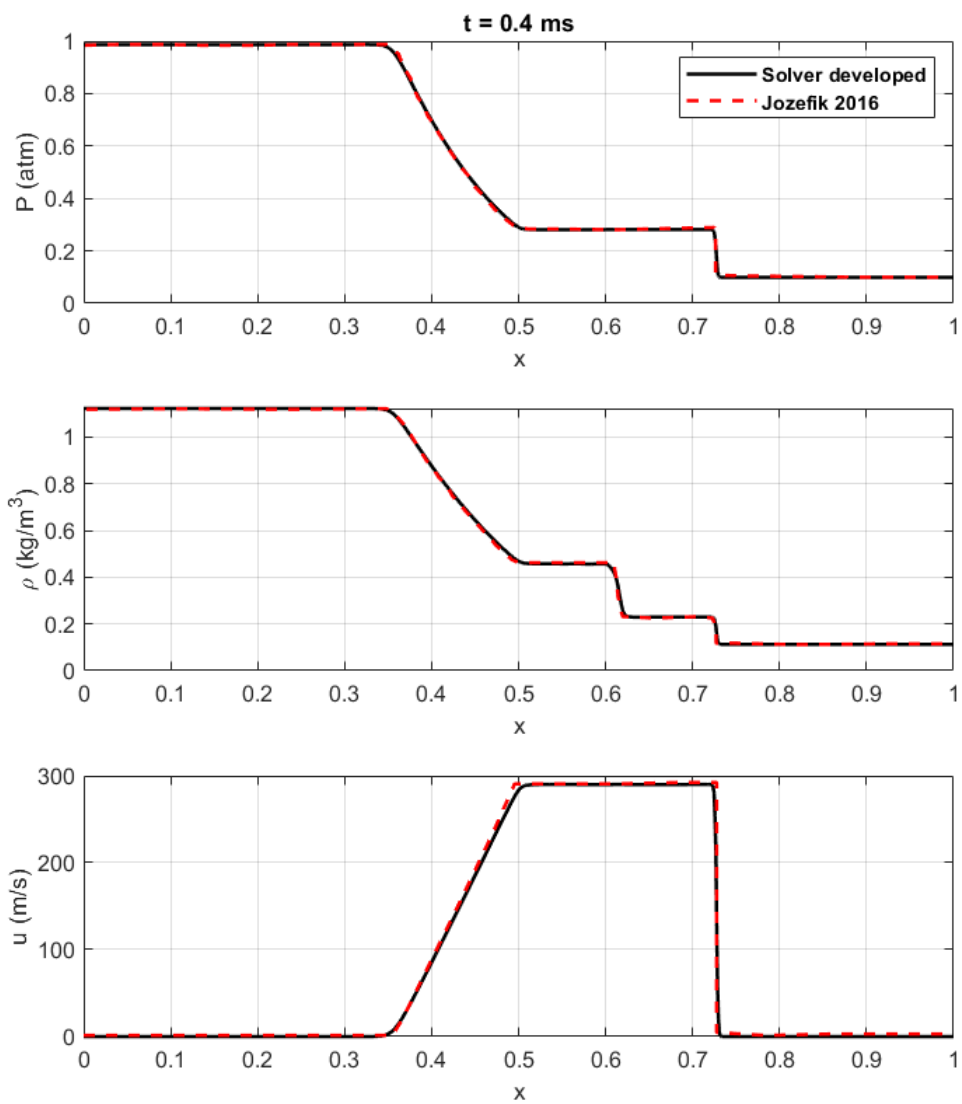


Figure 3.8: Sod shock-solution in the compressible model developed.

Chapter 4

High-order statistics and extreme fluctuations in stationary turbulence via one-dimensional turbulence

Associated reference:

Nath, Pranav and Hickey, Jean-Pierre, “High-order statistics and extreme fluctuations in stationary turbulence via one-dimensional turbulence”, *Physical Review Fluids* 10, 054602 (2025) <https://link.aps.org/doi/10.1103/PhysRevFluids.10.054602>.

Abstract

Rare but extreme dissipation events are dynamically important, but their numerical simulation represents a formidable computational challenge given the scale separation of high Reynolds number turbulence. Here, we explore the potential of a reduced dimensionality model, namely, the ODT approach, to represent the structure and evolution of forced HIT. We extend the classical ODT formulation to an Eulerian framework by solving the fully compressible equations (solved at low turbulent Mach numbers) including the modelling of all three velocity components. We computed temporally and spatially resolved simulations of forced HIT at Reynolds numbers up to $Re_\lambda = 5428$ and validated against

theoretical and numerical published results. More specifically, we show that the developed compressible formulation of ODT can capture many of the quantitative characteristics of HIT such as the turbulent spectrum, the normalized dissipation rate, the skewness, energy flux, and intermittency, among others, although accompanied by strong compressible effects inherent in the turbulence forcing formulation of the model. The computational tractability of ODT enables a detailed study of the generation of extreme localized dissipation in turbulence. Conditional sampling reveals that occurrence of extreme events is positively correlated with a high frequency of eddies at a specific spatial location and within a short time window.

4.1 Introduction

Turbulence is one of the oldest unresolved problems in classical physics in part due to the non-linearities in the governing equations which result in a complex multiscale problem. As the relative effects of viscosity become smaller with an increase in Reynolds number, the scale separation increases, imposing limitations to both experiments and simulations. Yet, the behaviour of the smallest scales of turbulence at high Reynolds number remains of great scientific interest. Kolmogorov [87] postulated his hypothesis on the universality of the smallest scales in turbulence in terms of statistical isotropy. As one of the fundamental concepts in modern turbulence theory, this hypothesis has motivated the need for detailed and controlled experiments of homogeneous isotropic turbulence (HIT), see, e.g. Warhaft [178], to confirm the behaviour the smallest scales at these extreme Reynolds numbers. The smallest scales are also characterised by strong intermittency, which highlights the importance of extreme viscous dissipation events despite their rare occurrence [38]. Although experiments remain vital for understanding high-Re turbulence, scale-resolving simulations provide detailed spatial and temporal information necessary to characterising these extreme events.

DNS of HIT, used to study turbulence at very-high Reynolds numbers, demand extreme spatial resolution to adequately resolve all scales; the resolution is even more severe

to characterise extreme dissipation, requiring sub-Kolmogorov resolution [187]. The resolution imposes strict time-advancement constraints and immense computational resources. The state-of-the-art DNS studies of HIT reach a Reynolds number, based on the Taylor length scale ($Re_\lambda = u'\lambda/\nu$), of about 2,500 which requires a resolution of more than 32 trillion ($32,768^3$) grid points [185]. A further increase in Re_λ only grows the required degrees of freedom of the numerical problem, while increasing the constraint on the time advancement. As the resolution requirement is directly tied to the ratio of the largest length scale (L) to the smallest length scale η , known as Kolmogorov length scale, of the problem, the degrees of freedom required to spatially resolve all the scales are:

$$df_{points} \propto \left(\frac{L}{\eta}\right)^n \sim \left(Re_\lambda^{3/2}\right)^n, \quad (4.1)$$

where n represents the dimension of the problem. For a typical three-dimensional DNS ($n = 3$), the total grid points will scale with $Re_\lambda^{9/2}$. This stiff scaling will impede the exploration of much higher Re_λ even with the most optimistic Moore's law projections. However, if we are able to reduce the dimensionality of the problem to one dimension ($n = 1$) through sensible modelling assumptions, we are able to show a much more optimistic scaling projection $\sim Re_\lambda^{3/2}$ to continue the exploration of extreme Reynolds number turbulence. Although the computational promise of one-dimensional surrogate models to study high-Reynolds number turbulence may be appealing, the necessary assumptions to simplify the problem may imbue the results with too many modelling approximations to be useful. Assessing the validity of a one-dimensional turbulence model, especially with respect to the dynamics at smallest scales, is the main motivation of the present work.

The formalism for solving the inherently three-dimensional problem of turbulence along a single spatial direction is attributed to Kerstein [78]. The ODT approach, which represents an adaptation of the original LEM by Kerstein [77], relies on the use of stochastic eddies to represent the effects of three-dimensional vortical overturns; the eddies emulate the mechanistic features of turbulent flows. Over the years, this model has been extended to solve a variety of freely decaying [154], wall bounded [20], and forced turbulence [40] cases. Despite relying on some modelling assumptions, ODT captures some of the main features of turbulence, such as reproducing the law of the wall—even capturing similar fea-

tures to the AEM [121]—or the energy spectrum in HIT [78, 150, 20] and represents the basis for the current study.

Adequate representation of rare events is central to the accurate modelling of the intermittent behaviour of turbulence at high Reynolds numbers. These events are characterised by short-lived, extreme fluctuations in dissipation and enstrophy, accompanied by intense local vorticity [188]. The probability distribution of the dissipation rate has been extensively studied at high Reynolds numbers, and has been approximated with log-normal distributions and stretched exponentials for dissipation tails [38, 187]. To establish the validity of the ODT model at these conditions, a thorough quantitative comparison of the ODT simulation results with established benchmarks is essential.

In this work, we compute HIT at up to $Re_\lambda \approx 5428$ using ODT , validate the results with theoretical predictions, compare with published results, and show the potential of this approach to further explore extreme Reynolds number turbulence. A fully compressible fluid model in a Eulerian frame-of-reference is developed in ODT , which departs from the classical Lagrangian approach favoured by most previous workers. We introduce a quasi-one dimensional representation of the governing equations by modelling the transverse derivatives based on the work of Marmanis *et al.* [106]. We investigate the turbulent energy spectra, skewness, and dissipation rate among other properties of turbulence. The obtained results show significant compressibility effects due to the deficiencies of the forcing method in the compressible framework, as will be discussed in section 4.3.1. Finally, we use the ODT framework to investigate flow features leading up to extreme dissipation events at a high Reynolds numbers.

4.2 Model formulation

4.2.1 Simplified governing equations

We use the temporally and spatially scale-resolving ODT approach for the computation of high Reynolds number, forced homogeneous isotropic turbulence (HIT). To account for

the inherently three-dimensional structures on the one-dimensional domain, a multiscale sequence of triplet mappings is stochastically applied, which mirrors the mechanistic behaviours of turbulent eddies in the flow. This approach differs from shell models, where each logarithmic shell represents a wave-number and carries spatial information indirectly. The high Reynolds number turbulence is sustained through a forcing term applied to the large scales in the flow. The conservation equations for mass, momentum, and energy, closed with the ideal gas state equation, are solved in a fully Eulerian framework along a periodic line domain. The present formulation uses the fully conservative form of the NS equations (ρ , ρu_i , and ρe) and we solve the forced HIT in the low-turbulent Mach number limit $M_t \ll 0.1$.

As the present compressible ODT formulation relies on the solution of the NS equation along a one-dimensional domain, the normal derivative terms must be modelled. These modelled terms are identified with a star in the below equations:

$$\begin{aligned}
\frac{\partial \rho}{\partial t} + \frac{\partial(\rho u_1)}{\partial x_1} + \left[\frac{\partial(\rho u_k)}{\partial x_k} \right]^* &= 0, \\
\frac{\partial(\rho u_1)}{\partial t} + \frac{\partial(\rho u_1 u_1)}{\partial x_1} + \left[\frac{\partial(\rho u_1 u_k)}{\partial x_k} \right]^* &= -\frac{\partial P}{\partial x_1} + \frac{\partial \sigma_{11}}{\partial x_1} + \left[\frac{\partial \sigma_{k1}}{\partial x_k} \right]^*, \\
\frac{\partial(\rho u_2)}{\partial t} + \frac{\partial(\rho u_2 u_1)}{\partial x_1} + \left[\frac{\partial(\rho u_2 u_k)}{\partial x_k} \right]^* &= -\left[\frac{\partial P}{\partial x_2} \right]^* + \frac{\partial \sigma_{12}}{\partial x_1} + \left[\frac{\partial \sigma_{2k}}{\partial x_k} \right]^*, \\
\frac{\partial(\rho u_3)}{\partial t} + \frac{\partial(\rho u_3 u_1)}{\partial x_1} + \left[\frac{\partial(\rho u_3 u_k)}{\partial x_k} \right]^* &= -\left[\frac{\partial P}{\partial x_3} \right]^* + \frac{\partial \sigma_{13}}{\partial x_1} + \left[\frac{\partial \sigma_{3k}}{\partial x_k} \right]^*, \\
\frac{\partial(\rho E)}{\partial t} + \frac{\partial(\rho u_1 E)}{\partial x_1} + \left[\frac{\partial(\rho u_k E)}{\partial x_k} \right]^* &= -\frac{\partial(P u_1)}{\partial x_1} + \left[\frac{\partial(P u_k)}{\partial x_k} \right]^* - \frac{\partial q_1}{\partial x_1} - \left[\frac{\partial q_k}{\partial x_k} \right]^* \\
&+ \frac{\partial(u_1 \sigma_{11} + u_2 \sigma_{12} + u_3 \sigma_{13})}{\partial x_1} + \left[\frac{\partial(u_1 \sigma_{k1} + u_2 \sigma_{k2} + u_3 \sigma_{k3})}{\partial x_k} \right]^*,
\end{aligned} \tag{4.2}$$

where $k = 2, 3$. The three spatial directions are identified by x_i ($i = 1, 2, 3$), while ρ, P, u_i, E represent respectively the density, pressure, velocity components, and total energy ($e + 0.5(u_1^2 + u_2^2 + u_3^2)$). The above equations are closed using the ideal gas equation of state.

Stress components are computed using simplified deviatoric stress components assuming

a Newtonian fluid:

$$\sigma_{ij} = \mu \left(\frac{\partial u_i}{\partial x_j} + \frac{\partial u_j}{\partial x_i} \right) + \lambda_s \delta_{ij} \frac{\partial u_l}{\partial x_l} \quad (4.3)$$

where $(i, j, l) = (1, 2, 3)$, μ is the dynamic viscosity, δ_{ij} is the Kronecker delta, and λ_s is the second viscosity coefficient. The heat flux, q_j , in the j -direction is modelled assuming Fourier's law. The three components of the heat flux are given by $j = 1, 2$ and 3 in:

$$q_j = -k_t \frac{\partial T}{\partial x_j}, \quad (4.4)$$

where, T is the temperature, k_t is the thermal conductivity and the normal derivatives are modelled as discussed below. We solve equation (4.2) for low-turbulent-Mach number HIT. This approach, although non-standard for incompressible three-dimensional DNS, allows an explicit formulation for pressure that stems from the ideal gas state equation. Furthermore, the time advancement is constrained by the extremely small, sub-Kolmogorov timescales on a fully adaptive mesh, thus making the acoustic Courant time constraint not as detrimental.

We model the forced HIT on a one-dimensional periodic domain of length 2π using a locally adaptive mesh that increases the resolution in regions of high gradients. The smallest eddy size is enforced by setting the minimum allowable cell size to one-third of the Kolmogorov length scale. A combination of the weighted essentially non-oscillatory (WENO) fifth-order scheme and the HLLC solver is used, as described in the work of Houim and Kuo [55]; the time integration is done using a third-order Runge-Kutta scheme. The computed flow velocity (u) and the isentropic speed of sound (c) are used to define the acoustically constrained minimal time step advancement. The present implementation is an extension to the open-source ODT code developed by Stephens and Lignell [169], which was based on a Lagrangian framework.

To correctly approximate the three-dimensional NS equation along a single-dimensional line, the ODT formulation must account for the effect of the velocity vector and its derivatives. Classical ODT formulations use a single velocity-component [78], often normal to the line domain to account for the dominant shear. In this work, we follow the subsequent development by Ashurst and Kerstein [6], which considers the complete velocity vector.

This formulation is necessary to correctly account for the energy redistribution that drives the flow to isotropy. As the governing equations in ODT are constrained to a single dimension, similar considerations must be placed on the derivatives of the velocity vector, temperature, and pressure. Classical ODT formulations, for both incompressible [140] and compressible [45] flows, usually only account for the component of the derivative along the line domain; this simplification is justified by aligning the domain along the direction of the steepest gradient of the flow. In HIT, the other components of the derivatives must be considered to avoid mathematical inconsistencies in the governing equations, such as a nonzero dilatational term ($\partial u_1/\partial x_1$) and inconsistencies in the acoustic energy transfer of energy (which promotes artificial anisotropy) by omitting the pressure derivative terms. Therefore, we introduce an approximation to account for additional terms of the velocity derivative tensor.

With the ODT domain aligned in an arbitrary x direction, the derivative terms along that direction can be calculated directly, while the other six terms of the velocity derivative tensor remain unknown ($\partial u_1/\partial x_2$, $\partial u_1/\partial x_3$, $\partial u_2/\partial x_2$, $\partial u_2/\partial x_3$, $\partial u_3/\partial x_2$, and $\partial u_3/\partial x_3$). Similarly, there are six important unknown second derivative terms necessary for the calculation of the viscous stress tensor. These unknown derivatives are the modelled terms in equation (4.2). In the absence of a closed-form representation of these derivatives, Marmanis *et al.* [106] proposed a two-parameter simplification to relate the known and unknown derivatives. In their general formulation, they related the transverse to the longitudinal derivatives such that $\alpha \partial u_i/\partial x_1 \equiv \partial u_i/\partial x_2$ and $\beta \partial u_i/\partial x_1 \equiv \partial u_i/\partial x_3$. A similar approximation was made to account for the principal unknown second-order derivative terms ($\alpha^2 \partial^2 u_i/\partial x_1^2 \equiv \partial^2 u_i/\partial x_2^2$ and $\beta^2 \partial^2 u_i/\partial x_1^2 \equiv \partial^2 u_i/\partial x_3^2$). In this form, the ratio α/β and α^2/β^2 represent the anisotropy of the unknown derivatives and dissipation, respectively. If α and β were computed from experiments or direct simulation, they would have a probability distribution that would vary in space and time. Similarly to the work by Marmanis *et al.* [106], we assume α and β to be constants along x , but we further assume $\alpha = \beta = 1$ given the inherent statistical isotropy of the flow under consideration, and the starred terms in the governing equations are thereby evaluated based on the derivatives along the ODT domain. The transverse derivatives of pressure and temperature are also evaluated based

on the longitudinal derivatives using the formulation described for velocity derivatives. Though the compressible formulation allows for the inclusion of transverse derivatives and pressure gradients, the discussion in section 4.3.1 later reveals that this occurs at the cost of strong compressible effects as an artifact of the adopted forcing methodology, with a major portion of injected energy for generating turbulence absorbed in domain heating.

4.2.2 Stochastic eddies to model turbulence

To account for the transport phenomena associated with the three-dimensional turbulence in the one-dimensional domain, stochastically generated turbulent eddies, represented as linear eddies, are superimposed; these ideas originate from the seminal work by Kerstein [78]. The interaction of the turbulent eddies with the line induces turbulent mixing at a specific physical location with a length and a time scale along the ODT line. These linear eddies, represented as a predefined mapping known as a triplet mapping (see equation (4.5)), introduce higher wave-numbers in the domain which are able to mirror the energy cascade. The mapping is measure-preserving for all the mapped variables and their moments, and does not introduce jump discontinuities. In the present compressible formulation, the mapping is applied to all flow variables and can be mathematically represented as:

$$f(x) = x_o + \begin{cases} 3(x - x_o), & x_o \leq x \leq x_o + \frac{1}{3}l \\ 2l - 3(x - x_o), & x_o + \frac{1}{3}l \leq x \leq x_o + \frac{2}{3}l \\ 3(x - x_o) - 2l, & x_o + \frac{2}{3}l \leq x \leq x_o + l \\ x - x_o. & \text{otherwise} \end{cases} \quad (4.5)$$

The starting location of the eddy x_o and the eddy size l are randomly sampled from a joint probability distribution function. Three copies of the profile of the eddy region are made, compressed, and stitched together while inverting the middle segment as shown in figure 4.1. A kernel function $K(x) = f(x) - x$ is defined to represent the displacement induced by the eddy and integrates to zero over the eddy region. Subsequent to the triplet map, $f(x)$, the energy is redistributed among the velocity components using a

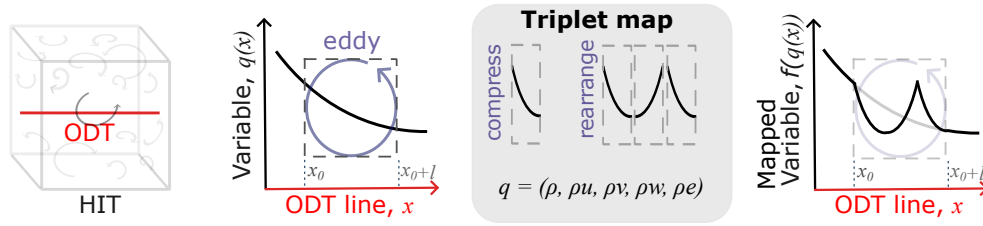


Figure 4.1: Triplet-map applied to the variable $q(x)$.

transformation involving the kernel K to simulate the tendency towards isotropy [6]. The post-triplet-map velocity transformation is carried out based on a measure of available energy in the velocity components. While this energy transfer among the velocity components conserves net energy, the momentum conservation in each coordinate is non-trivial for non-uniform density, and an additional term is added to the post-triplet-map velocity transformation to conserve momentum. The algorithms for velocity transformation and energy balance pertaining to the eddy events were further elaborated in chapter 3.

The eddies modify the underlying flow variables on the one-dimensional domain, and are invoked stochastically in time. Each eddy event is considered to be an instantaneous occurrence; however, the total number of admitted eddies is controlled. The admittance of eddies is restricted by defining an eddy acceptance probability, p_e , which is a function of the eddy time scale. The eddy time scale, τ , depends on the instantaneous state of the system over the region impacted by the eddy, and changes as the system evolves. The eddy time scale is given by the instantaneous state of the system as described in Sect. 3.1.4. Continual re-evaluation of the time scale of each possible eddy leads to a high computational cost and an indirect method is used instead. First, a sequence of eddies is sampled using *guessed* probability distributions, $g_1(x_o)$ and $g_2(l)$, for eddy start locations and sizes, respectively. Secondly, the sampled eddy is subject to acceptance or rejection based on the probability:

$$p_e = \frac{C \Delta t_e}{l^2 g_1(x_o) g_2(l) \tau}, \quad (4.6)$$

The parameter C is used to scale the turbulence intensity. Δt_e is the mean time interval between sampling of eddies, chosen so that p_e is typically much smaller than unity. The

two-step procedure produces the physically prescribed ensemble of eddies.

A uniform distribution $g_1(x_o)$ for the eddy start location is assumed, along with a probability distribution for the eddy size given as:

$$g_2(l) = \frac{c_1}{l^{s+1}} \exp\left(-\frac{c_2}{l^s}\right). \quad (4.7)$$

The parameters c_1 and c_2 are assigned so as to roughly approximate the anticipated flow-specific size distribution of eddies. The smallest eddy size permitted in the ODT formulation is three times the minimum cell size. In the basic ODT implementation in Stephens and Lignell [169], the exponent s is chosen as unity. The obtained results are found to have negligible dependence on the guessed eddy-size distribution for eddy sampling.

4.2.3 Generating sustained turbulence

In order to sustain statistically steady, homogeneous, isotropic turbulence, an external forcing must be applied to counteract the viscous dissipation. The forcing methodology in ODT differs from the methods used in DNS. Forcing is carried out via source terms in the DNS transport equations to attain specific levels of steady-state TKE. The production rate is then computed a posteriori from the simulation data or directly inferred from the observed dissipation rate. In contrast, in the current model, forcing is carried out via events of integral-scale size whose rate of occurrence determines the integral time scale. Unlike eddy events, they serve solely to inject specified kinetic-energy increments via the kernel operation, as follows.

The energy injected into the domain by forcing at the integral length and time scales cascades to smaller scales due to the stochastic eddies of ODT. The rate of production of turbulent kinetic energy, \mathcal{P} , by this energy injection mechanism is a prescribed input. Following *Fistler et al.* [40], a forcing methodology is used that produces turbulence by a sequence of forcing events, each of which adds a known amount of kinetic energy to the velocity components. Turbulent kinetic energy (Δk) is added at the integral-time scale of targeted turbulence (T_{11}), and is given by the product of the forcing time

scale (T_{11}) with the production rate (\mathcal{P}), density (ρ) and the forced volume ($A_c L_f$), such that: $\Delta k = \rho \mathcal{P} T_{11} A_c L_f$, where A_c and L_f are the notional cross-section area and forcing length, respectively. The cross-section area is defined temporarily to ensure dimensional consistency, but cancels out in the final equation used to impart TKE, thus having no consequence.

In a manner similar to the velocity transformation in an ODT eddy, the forcing events, $u_i \rightarrow u_i + d_i K(x)$, modify the velocity components, but without the triplet map ($f(x)$). Introducing an elemental volume $dV = A_c dx$, the net imparted kinetic energy is related to the coefficient d_i by:

$$\frac{1}{3} \Delta k = \frac{1}{2} \int_{x_o}^{x_o+L_f} \rho ((u_i + d_i K(x))^2 - u_i^2) A_c dx. \quad (4.8)$$

Using the definition of added Δk , the coefficients d_i are computed as:

$$d_i = \frac{1}{I} \left(-J_i \pm \sqrt{J_i^2 + 2I \Delta k / (3A_c)} \right) = \frac{1}{I} \left(-J_i \pm \sqrt{J_i^2 + \frac{2}{3} \rho I \mathcal{P} T_{11} L_f} \right), \quad (4.9)$$

where $I = \int_{x_o}^{x_o+L_f} \rho K(x)^2 dx$, $J_i = \int_{x_o}^{x_o+L_f} \rho u_i K(x) dx$ and T_{11} is the integral time scale. The simulations are conducted for a total duration that is sufficient to sample enough of the forcing events and attain stable turbulence characteristics over multiple eddy turn-over times.

4.3 Results

4.3.1 Details of simulations

To generate turbulence at different Re_λ , we modify the smallest scales (by modifying the viscosity). The integral time as well as length scale is held fixed.

Except where noted, we fix the forcing length scale (L_f) to be slightly lower than the domain length (L). This was done to avoid any inconsistencies due to the domain periodicity. The forcing length scale L_f and integral time scale T_{11} provide the characteristic

length and time scales in this study, which are used to normalize all the quantities, as discussed below.

First, we define an integral scale Reynolds number for forced isotropic turbulence as $Re = U_f L_f / \nu$, where $U_f = L_f / T_{11}$ is the velocity scale for the forced turbulence. The integral-scale Reynolds number is set by controlling the kinematic viscosity ν via $Re = (L_f / T_{11}) L_f / \nu$, which scales as $1/\nu$. The Kolmogorov length scale η normalized by L_f scales as $Re^{-3/4}$ [136]. The minimum grid cell size used with the adaptive meshing is set to be one-third the size of the Kolmogorov length scale. Since the smallest permitted eddy size is three times the minimum cell size, resolution down to the Kolmogorov length scale is ensured.

Secondly, the production rate, \mathcal{P} , which scales as L_f^2 / T_{11}^3 , is the input parameter that imparts the energy via the forcing to the flow to sustain the turbulence. We recall that $\Delta k = \rho \mathcal{P} T_{11} A_c L_f$ (from section 4.2.3), where $\Delta k / \rho$ can be understood as the velocity variance increment $\langle \Delta u^2 \rangle \sim \mathcal{P} T_{11}$ applied to the volume $L_f A_c$. Thus, the velocity variance can be used to define the scaling $u' \sim \sqrt{\mathcal{P} T_{11}}$. The production rate normalized by its scaling L_f^2 / T_{11}^3 is of the order unity for all the simulated cases, which sets the normalized u' to be of order unity.

The kinematic viscosity (ν) and production rate (\mathcal{P}) together set the Re_λ of the generated turbulence. For all the simulated cases, we held the normalized production rate fixed at $\mathcal{P} = 0.36$ and varied ν for setting Re_λ .

The current model solves the compressible form of the Navier-Stokes equation, thus the viscous dissipation results in a slight increase of domain mean temperature with time. The dissipation rate is about 10 times smaller than the prescribed value of \mathcal{P} due to the domain heating as the simulation proceeds. The transport of energy from the integral to smallest scales is later demonstrated by the constant energy flux over a broad range of scales, matching the mean dissipation rate, shown in figure 4.5.

The major portion of the injected energy by the turbulence forcing is being absorbed into the heating of the domain, which is an outcome of the developed compressible formulation. Petersen and Livescu [132] shows the necessity of splitting the forcing terms into

solenoidal and dilatational terms in compressible turbulence, and controlling the forcing method ensures that the major portion of the injected energy is input into the solenoidal component of velocity, which is divergence-free, and hence incompressible. The energy injection into the dilatational component of velocities provides a pathway for the injected energy to convert to pressure work, thus acting as an energy sink in the momentum equation. Contrary to the precise control of the forcing in Petersen and Livescu [132], the adopted forcing methodology does not distinguish between the solenoidal and dilatational terms, and a large fraction of the injected energy is absorbed in the dilatational pressure work as the dilatational contribution emerges from a nonzero $\partial\rho u_1/\partial x_1$ term. In addition, the one-dimensional compressible framework is prone to artificial changes in density, thereby injecting energy into the pressure-work. Since the three velocity-derivative components are set equal, any change in one of the velocity-derivative components is not counteracted upon by the other components, thus leading to an unavoidable change in density via the continuity equation. Thus, the obtained results show significant compressible effects, leading to a disproportionate injection of input energy into the pressure work. Section 4.4 provides more details on the compressibility effects.

Several forced HIT simulations were conducted spanning a wide range of Re_λ , which is computed using $Re_\lambda = 2k\sqrt{1/(3\langle\epsilon\rangle\nu)}$, where the mean dissipation rate is computed in ODT using Kerstein [78]:

$$\langle\epsilon\rangle = 3\nu\left\langle\left(\frac{\partial u_1}{\partial x}\right)^2\right\rangle. \quad (4.10)$$

Table 4.1 summarises the physical details of the reported cases. The kinematic viscosity ν , integral length scale L_ϵ , Kolmogorov scale, root-mean-square velocity fluctuation magnitude u' and dissipation rate $\langle\epsilon\rangle$ have been normalized based on the inputs L_f and T_{11} . The quantity $D^* = \langle\epsilon\rangle L_\epsilon/u'^3$, which uses an output based normalization for dissipation rate, and the velocity-derivative skewness $S = \overline{(\partial u_1/\partial x)^3}/\overline{(\partial u_1/\partial x)^2}^{3/2}$, are also tabulated. All cases are run until they reach a statistically steady state after which the data is collected over a sufficiently long time window. For the highest Re_λ case, the integral statistics are well converged but the higher-order and small-scale statistics are not fully smooth due to the very long simulation time required (over two months of continuous calculations). We

Re_λ	$\nu \cdot 10^{-6}(L_f^2/T_{11})$	$L_\epsilon(L_f)$	$\eta \cdot 10^{-5}(L_f)$	$u'(L_f/T_{11})$	$\langle \epsilon \rangle (L_f^2/T_{11}^3)$	D^*	S
218	27.2	0.352	87.8	0.347	0.0338	0.566	-0.48
355	11.2	0.349	43.6	0.367	0.0386	0.489	-0.25
491	6.92	0.339	29.8	0.389	0.0413	0.404	-0.35
929	2.40	0.341	13.7	0.405	0.0390	0.385	-0.31
1361	1.20	0.327	8.26	0.407	0.0370	0.322	-0.67
1745	0.84	0.332	5.94	0.448	0.0473	0.297	-0.27
5428	0.20	0.385	1.86	0.605	0.0682	0.188	-0.48

Table 4.1: List of cases of HIT in the present study. D^* is evaluated using the energy spectrum with the inertial range extrapolated below $k = 6$. The terms in the parentheses are normalizing factors used for the respective quantities.

first validate for HIT with ODT and then investigate the emergence of extreme dissipation events at the smallest scale of turbulence.

4.3.2 Validation and theoretical considerations

The turbulent kinetic energy (TKE) spectrum of HIT admits a number of theoretically derived scaling laws that can be used to validate the present ODT simulations. To validate the results, the TKE spectrum for the case at $Re_\lambda = 929$ is compared with the theoretical result:

$$E(k) \approx K_o \langle \epsilon \rangle^{2/3} k^{-5/3} \quad (4.11)$$

from Kolmogorov [87], where the Kolmogorov constant is given by $K_o \approx 1.62$ [163]. The energy spectrum $E(k)$ is computed by using the one-dimensional Fourier transform of the velocity component u'^2 in the spatial domain and then multiplying a factor of 55/18 corresponding to the Sreenivisan constant [163] which relates the one-dimensional spectrum to the three-dimensional spectrum.

The turbulent kinetic energy spectrum obtained displays an offset from the theoretical solution for $E(k)$ at the largest scales, despite an otherwise consistent inertial-range

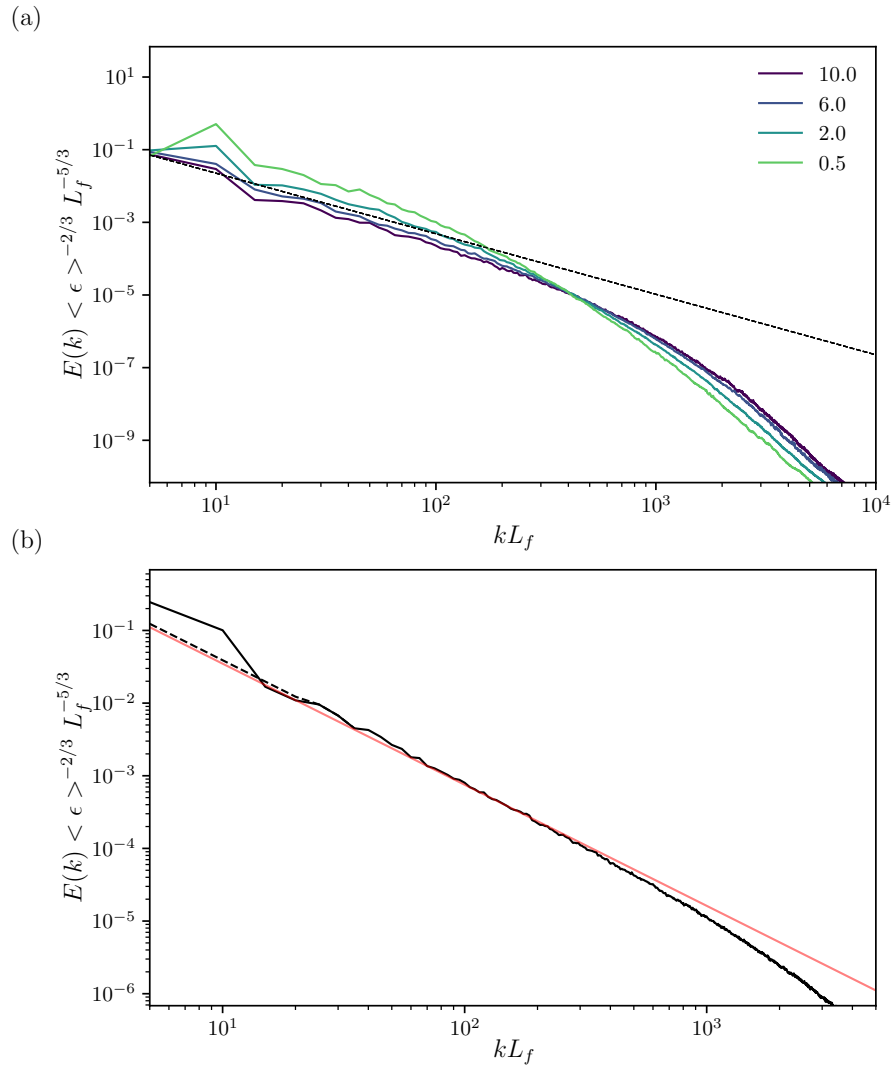


Figure 4.2: (a) Convergence of TKE spectrum with C parameter, and (b) TKE spectrum at $Re_\lambda = 929$ with $C = 10$: —, from ODT, - -, extrapolated and —, theoretical scaling (see equation 4.11).

spectrum with the slope of $-5/3$, see figure 4.2. The anomaly observed at the largest scales can be attributed to the interplay between forcing length scales L_f and the overall domain size L . As noted in Fistler *et al.* [40], lowering the forcing length scale relative to the domain size can mitigate the observed low-wave-number anomaly. Testing a case with $L_f \ll L$, we observe the TKE scaling as $\sim k$ for k less than the forcing wave-number k_f , see figure 4.3. In the simulated cases of turbulence in Table 4.1, $L_f \approx L$, and the observed large-scale anomaly likely stems from a spectral barrier that limits energy transfer to wave-numbers below what the domain can accommodate, causing accumulation of TKE at low wave-numbers ($k < k_f$). In cases where L is larger than L_f , the TKE spectrum exhibits k^4 scaling at scales larger than L_f for physical turbulence, while in the ODT model (see figure 4.3), the spectrum scales as k for $k < k_f$, as suggested by findings from LEM analysis in Kerstein and McMurtry [81]. The used compensation for correcting the observed anomaly at the largest scales can introduce arbitrary errors in computation of dissipation rate and integral length scale, which involves integrals with $1/k$, where k values approaching zero may lead to divergence of the integral. The dissipation region exhibits a scaling of k^{-5} in figure 4.3, consistent with the findings in Refs. [78] and [120].

To address this offset, the spectra at these largest scales ($k \leq 6$) are replaced with the extrapolated inertial-range spectra. The dissipation, computed from the velocity derivatives with equation (4.10), is found to agree with the indirect computation via the energy spectrum: $\langle \epsilon \rangle = \int_0^\infty 2\nu k^2 E(k) dk$. It shall be noted that the computation of dissipation rate using the energy spectrum is merely used to check the consistency of the results from equation (4.10).

As the present ODT formulation includes all three velocity components, we verified that the root-mean-square of all three components are equal ($u'_1 = u'_2 = u'_3$), validating the isotropy condition of the present model despite the one-dimensional formulation. It is noted that despite the attempts to enforce isotropy in the system, the solution of the equation along the x -coordinate with distinguished role of u_1 and modelling in transverse directions, introduce an inherent anisotropy. Nonetheless, the main features of isotropic turbulence are still evident in the results. The velocity derivative skewness, S , computed from the generated turbulence, shown in Table 4.1, is close to the expected value of -0.53

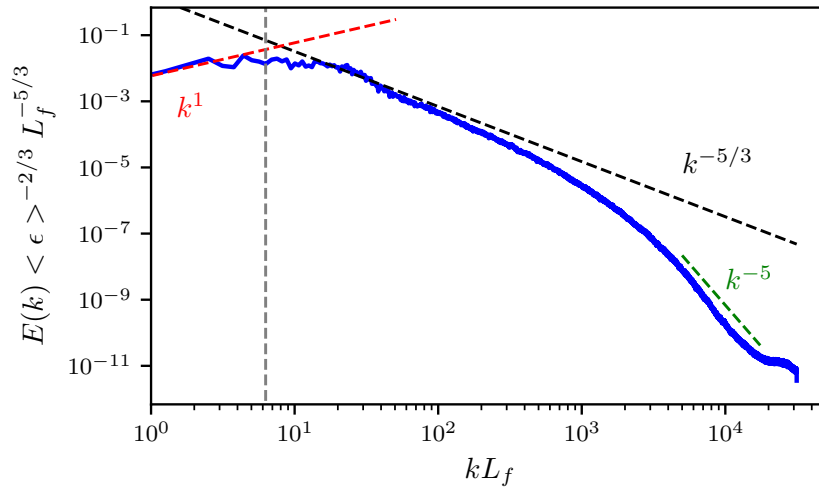


Figure 4.3: TKE spectrum with a case with domain size much larger than the forcing length scale at $Re_\lambda = 82$. The energy scaling of different regions, namely, at the region of length scales larger than the forcing length scales (shown by the vertical dashed line at $kL_f = 2\pi$), the inertial and dissipation range are depicted.

from Antonia *et al.* [5], though with a larger variability in the present work compared with the findings in Antonia *et al.* [5]. The observed variability can be attributed to the finite sample size over a single dimension in ODT, in contrast with the three-dimensional DNS database, and can be possibly reduced by extending the simulation runtimes.

The ODT approach relies on a small number of user-defined parameters, and the sensitivity of these parameters should be understood. The turbulence intensity parameter, C , defined in equation (4.6), is a constant that is inversely proportional to the characteristic time scale of an eddy. In turn, this parameter influences the eddy acceptance probability, p_e . A study of the turbulent energy spectrum with regard to the turbulence intensity parameter C is carried out to verify the convergence of the results, see figure 4.2. As the parameter C is progressively increased up to approximately 6.0, the results converge to the theoretical prediction from equation (4.11).

Above this value, the spectra perfectly collapse with the theoretical prediction and exhibit insensitivity to C . Therefore, a value beyond this threshold is set to $C = 10.0$ in all the simulated cases. The convergence with respect to C is explained by the reduction of eddy-sampling time by ODT to counterbalance the increase in C when too many eddies are being accepted, thus, keeping an upper bound on eddy acceptance.

4.3.3 Reynolds number effects

The turbulence spectra, for Taylor Reynolds numbers increasing from 218 to 5428, are shown in figure 4.4(a). Taking into account the theoretical predictions for inertial-range scaling of TKE spectrum [87], the energy spectra of the generated turbulence follows the $-5/3$ slope when plotted in logarithmic scale against the wave-number. As expected, the smallest scales show an increase in energy content at higher Re_λ . However, the spectra overlap for all simulated cases in the inertial range and at large scales, which is consistent with the constant numerical domain size for all Re_λ . The consistency of the energy flux spectra $\Pi(k)$ in the inertial range is also consistent with DNS results from Ishihara *et al.* [62], see figure 4.5. The normalized energy flux spectra ($\Pi(k)/\langle\epsilon\rangle$) is unity at the inertial range signifying that the energy transfer across the scales equals the mean dissipation rate.

The start of the dissipation range is observed at the scales well above the Kolmogorov-length scale (η) in figure 4.5, thus, justifying the adequacy of the resolution.

The TKE spectra for different Re_λ exhibit an overlap when plotted with an η -normalized coordinate, see figure 4.6, exhibiting the $k^{-5/3}$ scaling in the inertial range.

The validity of the ODT-generated HIT is affirmed by computing the dissipation characteristics at increasingly small viscosities that correspond to high Re_λ . At these conditions, the mean dissipation rate, $\langle \epsilon \rangle$, asymptotically approaches a finite value as per the turbulence theories [87]. The normalized mean dissipation rate, D , best represents this asymptotic behaviour. We denote the mean dissipation rate computed from the extrapolated spectra as D^* . The integral length scale L_ϵ used to compute the normalized mean dissipation rate is defined using the TKE spectrum in wave-number space [29]:

$$L_\epsilon = \frac{\pi}{2u'^2} \int_0^\infty \frac{E(k)}{k} dk. \quad (4.12)$$

The computed normalized dissipation rate D^* is about 0.4 (both for the direct and extrapolated TKE spectra), which is consistent with the predictions from Donzis *et al.* [29] and the observations from other works; see figure 4.4(b). Interestingly, as the ODT approach enabled a computation at extreme Reynolds numbers, not currently achievable by conventional DNS, we observe a continued monotonic decrease with increasing Re_λ . However, since we are modelling turbulence outside of the currently accessible Re_λ range, a firm claim on the continued monotonic decrease of the normalized dissipation rate D^* will have to wait until further numerical and experimental results become available to confirm the trend.

4.3.4 Extreme dissipation events

The extreme instantaneous fluctuations occurring at the smallest scales of turbulence cause significant oscillations in local dissipation rate at high Re_λ . The prevalence of these extreme dissipative events at these extreme Reynolds numbers is evident from the extended tails in the probability distribution of the velocity derivatives and dissipation rate in figure 4.7.

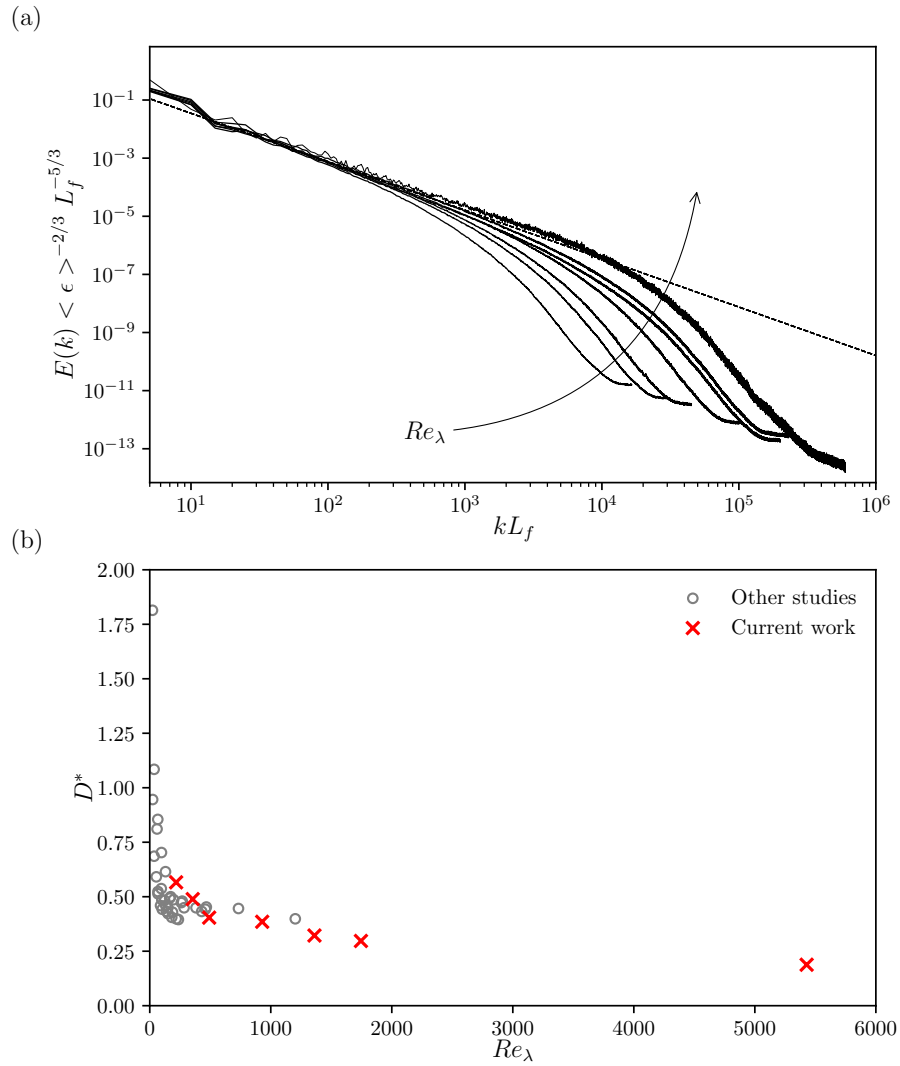


Figure 4.4: (a) Normalized energy spectrum at $Re_\lambda = 218, 355, 491, 929, 1361, 1745$ and 5428 (Re_λ increasing in the direction of the arrow), and (b) normalized dissipation rate D^* (comparative results from Ref.[62]).

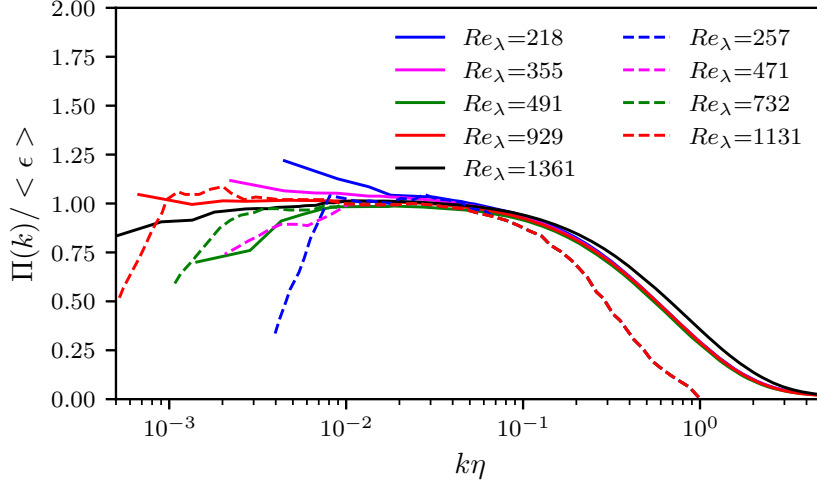


Figure 4.5: Energy-flux spectrum normalized with the mean dissipation rate. Solid lines depict ODT results and the dashed lines represent DNS results from Ref. [62].

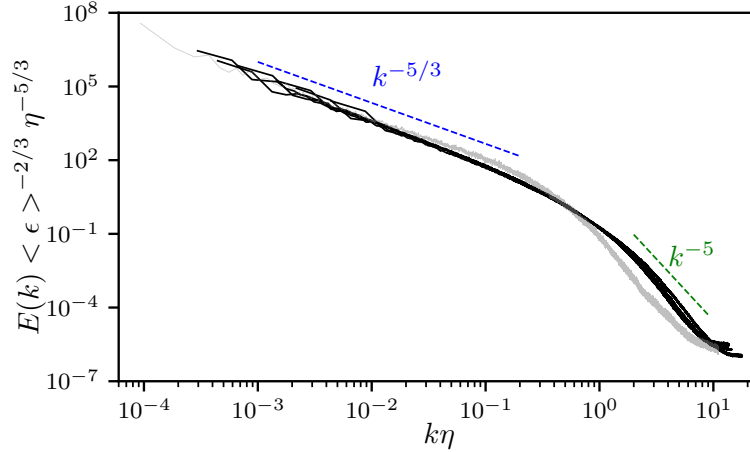


Figure 4.6: Overlapping TKE spectra with an η -normalized coordinate. The green dashed line shows k^{-5} scaling. $Re_\lambda = 5428$ has been shown in grey as it shows slight difference in characteristics from the remaining curves, which may be attributed to the insufficient run-time of the simulation.

These extreme events are of vital importance to represent the intermittency in turbulence. Insufficient total simulation time for the largest Re_λ of 1745 and 5428 precluded a formal analysis of small-scale statistics of the extreme events, although we note that the noisy distributions are consistent with the anticipated results.

The statistical approach of invoking turbulent eddies in ODT systematically accounts for the extreme events. The present model directly embodies the collocation of severe turbulent vorticity and dissipation rate [188], by virtue of an exceptional eddy at the smallest scales creating the specified extreme gradients and hence the extreme dissipation events. The statistical representation is an outcome of the ad hoc ODT eddy event modelling. To ascertain the validity of the rare event statistics produced by ODT, we compare the PDFs of dissipation rate with the results by Buaria and Sreenivasan [14], see figure 4.8. ODT produces the characteristic dissipation rate PDF shape, however, at elevated probabilities of occurrence of extreme events. In other words, ODT shows a more uniform probability distribution of dissipation events strength compared to the DNS but the functional form of the distribution and the Reynolds number effects are well captured (see figure 4.8, right).

We estimate the stretched exponential functions to approximate the dissipation rate PDFs for the two cases: $Re_\lambda = 491$ and 1361, see figure 4.9. The coefficients computed corresponding to the exponential function of the form $f(\epsilon/\langle\epsilon\rangle) \approx \exp(-b(\epsilon/\langle\epsilon\rangle)^{\gamma_s})$ are: (i) $b = 5.0$ and $\gamma_s = 0.139$ for $Re_\lambda = 491$, and (ii) $b = 5.3$ and $\gamma_s = 0.127$ for $Re_\lambda = 1361$. For comparison, the exponential functions reported in Yeung *et al.* [187] are (i) $b = 6.76$ and $\gamma_s = 0.25$ for $Re_\lambda = 390$, and (ii) $b = 6.25$ and $\gamma_s = 0.225$ for $Re_\lambda = 650$. ODT results lead to lower pre-multipliers (b) and exponents (γ_s) in comparison to DNS, consistent with the wider dissipation tails observed in ODT.

To further investigate the elevated occurrence of small-scale dynamics in the current model, we compute the longitudinal second-order structure functions $\langle(\delta u_r^L)^2\rangle$. The normalized PDF of δu^L in figure 4.10(a) exhibits the increased spread at dissipative scales ($n = 0, 1, 2$) in lines with the DNS results shown in figure 4.10(b). However, a larger probability of rare event occurrence and an approximate symmetry of the PDFs about $\delta u^L = 0$ is observed, unlike the DNS results, which exhibit clear skewness in the PDFs. Normalized

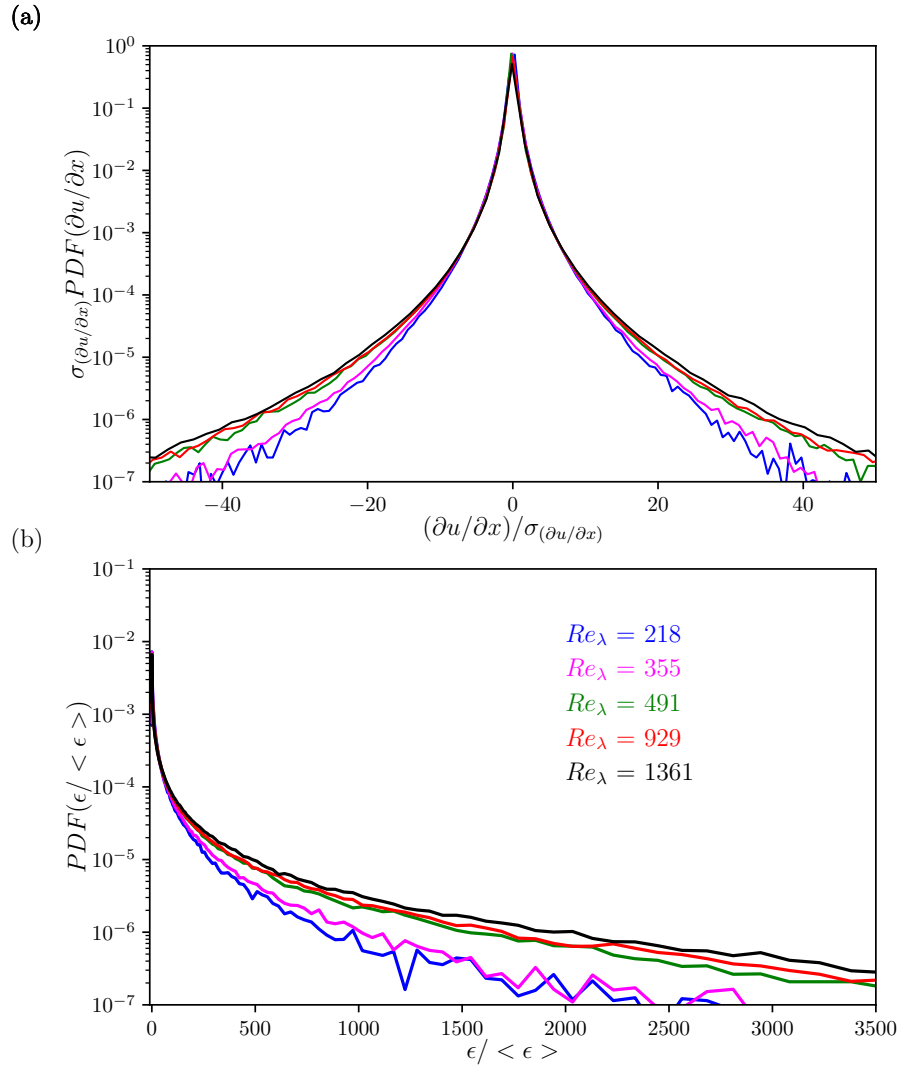


Figure 4.7: PDF of (a) the velocity derivative and (b) dissipation rate.

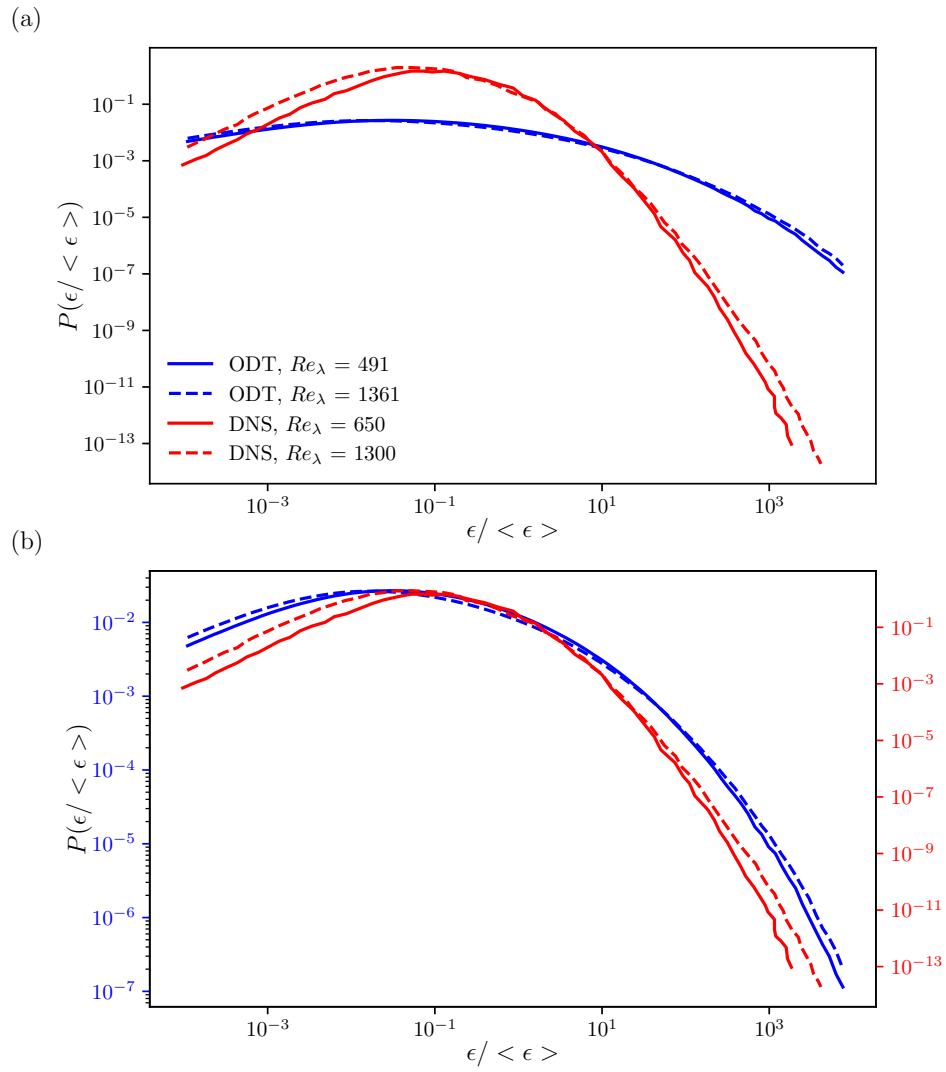


Figure 4.8: PDF of the dissipation rate in log-log plots. The vertical axis colors correspond to the respective plotted cases in (b).

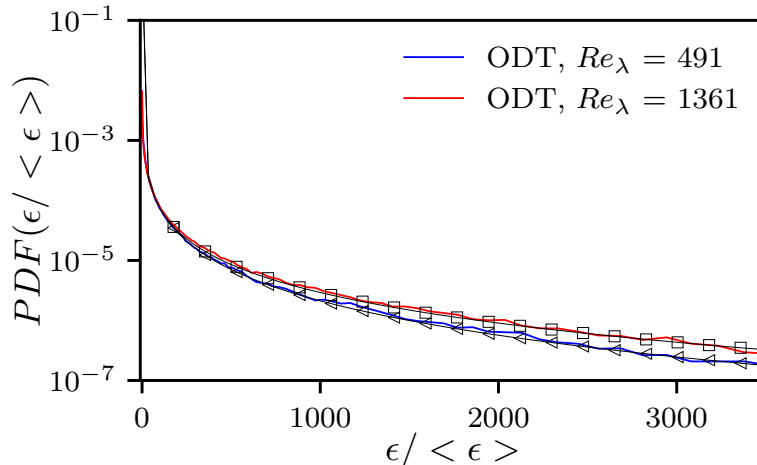


Figure 4.9: Stretched-exponential functions for dissipation rate PDF. Symbols show the stretched-exponential approximations to the PDFs.

structure functions are also compared with DNS results at different Re_λ in figure 4.11. The structure functions show an overlap at length scales in the vicinity of the Kolmogorov length scale, with an increased spread at the large separation distances.

To characterize intermittency in the generated turbulence, we find the high-order longitudinal structure functions and their scaling exponents, see figure 4.12. The p^{th} -order structure function is given by: $S_p^L = \langle (\delta u_r^L)^p \rangle \propto r^{\zeta_p^L}$, where ζ_p^L is the scaling exponent. To estimate the scaling exponent of the structure function, we look for the plateau of the local scaling exponent given by $\zeta_p^L(r) = d(\log(S_p^L))/d(\log(r))$, following the approach by Ishihara *et al.* [62]. The scaling exponents show a clear plateau for $p = 1$ to $p = 4$, and an irregular pattern at higher orders. The structure function exponents (ζ_p) derived from ODT exhibit the concavity property that distinguish the produced turbulence from the intermittency-free self-similar results from Kolmogorov [87]. The variation of ζ_p with the moment order p in figure 4.13 differs from Iyer *et al.* [69] in terms of the absolute values of the scaling exponents. However, the ODT results cross the intermittency-free line ($\zeta_p = p/3$) at about $p = 3$. Simulations of higher Re_λ turbulence, spanning over a long

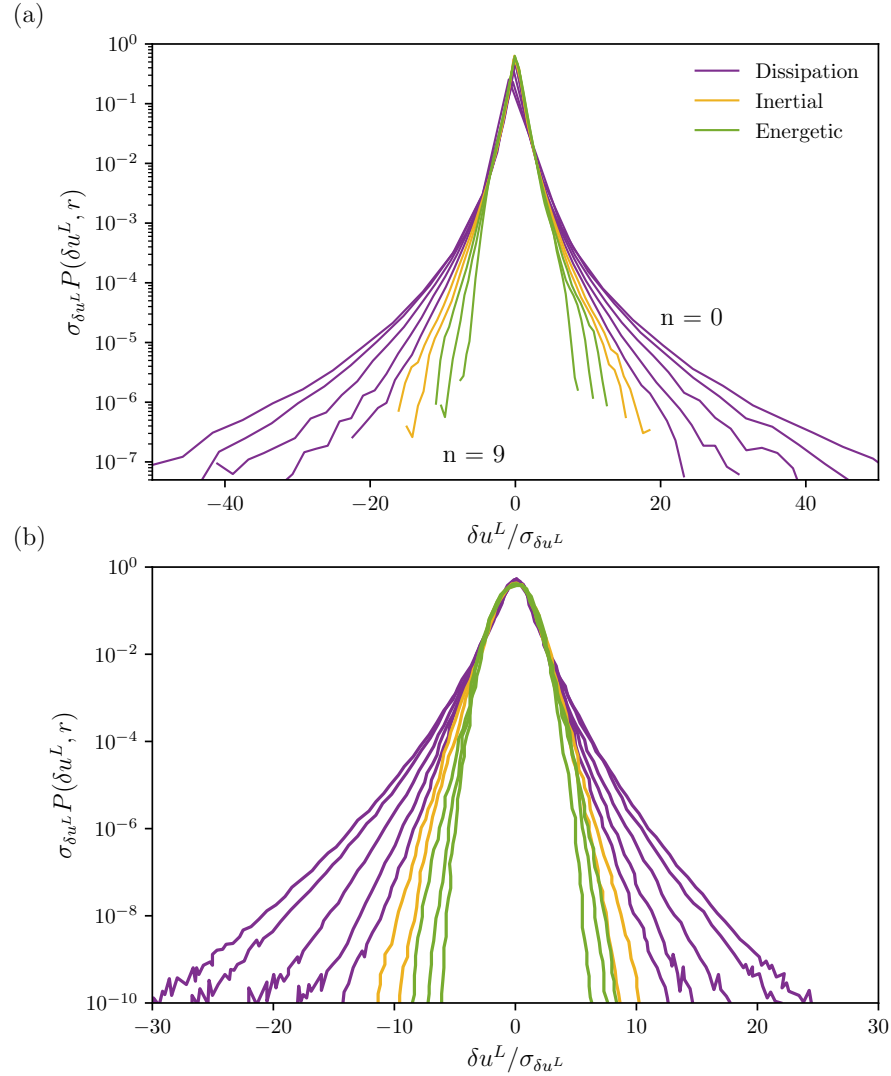


Figure 4.10: Normalized probability distribution functions of δu^L for (a) ODT at $Re_\lambda = 491$ and (b) DNS at $Re_\lambda = 460$ at fixed values of separation distance computed as $2^n \Delta x$, where n varies from 0 (\sim Kolmogorov scales) to 9 (\sim energy containing large scales) and Δx is the cell size (comparative results from Ishihara *et al.* [62]).

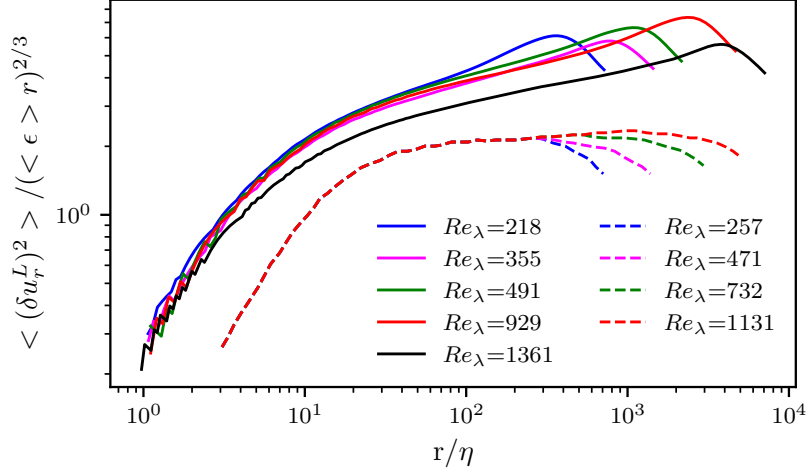


Figure 4.11: Normalized second-order longitudinal structure functions versus normalized separation distance. Solid lines depict ODT results and the dashed lines represent DNS results from Ishihara *et al.*[62].

duration of multiple T_{11} , might be essential to resolve the scaling exponents for larger p values.

It is noted that the features of the stretched exponential PDF tails in figure 4.12 along with the concavity in the variation of scaling exponents in figure 4.13 signifies deviations from the intermittency-free condition, but the characterizations are far from complete and are only an attempt by the authors to extract intermittency-like features from the ODT results.

ODT is a low-dimensional model that accounts for the turbulence through the superposition of stochastic eddy events. Although we are solving the governing equations along a single dimension, the qualitative and quantitative evaluation of the model tells us that many of the key features of dynamics of the full-dimensional equations are well captured, even at the smallest scales. Given the one-dimensional nature of ODT, extreme dissipation events can be traced back in time to identify the intense, repetitive shear experienced by the fluid. Despite the non-deterministic nature of ODT, we contend that the under-

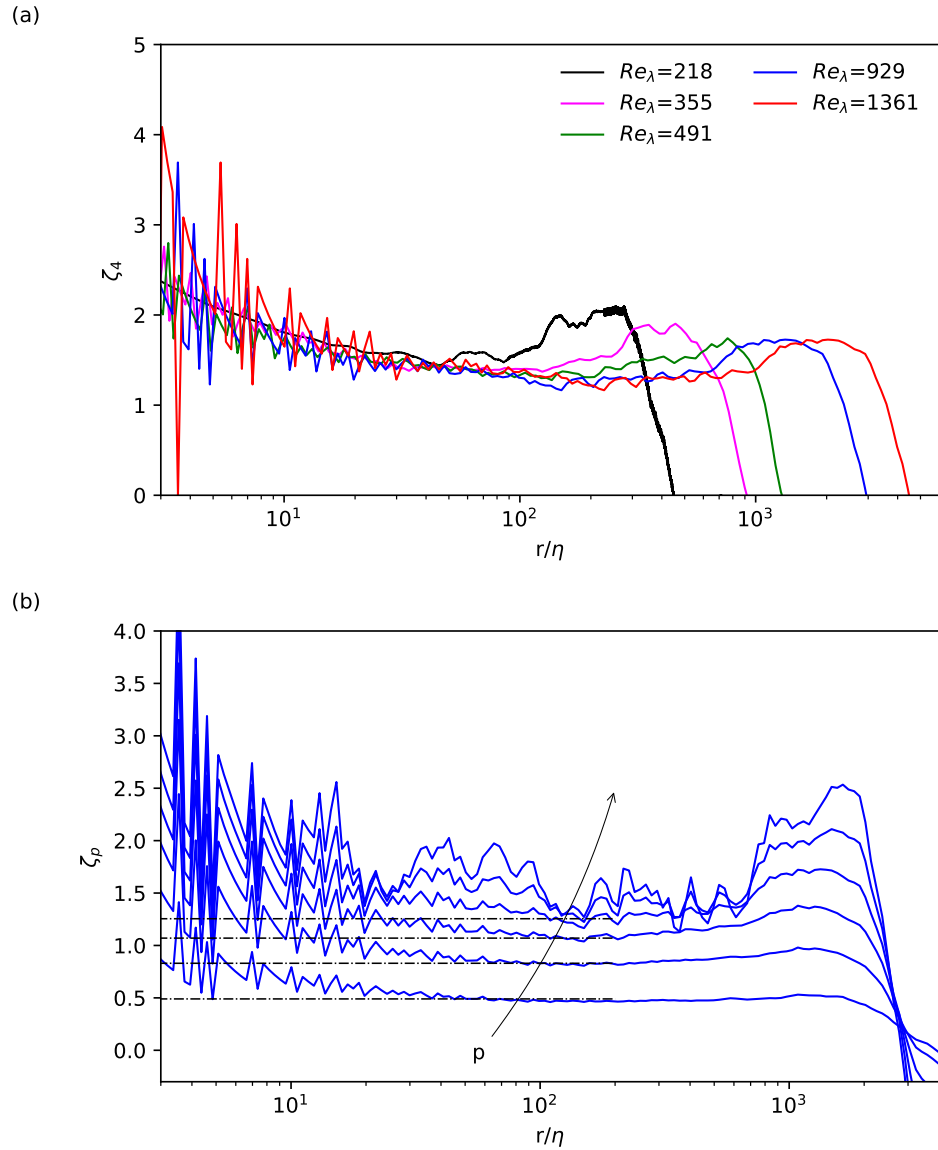


Figure 4.12: Higher-order structure functions and their exponents. (a) The extension of the plateau region for the exponent ζ_4 with increase in Re_λ , and (b) increase in ζ_p as p increases from 1 to 6 (along the direction of the arrow) for $Re_\lambda = 929$. The horizontal lines in (b) correspond to the ζ_p values of 0.49 ($p = 1$), 0.83 ($p = 2$), 1.07 ($p = 3$), 1.26 ($p = 4$) and 1.4 ($p = 5$).

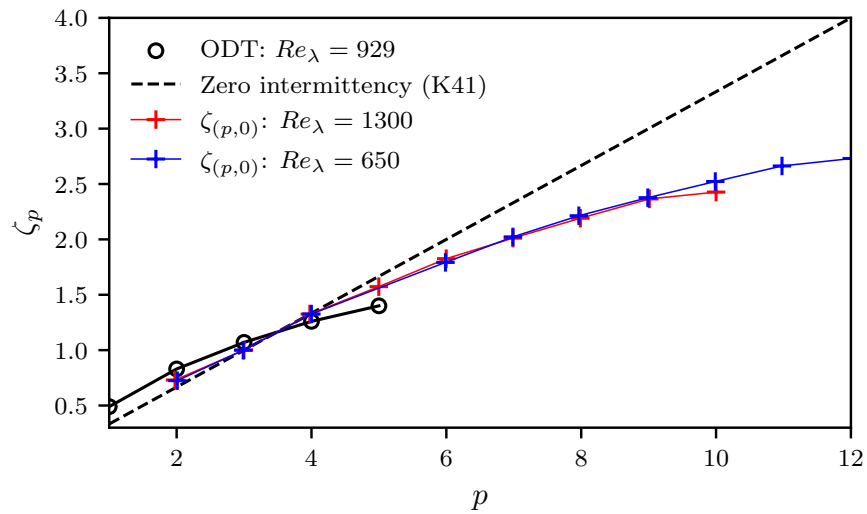


Figure 4.13: Intermittency in the structure-function exponents of ODT, compared with DNS results from Iyer *et al.* [69]. $\zeta_{(p,0)}$ denote the scaling exponents for longitudinal structure functions.

standing of the sequential superposition of eddy events that are a precursor of extreme small scale events can be informed by detailed exploration of the turbulence. Sharp local velocity gradients encourage the generation of smallest-scale eddies by amplification of E_{kin} (see equation (4.6)), causing large $1/\tau_{eddy}$, and hence a high acceptance probability p_e . These newly invoked eddies, at the smallest scales, further amplify the local dissipation rate. figure 4.14 illustrates two extreme dissipation events observed at times t_e^1 and t_e^2 , which immediately follow the occurrence of eddies in regions of high velocity gradients. By conditionally sampling all extreme events, we find that the local dissipation rate positively correlates with high $1/\tau_{eddy}$ and the number of eddies in the spatiotemporal region of the extreme event, see figure 4.15(a). The analysis to find the correlations was carried out for all the data points in the domain of length 2π from $t = 10 T_{11}$ to $t = 13.33 T_{11}$ for $Re_\lambda = 929$. The time between $t = 10 T_{11}$ and $t = 13.33 T_{11}$ was divided into 200 bins and the domain length was divided into 60 bins to gather the correlation data. Many localised eddies, at least one of which is highly energetic, is hence, a favourable condition for the occurrence of an extreme event.

4.4 Compressibility effects

In this section, a more detailed explanation of the modelling assumptions used in the solution of the compressible flow equations, mentioned in section 4.2, are presented for completeness. Although we solve the compressible NS equations, the simulations are conducted at very low Mach number. The shear stress, σ_{ij} , in equation (4.3) depends on the dynamic viscosity, μ , and the second coefficient of viscosity, λ_s . The variation in μ with temperature, T , is given by a power law [127]:

$$\mu(T) = \mu_{ref} \left(\frac{T}{T_{ref}} \right)^{3/4}, \quad (4.13)$$

and the second coefficient of viscosity is given by $\lambda_s(T) = -2/3 \mu(T)$. It should be noted that the contribution of dilation to the shear stress is negligibly small. For each of the

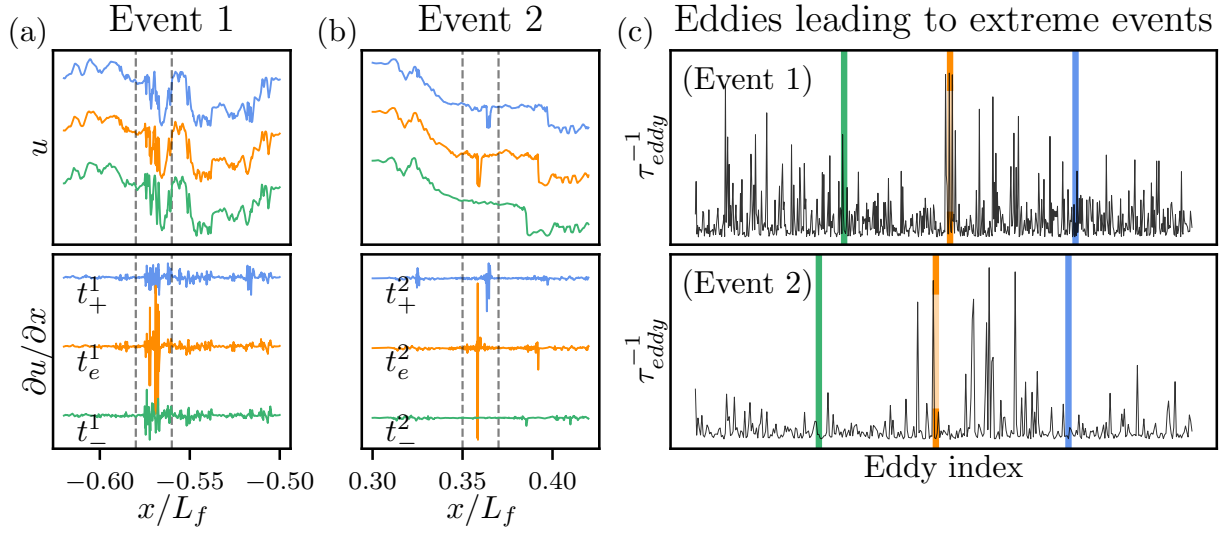


Figure 4.14: Velocity (a, b: top) and velocity derivative (a, b: bottom) in two extreme dissipation events for $Re_\lambda = 929$, at times t_e^1 ($12.05 T_{11}$) and t_e^2 ($13.09 T_{11}$), within the x -range (normalized with L_f) depicted by the vertical dashed lines. The profiles immediately before and after the extreme event are also shown at times t_- and t_+ , which are in immediate vicinity of the studied event. The inverse eddy time scale of the invoked eddies at these extreme events are shown in (c), where individual eddies are identified by an index.

simulated Re_λ cases, the reference values of temperature (T_{ref}) and density (ρ_{ref}) are set to unity and reference kinematic viscosity (ν_{ref}) is tabulated as ν in Table 4.1.

The initial thermodynamic conditions of the simulation are set to the reference values, and the molecular mass of the fluid (\mathcal{M}) is selected to ensure a low turbulent Mach number ($M_t = u' / \sqrt{\gamma(R_u/\mathcal{M})T}$), where R_u is the universal gas constant. Similarly, the reference pressure, P_{ref} is calculated using the ideal gas law using the previously discussed gas constant.

As mentioned in section 4.3.1, the domain mean temperature is observed to rise as the simulation proceeds due to the inherent periodicity of the domain, the imposed forcing, and the fact that viscous dissipation results in an increase in the internal energy. Given the low Mach number of the simulation, this temperature increase remains modest (at the low Mach numbers), thus we opted to not model an energetic sink term to artificially maintain a constant temperature across the computational domain. The temperature increase can be mitigated by increasing the domain size relative to the forcing length scale, albeit with increased computational cost. In this work, we see a variation of less than 10 percent in the mean pressure and temperature over the entire simulation period, which still maintains the M_t much smaller than unity and only slightly modifies the viscosity.

The transient heating due to pressure work, which is partly reversible and not strictly dissipative, along with the non-zero second coefficient of viscosity (λ_s), likely impacts the overall energy balance. The dissipative numerical transport in the time advancement of equation (4.2) also affects the validity of dissipation rate computation via equation (4.10).

4.5 Discussion

We developed a compressible, Eulerian-based ODT framework for the study of extreme Reynolds number HIT by modelling for the normal derivatives. The validity of the ODT generated turbulence is systematically ascertained across a range of Re_λ . Although the equivalent DNS at $Re_\lambda \approx 1250$ required nearly 2 billion grid points and massive computational power [64], the present calculations were performed on a single core. To establish

the applicability of this method to further explore extreme Reynolds numbers, an estimation of the computational efficacy of ODT versus DNS is essential. The computational cost is quantified by the number of degrees of freedom in the system corresponding to all computations in the solution process.

The steps in space (N) and time (T) contribute to the net degrees of freedom $df \sim (N^n T)$ for an n dimensional system [136]. When resolving the smallest scales with a uniform grid, both N and T scale as $\sim Re_\lambda^{3/2}$ [136], thus $df \approx (Re_\lambda^{3/2})^{n+1}$. The scaling of computational cost with Reynolds number relates directly to the degrees of freedom, which is shown in figure 4.15(b) for the one-dimensional model ($n = 1$) versus the DNS ($n = 3$). It is observed that the cost scaling for the present model closely aligns with the scaling for $n = 1$, showing the cost advantage gained by the reduced dimensionality of the model.

Although ODT can never replace DNS or experiments of high Reynolds number HIT due to the inherent modelling and approximations, it does provide a valuable surrogate model to understand the dynamics of the turbulence. Despite the modelling and approximations, ODT is able to capture salient features of high-Reynolds number turbulent flows. ODT performs well in matching the Kolmogorov-scaled spectrum, mean dissipation and skewness characteristics. The statistical approach of ODT provides a qualitative agreement in the dissipation rate PDFs, albeit with a higher occurrence of extreme events. The statistical variation of velocity derivative skewness produced using ODT is large, which can be attributed to the single line-of-sight dataset, and a much longer run in units of T_{11} might be required for ODT to attain the same statistical precision as DNS results. Hence, the computational savings achieved by dimensional reduction are accompanied by a reduced sample size, which lowers the statistical precision. The current compressible formulation leads to strong artificial compressible effects due to the inadequacy of the forcing method in the compressible regime, which allows a major fraction of the injected energy to be converted into pressure work. The future work can focus on an improvement of forcing scheme, however, this remains challenging since the one-dimensional approach does not allow an easy adoption of a forcing schemes similar to those used in DNS. In the absence of specifically designed forcing schemes, the unmodified incompressible ODT approach would be preferable for generating HIT in incompressible flows since it does not

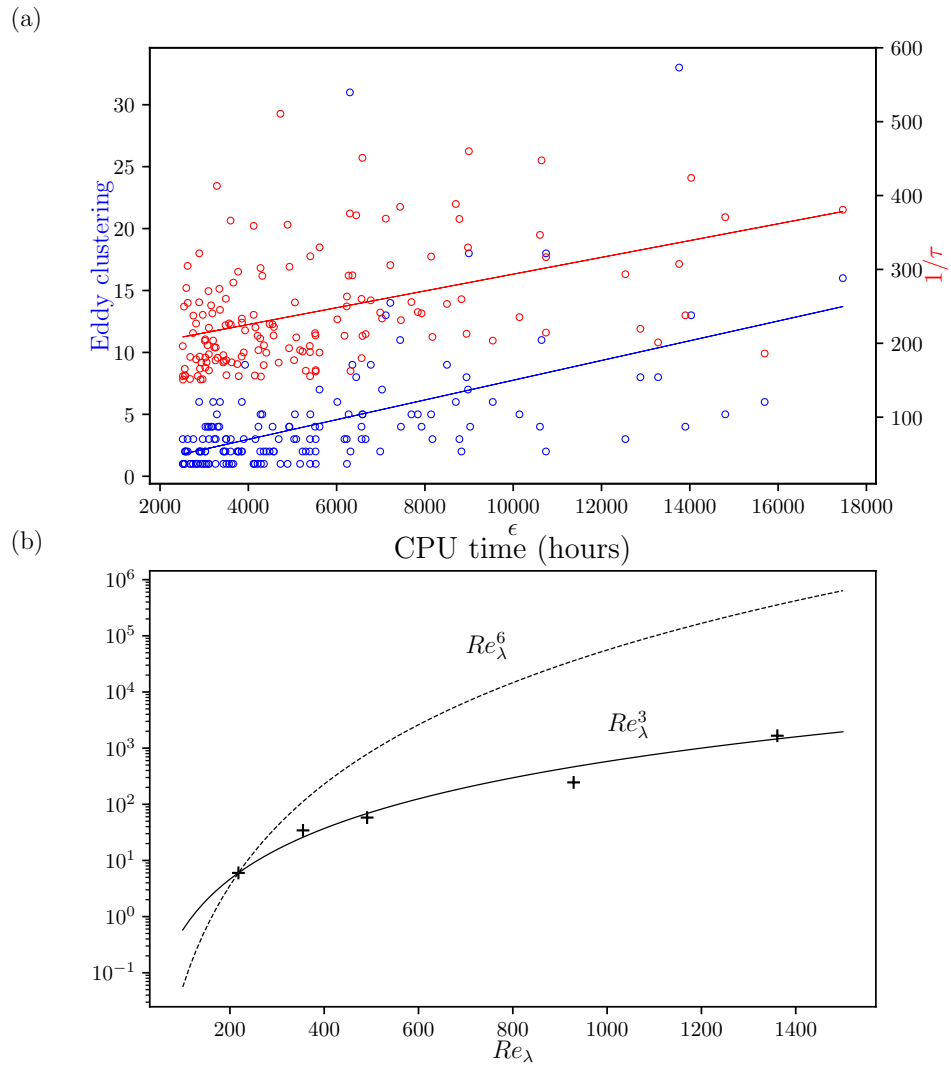


Figure 4.15: (a) Positive correlation of extreme dissipation with eddies at large $1/\tau$ and clustering density. (b) Scaling of computational cost as a function of Re_λ .

provide a pathway for domain heating. The ODT approach, due to its nimble computational and memory costs, can provide an alternative methodology for studies of high-order statistics and extreme fluctuations, though at reduced fidelity, in high-Reynolds number stationary turbulence that would otherwise be unachievable.

Chapter 5

Features of the Attached-Eddy hypothesis in One-Dimensional Turbulence models of turbulent boundary layers

Associated reference:

Nath, Pranav and Hickey, Jean-Pierre, “Features of the Attached-Eddy hypothesis in One-Dimensional Turbulence models of turbulent boundary layers”, under revision in *Physical Review Fluids*.

Abstract

The complexity of wall-bounded turbulent flows has given rise to a variety of models that capture the essence of this physical problem; yet many of these models are built on different modelling assumptions. One of the most compelling models is Townsend’s Attached Eddy Model (AEM) which is predicated on the assumption that the eddies have a geometric scaling with the distance from the wall and a constant characteristic velocity. With a limited set of modelling assumptions, AEM is able to capture many of the preponderant

features of the turbulent boundary layer (TBL) such as the log-layer and Reynolds stress distributions. Other models, such as the stochastic ODT model from Kerstein [78], are built on a completely different set of modelling assumptions, yet show similarly convincing agreement when modelling the TBL. In this work, we re-write the ODT formulation as a Markov process and simplify some modelling assumptions, which allows us to recast the equations into a form analogous to AEM. By distilling and simplifying ODT, we highlight the implicit similarities in the modelling assumptions found in AEM, which underscores the importance of (i) the eddy-probability estimation and (ii) the functions associated with the displacement and velocity induced by the eddy events. Comparison of the stochastic ODT model with a structural AEM model helps to identify the key features in TBL modelling along with some of the shortcomings in each of these models.

5.1 Introduction

A model is a simplified representation of a more complex physical reality, which is useful in understanding experiments, grounding theoretical frameworks, or developing other physics-based modelling approaches. The model must capture the essence of the physical problem while selectively neglecting the less relevant aspects; thus, simplification is an inherent component of model development. Physical models are most effective when they are conceptually and mathematically simple while simultaneously retaining the main features of the complex reality.

Due to the complexity of turbulent flows, a number of physical models have been proposed. The most common models in turbulence, such as those developed by Kolmogorov, Taylor, or Batchelor, view turbulence through a statistical lens. Statistical models are often derived from the governing equations of fluid motion predicated on a number of simplifying assumptions. Others, such as Townsend, have taken a structural [19], phenomenological, or even a mechanistic view of turbulence. These structural models typically understand turbulence as a superposition of structures, from which basic properties can be derived. Both statistical and structural models represent the same physical reality, yet conceptually

the models differ in their fundamental representation of the nature of turbulence.

Phenomenological or structural models for describing turbulence take many forms. One example is the shell or multi-fractal models [10] in which non-linear coupling across different scales is introduced to capture the features of the Navier-Stokes equations such as the energy cascade and intermittency [25]. Other models describe turbulence through the actions of coherent structures in the flow. Yao and Hussain [184] proposed a physical mechanism for the energy cascade through a sequence of vortex reconnection events, thus imparting greater relevance to coherent structures in describing the dynamics of turbulence; similar ideas have been extended to quantum turbulence [156]. One of the most common phenomenological models in wall-bounded flows is arguably the AEM [170]. AEM relies on the conceptual understanding that wall-bounded turbulence can be viewed as the superposition of self-similar structures whose sizes scale with the distance from the wall. Although AEM was first proposed by Townsend about half a century ago, its relevance in describing wall-bounded turbulence has not waned [112] as the model brings together the qualitatively observed coherent structures with the ability to explain critical aspects of wall-bounded turbulence. Perry and Marusic [131] showed that AEM can capture the logarithmic profile and shear stresses, but, the wall-attached eddies could not correctly represent the normal stresses. To address the mismatch in the normal stresses, an additional set of eddies that are detached from the wall were introduced to produce the realistic wake structure [131]. The features of AEM were used to study the logarithmic region in the experimental boundary layer flow [113].

Stochastic-based models have also gained prominence due to their ability to capture key features of turbulence. One such model, developed by Kerstein in the 1990's [78], is the ODT. At its core, ODT solves the NS equations along a single direction, typically in the direction of the largest gradient, and models the convective effects of turbulence through a sequence of eddy events that are stochastically applied in time. These eddy events are meant to replicate the convective transport of three-dimensional eddies acting in the one-dimensional domain. The dimensional reduction results in significant computational savings with a DNS-like spatio-temporal resolution (in one dimension) but must rely on some important modelling assumptions. These stochastic-based models have given rise to

subgrid-scale models for LES [115], have been used to model spatially evolving free shear flows [40, 154], for combustion [96, 74, 73], isotropic turbulence [122] and to approximate wall-bounded turbulent flows [150, 116, 41, 85, 20, 44].

Although AEM and ODT differ greatly in their approach to describing wall-bounded turbulence—AEM focussing on structural features and their scaling while ODT describes a sequential series of stochastic events—both models exhibit subtle commonalities that should be underscored. In fact, the link between the stochastic eddies of ODT and the AEM phenomenology has been alluded to in Klein and Schmidt [84]. AEM and ODT are able to convincingly replicate key first- and second-order statistics of wall-bounded turbulence, thus exploring the similarities between these models helps to isolate the essence of turbulence dynamics in these flows. If the features of the TBL arise from the similarities in these two distinct approaches, it can be inferred that an effective representation of future wall-bounded turbulence models can utilize these similarities. In AEM, the turbulence statistics are the result of the spatial distribution of hierarchical eddies and their induced velocities. In ODT, on the other hand, the time-integrated profiles emerge from the physical principles governing the time-varying probabilities of these eddy events. There is a common set of building blocks in both AEM and ODT that we seek to explore and form the basis of enquiry in this work. These are:

1. **Geometric approach to turbulent eddies:** AEM utilizes vortex tubes attached to the wall and ODT uses linear eddies.
2. **Well-defined probabilities of occurrence of the eddies:** AEM explicitly links eddy probabilities to wall-normal distance; however, ODT evaluates eddy probabilities taking into account the available energy for eddy generation, which varies temporally as well as spatially.
3. **Eddies induce velocity changes in the domain:** AEM infers velocities from a vortex line and ODT induces velocity change by virtue of the mapping structure.
4. **Aggregate behaviour of eddies:** AEM explains the wall structure with a static superposition of eddies and ODT constitutes a sequence of eddies in time, each eddy

with instantaneous occurrence.

Section 5.2 provides a brief description of the AEM and ODT models, followed by the analysis of mean velocity profile and Reynolds stresses arising from the considered eddy structures, in section 5.3. The shared essence of ODT and AEM models inferred from the analysis is discussed in section 5.4.

5.2 Theoretical modelling framework

5.2.1 AEM: Eddies at multiple scales

AEM uses superposition of hierarchical eddies with a pre-defined eddy structure to model wall turbulence; these three-dimensional eddies induce velocities, thus, resulting in mean flow profiles and Reynolds stresses, see figure 5.1. The original work by Townsend [170] emphasized the structure of the velocity fields, and did not prescribe the shape nor distribution of eddies. Perry and Chong [130] used hierarchical eddies whose shapes and heights varied; geometrically self-similar eddies were later used by Perry and Marusic [131]. Marusic [111] further refined the work of Perry and Marusic [131] by establishing the importance of coherent structures in the prediction of mean flow profiles, Reynolds stresses, and transport processes.

The significance of attached eddies has been confirmed experimentally in the manifestation of zonal structures with uniform momentum (UMZs) within the turbulent boundary layer [158]; these UMZs emerge from the structural understanding of the turbulent boundary layer by Adrian *et al.* [3]. Organization of the coherent structures as hairpin vortices or packets and their impact in the study of wall turbulence has been explored by Refs. [1, 181, 2].

AEM generally assumes the constitutive building block of the turbulent boundary layer to be a self-similar hairpin-shaped vortex rod or vortex tube. The average flow statistics in the turbulent boundary layer can be computed through the integration of the contribution

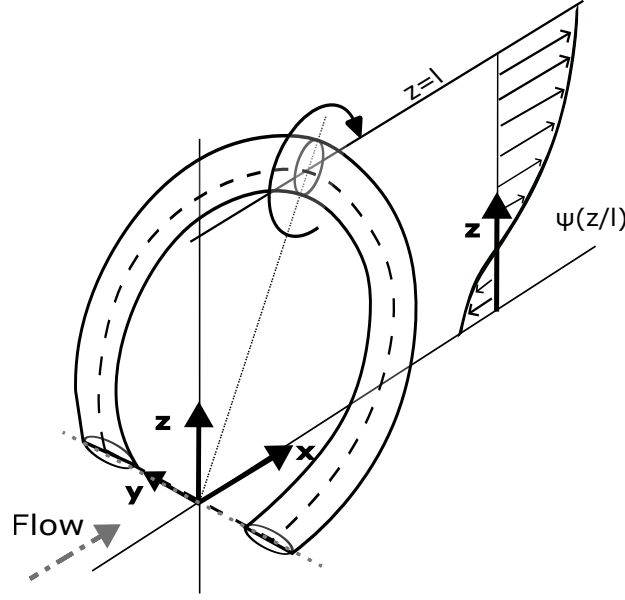


Figure 5.1: Representative vorticity distribution or intensity functions $\psi(z/l)$ of AEM.

of all the hierarchies of these self-similar eddies. The z -direction represented by index $i = 3$ is oriented normal to the wall, and the x ($i = 1$) and y ($i = 2$) axes are placed along the streamwise and spanwise directions, respectively. We use $\Psi(z)$ to represent any mean flow property in the boundary layer such as the mean spanwise vorticity $\Omega = d\langle u_1 \rangle(z)/dz$ or Reynolds stresses $\langle u'_i u'_j \rangle(z)$. We assume the eddy size, l , varies from $\delta_1 \approx 100\delta_\nu$ to the boundary layer thickness (δ_c). Here, δ_ν is the viscous wall unit defined as the ratio of kinematic viscosity (ν) to friction velocity (U_τ). Thus, we can define the mean flow property $\Psi(z)$ as:

$$\Psi(z) = \int_{\delta_1}^{\delta_c} \psi(z/l) P_H(l) dl, \quad (5.1)$$

where $\psi(z/l)$ is the contribution of the self-similar eddies of size l at the wall distance z ; this contribution is computed based on the induced velocity field of the eddies using the Biot-Savart induction law. The term $P_H(l)$ represents the probability density of the occurrence of eddies of size l . The definition of the functions $\psi(z/l)$ and $P_H(l)$ is therefore

central to AEM. The contribution of eddies at scale l is given through the function:

$$\psi(z) = F_{AEM}(l, U_\tau, \Gamma(z/l), \mathbb{Q}(l/\delta_c)), \quad (5.2)$$

where F_{AEM} is a function that depends on l and U_τ , which are respectively the eddy length scale and friction velocity, but also on $\Gamma(z/l)$, the isolated effects of the geometry of vorticity distribution, and $\mathbb{Q}(l/\delta_c)$, the characteristic velocity scaling (represented by the ratio of the characteristic velocity scale U_o to friction velocity U_τ). The function F_{AEM} takes different forms for mean spanwise vorticity and Reynolds stress formulations, see Eqs. (5.4) and (5.6) below. Interested readers can refer to Perry and Marusic [131] for more details.

The probability density function, P_H , in equation (5.1), is assumed to be inversely proportional to the length of the eddy; thus, smaller eddies occur more frequently as expected. The -1 power law probability density of occurrence is corrected by the departure term $\mathbb{D}(l/\delta_c)$. The spatial variation of the probability density $P_H(l)$ along the wall can also be incorporated into the function $\mathbb{D}(l/\delta_c)$, but is neglected in this study. Thus, the probability density function is defined as:

$$P_H(l) = l^{-1}\mathbb{D}(l/\delta_c). \quad (5.3)$$

Using the above definitions, we can define the mean spanwise vorticity normalized by the friction-velocity U_τ as:

$$\Psi_1(z) = \frac{d\langle u_1 \rangle / U_\tau}{dz} = \int_{\delta_1}^{\delta_c} \Gamma_1(z/l) \mathbb{Q}(l/\delta_c) \mathbb{D}(l/\delta_c) \frac{1}{l^2} dl, \quad (5.4)$$

where the geometry of the vorticity distribution can be defined as [131]:

$$\Gamma_1(z/l) = \frac{2}{q^2} \int_{-\infty}^{\infty} \int_{-\infty}^{\infty} \frac{\Omega}{\Omega_o} (\hat{\mathbf{t}} \cdot \mathbf{j}) d(x/l) d(y/l). \quad (5.5)$$

Here, $\hat{\mathbf{t}}$ refers to the tangential coordinate along the eddy-vortex line, \mathbf{j} is the unit vector along the y-axis in figure 5.1 and Ω / Ω_o refers to the local vorticity and effective vorticity within the vortex rod, respectively. The geometric constant q is the ratio of vortex rod radius to eddy size.

Similarly, we can define the Reynolds stresses normalized using the friction-velocity U_τ as $\Psi_2(z) = \langle u'_i u'_j \rangle / U_\tau^2$, to obtain:

$$\Psi_2(z) = \frac{\langle u'_i u'_j \rangle}{U_\tau^2} = \int_{\delta_1}^{\delta_c} \Gamma_2(z/l) \mathbb{Q}^2(l/\delta_c) \mathbb{D}(l/\delta_c) \frac{1}{l} dl, \quad (5.6)$$

where,

$$\Gamma_2(z/l) = I_{ij}(z/l) = \int_{-\infty}^{\infty} \int_{-\infty}^{\infty} \frac{V_i V_j}{U_o^2} d(x/l) d(y/l). \quad (5.7)$$

Here, V_i corresponds to i^{th} velocity component computed from the Biot-Savart law and the function I_{ij} is known as the intensity function. The formulation of integrals in Eqs. (5.4) and (5.6) is typically followed by logarithmic transformations of the integral to aid in the solution procedure.

The choice of eddy shapes exerts a strong influence on the mean spanwise vorticity and Reynolds stresses. This dependence is established through the terms $\Gamma_i(z/l)$ where ($i = 1, 2$), which are primarily a function of the geometry of the non-dimensional vorticity distribution, see Eqs. (5.5) and (5.7).

The resulting one-dimensional formulations of the integrals in Eqs. (5.4) and (5.6) serve as the foundation for the comparison with the one-dimensional ODT formulation. In the next section, we introduce essential elements of ODT to lay the foundation for deriving simplified models to compare with AEM.

5.2.2 ODT: Stochastic turbulence modelling

A number of works have established that ODT can successfully model the statistics in a zero-pressure gradient turbulent boundary layer [140, 85, 44]. In ODT, stochastic eddy events emulate the three-dimensional turbulent eddies acting along a one-dimensional domain using a geometric map. The fluid flow evolves in time with recurrent, yet stochastic, interruptions by the instantaneous eddies at different locations in the domain. An overview of the theoretical basis for ODT is presented out of completeness; interested readers can consult Refs. [78, 80, 6, 95] for additional details.

A turbulent eddy interacts with the ODT velocity profile by rearranging the spatial ordering of fluid parcels within some interval of the one-dimensional domain. We position the coordinate system along the wall in a manner identical to the AEM description in section 5.2.1. These linear eddies, represented as a predefined mapping known as a triplet map (see equation (5.8)), introduce higher wave numbers in the domain which are able to mirror the energy cascade. The triplet map can be mathematically defined as:

$$f(z) = z_o + \begin{cases} 3(z - z_o), & z_o \leq z \leq z_o + \frac{1}{3}l \\ 2l - 3(z - z_o), & z_o + \frac{1}{3}l \leq z \leq z_o + \frac{2}{3}l \\ 3(z - z_o) - 2l, & z_o + \frac{2}{3}l \leq z \leq z_o + l \\ z - z_o, & \text{otherwise.} \end{cases} \quad (5.8)$$

Three copies of the eddy region are made, compressed to one-third its original size and stitched together with the middle region inverted, see figure 5.2. The mapping is measure-preserving for all the mapped variables and their moments, and does not introduce any jump discontinuities. In equation (5.8), z_o is the start location of the eddy and l is the eddy size. Furthermore, a probability density function is defined for the eddy frequency; which defines the probability of occurrence of an eddy of size l and start location z_o . To account for tendency to isotropy, a post-triplet-map velocity transformation is carried out: $u_i(z) \rightarrow u_i(f(z)) + c_i K(z)$, where u_i is the i^{th} velocity component. The coefficient c_i is introduced to specify the amount of kinetic energy transfer amongst the velocity components and the kernel function, $K(z)$, is defined as:

$$K(z) = f(z) - z. \quad (5.9)$$

In general, the ODT eddies can have a start location, z_o , away from the wall. The frequency of occurrence of an eddy of size l and start location z_o at the fixed time t is the inverse of the time scale $\tau(z_o, l; t)$ associated with the eddy. To obtain a probability density for eddy frequency, a normalizing factor $\Lambda(t)$ is defined by integrating the eddy frequency ($1/\tau(z_o, l; t)$) over all the eddy start locations (z_o) and sizes (l):

$$\Lambda(t) = \int_{z_o=0}^{\infty} \int_{l=0}^{\infty} \frac{1}{\tau(z_o, l; t)} dz_o dl. \quad (5.10)$$

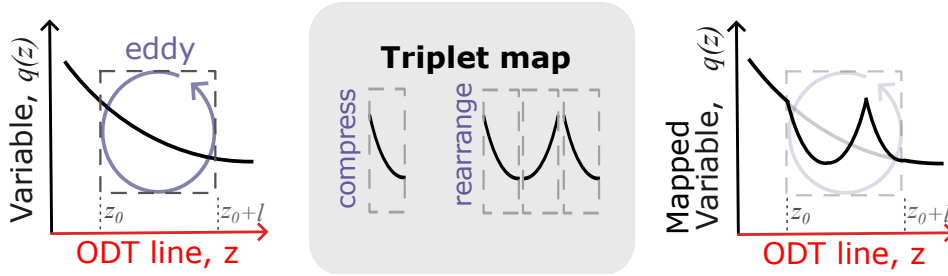


Figure 5.2: Representation of the triplet-map in ODT.

Thus, a bivariate probability density function for eddy frequency can be given as:

$$g(z_o, l; t) = \frac{1/\tau(z_o, l; t)}{\Lambda(t)}, \quad (5.11)$$

where the probability of occurrence of eddies in the parameter bin $z_o \in [z_o, z_o + dz_o]$, and $l \in [l, l + dl]$ is given by $g(z_o, l; t)dz_o dl$.

Since the continual reconstruction of $g(z_o, l; t)$ and $\Lambda(t)$ at each time step entails a high cost, a select-and-decide eddy-sampling procedure is utilized in ODT. The eddy sampling is carried out via a discrete Poisson process at a rate which is set much higher than $\Lambda(t)$, and most of the eddies are then rejected based on the select-and-decide procedure. However, for the analytical formulations used in the current work, we adopt a time-averaged form of the eddy frequency probability density $g(z_o, l; t)$. The quantity $\Lambda(t)$ averaged over time can be represented by a constant $\hat{\Lambda}$, which acts as the normalizing factor for $g(z_o, l)$, and has dimensions of $length^2/time$. Hence, the time-averaged eddy frequency probability density takes the form:

$$g(z_o, l) = \frac{1}{\tau(z_o, l)\hat{\Lambda}}. \quad (5.12)$$

The eddy time scale is a function of the extractable energy (E_{kin}) from the flow in the region where the eddy occurs [6, 74]:

$$\frac{1}{\tau(z_o, l)} = \frac{1}{l} \sqrt{E_{kin}}, \quad (5.13)$$

where the extractable energy using the kernel mechanism is:

$$E_{kin} = (1 - \omega)u_{1,K}^2 + \frac{\omega}{2}(u_{2,K}^2 + u_{3,K}^2), \quad (5.14)$$

where $u_{i,K}$ is given by:

$$u_{i,K} = \frac{1}{l^2} \int_{z_o}^{z_o+l} u_i(f(z))K(z)dz. \quad (5.15)$$

Here, u_i refers to the i^{th} velocity component with $i = 1, 2$ and 3 . The parameter ω is used to control the inter-component energy transfer. $\omega = 1$ causes the maximum inter-component energy transfer, and $\omega = 2/3$ leads to the equipartition of available energy among velocity components. $\omega = 1$ has been shown to be advantageous for some flows [80], and other works reported low sensitivity [6]. In this work, we choose $\omega = 0$ to suppress the inter-component transfer. In standard ODT formulations, a viscous penalty term E_{vp} is subtracted from E_{kin} in equation (5.13) to disallow the eddies that are smaller than a specific size, adding a viscous mechanism to the solution procedure. This work ignores the viscous penalty term, to focus on the central elements of the ODT formulation.

For constant-density flows, equation (5.15) can be simplified by making use of the measure-preserving property of the map, $f(z)$, in equation (5.8) along with the kernel function definition in equation (5.9) and takes the form [6]:

$$u_{i,K} = \frac{4}{9l^2} \int_{z_o}^{z_o+l} u_i(z) (2(z - z_o) - l) dz. \quad (5.16)$$

This latter formulation is slightly more amenable to establishing a connection with AEM. In the present work, we depart from the standard ODT formulation in our consideration of the term $u_{i,K}$. Based on equation (5.16), the value of $u_{i,K}$ is highest when the sampled eddy size is very small and a significant velocity change occurs at the length scale of the eddy. In a turbulent boundary layer, the large wall-normal gradient of the streamwise velocity component, u_1 , causes a high eddy occurrence. Henceforth, we consider $u_{1,K}$ as the main contributor to the eddy frequency and the probability density of the eddy frequency scales as:

$$g(z_o, l) = \frac{1}{\tau(z_o, l)\hat{\Lambda}} \approx \frac{1}{\hat{\Lambda}l} |u_{1,K}|. \quad (5.17)$$

In classical ODT, the eddies are invoked, accepted, and applied via the triplet mapping. This instantaneous convective step is then followed by an advancement of viscous transport.

The information transfer along the ODT line (wall-normal direction, for boundary layers) is primarily governed, outside the buffer layer, by these stochastically applied eddy events; the viscous diffusion plays a secondary role. Owing to the dominance of eddies on the flow evolution at the Reynolds numbers of interest and considering that we are relating the ODT to AEM, the current simplified ODT model ignores the diffusive processes. Hence, the sole deterministic operator, which is the diffusion step, is turned off in the stochastic PDE system considered.

5.3 Application to turbulent boundary layer

The complete ODT formulation, as presented in Stephens and Lignell [169] for example, can be used to accurately compute the mean and higher-order statistics in the turbulent boundary layer. As an illustrative example, the mean velocity profile of a turbulent boundary layer computed using a full ODT model is compared to DNS results under similar conditions in figure 5.3. The full ODT model simulates a pressure-gradient driven channel flow using a one-dimensional domain spanning across the channel, with no-slip boundary conditions on both ends and the Reynolds number ($Re = U_\infty \delta_c / \nu$) is set as 22,000, where U_∞ is the free-stream velocity (or in the case of the channel flow, the centerline velocity). The channel flow profiles are equivalent to the results for the turbulent boundary layer as a small pressure gradient drives the channel flow and the channel width is much larger than the viscous length scale.

In the present work, we simplify the full ODT formulation to its skeletal elements and into a form that resembles the formulation of AEM. Thus, it is expected that the simplified ODT model will be less accurate than the full ODT formulation. While presenting the results and further discussions, we refer to the full ODT model [169] as Full-ODT (F-ODT) and the reduced version developed and analysed in further sections of this work as Reduced-ODT (R-ODT). The simplified expression for the eddy probability distribution derived in

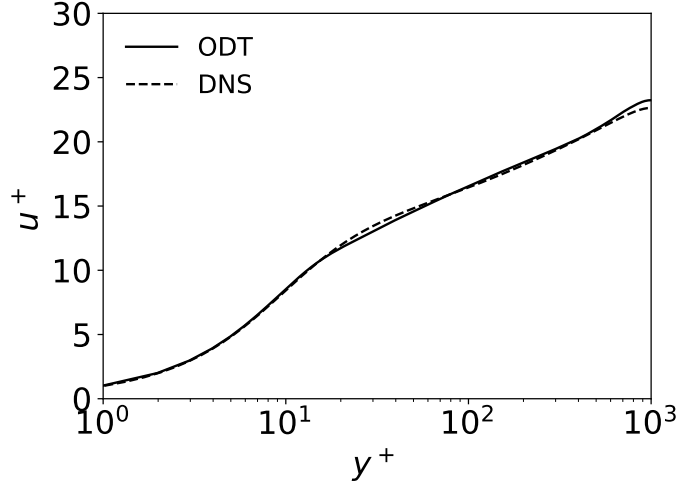


Figure 5.3: Velocity profile obtained from ODT simulation of channel flows using the F-ODT algorithm at $Re = 22,000$, where $Re = U_\infty \delta_c / \nu$, U_∞ is the free-stream velocity and ν is the kinematic viscosity. DNS results from Graham *et al.* [49].

equation (5.17) acts as an essential building block of R-ODT. The codes developed in this work can be found for reference at <https://gitlab.com/odt4/odtaem.git>.

ODT eddies are instantaneous and occur sequentially, one at a time. Furthermore, ODT is formulated in a way that transparently exhibits its Markovian character (see appendix A of Kerstein [79]). We use ODT's Markovian character to build an equivalence between the ODT procedure and AEM. Thus, the transformation due to each eddy event can be thought of as a Markov step Φ_i in a larger Markov chain of transformations that acts on the flow properties $X(z)$. The eddy size is assumed to vary from $\delta_1 \approx 100\delta_\nu$ to the boundary layer thickness δ_c unless otherwise stated.

The present work focuses on modelling the steady-state flow in the turbulent boundary layer. The steady state profiles of flow properties, for instance the velocity derivative $d\langle u_1 \rangle / dz$, are represented by the expectation value of the Markov chain given by:

$$X_n(z) = [\sum_{k=1}^n \Phi_k] X_o(z), \quad (5.18)$$

where $X_o(z)$ is the initial condition, Φ_k is the k^{th} Markov step and n is sufficiently large to attain the steady state.

Applying the Markov chain analogy to the transformation by ODT eddies, the steady-state velocity profiles can be estimated. The expected profiles of flow property X at steady state can be expressed using probabilities \hat{q}_j associated with states X_j and probabilities \hat{g}_i associated with eddies Φ_i that operate on state X_j , using:

$$X_E = \sum_i \sum_j \hat{g}_i \hat{q}_j \Phi_i(X_j). \quad (5.19)$$

Here, $0 \leq i \leq n_1$ and $0 \leq j \leq n_2$, where n_1 and n_2 are sufficiently large.

Analysis in section 5.3.1 later shows that the transformation Φ_i for vorticity distribution $d\langle u_1 \rangle / dz$ used to compute velocity profiles is linear, expressed by $\Gamma_1(z/l)$. Using linearity of the transformations Φ_i , we get $\sum_j \hat{q}_j \Phi_i(X_j) = \Phi_i(\sum_j \hat{q}_j X_j)$, and equation (5.19) simplifies to:

$$X_E = \sum_i \hat{g}_i \Phi_i \left(\sum_j \hat{q}_j X_j \right), \quad (5.20)$$

where, the term inside curved brackets is the expected value of state X at steady state, given as $X_E = \sum_j \hat{q}_j X_j$. Thus, equation (5.20) can be expressed as:

$$X_E = \sum_i \hat{g}_i \Phi_i(X_E). \quad (5.21)$$

Instead of discrete probabilities of eddy events, if we use the probability density function for eddy occurrence, $g(\Phi_i)$, spanning over the entire range of potential eddies, the expectation value from equation (5.21) can be expressed as:

$$X_E = \int \Phi(X_E) g(\Phi) d\Phi. \quad (5.22)$$

Hence, the aggregate effect of eddies as Markov transformations is analogous to the superposition of eddies in AEM (see equation (5.1)). We explore the implications of this analogy with regard to the assessment of the mean velocity profile and the Reynolds stresses for the turbulent boundary layer. It should be noted that the formulation of equation (5.22) is predicated on the assumption of eddies dominating the flow evolution in R-ODT, which justifies the neglect of viscous diffusion.

5.3.1 Capturing the logarithmic mean velocity profile

We approach the reconstruction of the mean velocity profile by computing the vorticity induced by eddies at different wall-normal locations. Viewing ODT as a Markov process as defined in equation (5.22), the mean spanwise vorticity $d\langle u_1 \rangle/dz$ at a location z is expressed as the superposition of vorticity contributions $\Omega(z, l)$ from individual ODT eddies of size l and start location z_o , see equation (5.23). We include the start location in equation (5.23) to account for the eddies that are both detached and attached to the wall.

$$\frac{d\langle u_1 \rangle}{dz} = \int_{l=\delta_1}^{\delta_c} \int_{z_o=0}^{\delta_c} \Omega(z, l) g(z_o, l) dz_o dl, \quad (5.23)$$

where $g(z_o, l)$ refers to the probability density of occurrence of eddy of size l and starting location z_o . The mean spanwise vorticity can be used to reconstruct the velocity profile. The terms in the integrand of equation (5.23), $\Omega(z, l)$, and $g(z_o, l)$, help us to construct a reduced ODT model (R-ODT) that resembles equation (5.4) of AEM. A brief description of the evaluation of these terms follows.

The probability density of eddy occurrence, $g(z_o, l)$, follows from equation (5.17), where the term $u_{1,K}$ is a function of the instantaneous velocity profile $u_1(z)$ in F-ODT. Wall-detached eddies ($z_o > 0$) are permitted in F-ODT, similar to the AEM models [131] in which it was necessary to introduce the detached eddies for reconstructing the wake structure. Though ODT admits eddies that originate above the wall, a large fraction of eddies are in the vicinity of the wall, as observed from F-ODT results and by evaluating $g(z_o, l)$ using a typical steady-state logarithmic velocity profile $u_1(z)$ (universal law-of-the-wall). The prominence of eddies attached to the wall is evident by the large $g(z_o, l)$ at small values of z_o in figure 5.4. It should be noted that a logarithmic velocity profile $u_1(z)$ is used solely to comment on the dominance of wall-attached eddies, and the velocity profile is not directly assumed in this work. The current model independently computes the velocity profile, as will be shown. The prevalence of wall-attached eddies is valid even during the initial evolution of the ODT simulation, before the logarithmic velocity profile develops, as an outcome of the large velocity gradients at the wall introduced by the no-slip boundary condition. Based on the predominance of eddies in the vicinity of wall, we assume that the

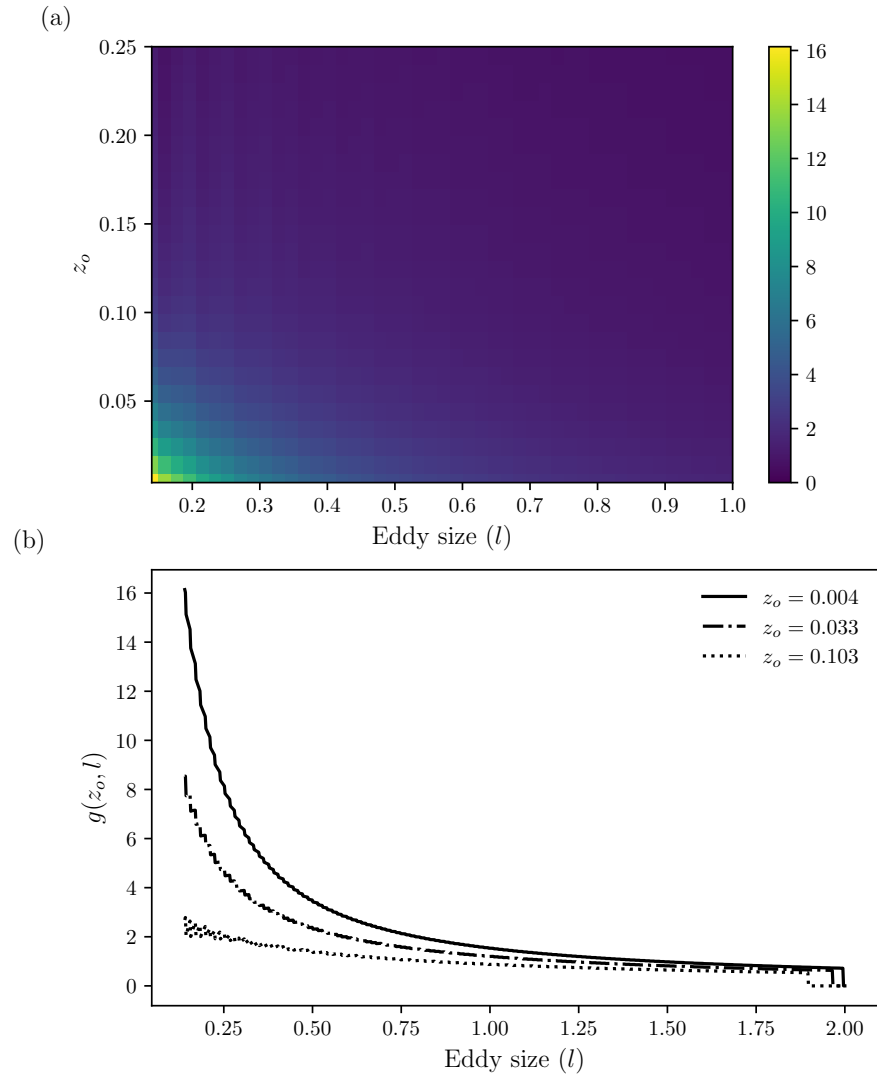


Figure 5.4: (a) Contours of $g(z_o, l)$ as defined in equation (5.17) for turbulent boundary layer flow and (b) $g(z_o, l)$ corresponding to three different eddy start locations, from the R-ODT formulation.

R-ODT eddies always start at the wall, and equation (5.23) simplifies to:

$$\frac{d\langle u_1 \rangle}{dz} = \int_{l=\delta_1}^{\delta_c} \Omega(z, l) g_o(l) dl, \quad (5.24)$$

where $g_o(l)$ is the PDF for the occurrence of the eddy of size l , with the eddy-start location fixed at $z_o = 0$. The PDF $g_o(l)$ can be defined by normalizing the joint PDF $g(z_o = 0, l)$ by $\int_l g(0, l) dl$, using:

$$g_o(l) = \frac{g(z_o = 0, l)}{\int_{l=\delta_1}^{\delta_c} g(0, l) dl}, \quad (5.25)$$

The term $\Omega(z, l)$ is computed using the vortex line formulation in AEM, whereas in the current R-ODT model, the vortical motion associated with ODT eddies is used to evaluate this term. The equivalent vortical motion induced by the eddy is assessed based on an estimate of the eddy kinetic energy, which can be expressed as $\langle d^2 \rangle / \tau^2$, where $\langle d^2 \rangle = 4/27 l^2$ represents the mean square eddy-induced fluid displacement in the eddy region resulting from the vortical transfer by a size- l eddy [78]. The vorticity induced by an eddy can be given as $\Omega_{net}(l) \sim 1/\tau(l)$. From this simplification, we can write:

$$\Omega_{net}(l) = \frac{1}{l} \underbrace{\frac{4}{9l^2} \int_0^l u_1(z)(2z - l) dz}_{u_{1,k}} \quad (5.26)$$

Based on equation (5.26), one arrives at the vorticity induced at the wall-normal distance z by the eddy of length l as:

$$\Omega(z, l) = \frac{4}{9l^2} u_1(z)(2z - l). \quad (5.27)$$

Here, only the eddies that encompass the current z location, with eddy size $l \geq z$, induce spanwise vorticity at z , and this is enforced using the Heaviside-step function $H(l - z)$. This is also evident from figure 5.5(a), where the induced vorticity is zero when $z \geq l$ and $z/l = m$ refers to the start point of the simulation region next to the wall at $z^+ = 100$.

Substituting $\Omega(z, l)$ from equation (5.27) in equation (5.24) and normalizing by the friction velocity U_τ , we get:

$$\frac{d\langle u_1 \rangle / U_\tau}{dz} = \int_{\delta_1}^{\delta_c} \frac{4}{9l^2} \frac{u_1(z)}{U_\tau} (2z - l) H(l - z) g_o(l) dl. \quad (5.28)$$

We analyse the formulation of equation (5.28) to ascertain the equivalence of individual terms with AEM, followed by a direct numerical integration of the equation to substantiate the creation of a linear logarithmic region in this R-ODT model.

Equation (5.28) can be converted to the form of equation (5.4) of AEM by rearranging the terms and substituting $g_o(l) \approx 1/l$, which has been depicted in figure 5.4 and corresponds to a -1 probability power law. We obtain:

$$\frac{d\langle u_1 \rangle / U_\tau}{dz} = \int_{\delta_1}^{\delta_c} \frac{4}{9} \frac{u_1(z)}{U_\tau} \left(\frac{2z}{l} - 1 \right) H(l-z) \frac{1}{l^2} dl. \quad (5.29)$$

The expression on the right-hand side of equation (5.28) exhibits similarities to the AEM formulation: (i) the eddy probability density: $g_o(l) \approx 1/l$ (see equation (5.3)), (ii) a linear vorticity distribution $\Gamma_1(z/l) \approx (2z/l - 1)$, similar to the third category of type-A eddy considered [131], and (iii) the velocity scaling: $u_1(z)/U_\tau$. The velocity scaling in the current model differs from AEM, as the latter uses the eddy characteristic velocity scale U_o , instead of the local velocity $u_1(z)$.

The integral to evaluate $d(\langle u_1 \rangle / U_\tau) / dz$ in R-ODT resembles that of the AEM formulations described earlier. We compute the resultant velocity profile as done in AEM. Similar to the analytical proof of the occurrence of the linearity of the logarithmic velocity profile by Perry and Marusic [131], we analyse the limiting behaviour of the terms in equation (5.29) after specific transformations. The term $u_1(z)/U_\tau$ can be approximated by the logarithmic mean velocity profile at the steady state, and marginally varies inside the log-layer especially at low l/δ_c , thus can be treated as a constant. This assumption of constancy of $u_1(z)/U_\tau$ is justified for low $l \ll \delta_c$, as is the case for characteristic eddy velocity U_o in AEM. First, we introduce the logarithmic transformations: $\xi = \log(l/z)$, $\xi_1 = \log(\delta_1/z)$, $\xi_E = \log(\delta_c/z)$, and define the function $h(\xi) = 2z/l - 1$. Then, by combining all the constants into the constant κ and defining the velocity deficit with respect to free-stream flow: $U^* = (U_\infty - \langle u_1 \rangle) / U_\tau$, we get:

$$\frac{dU^*}{d\xi_E} = \int_{-\infty}^{\infty} \kappa e^{-\xi} h(\xi) d\xi. \quad (5.30)$$

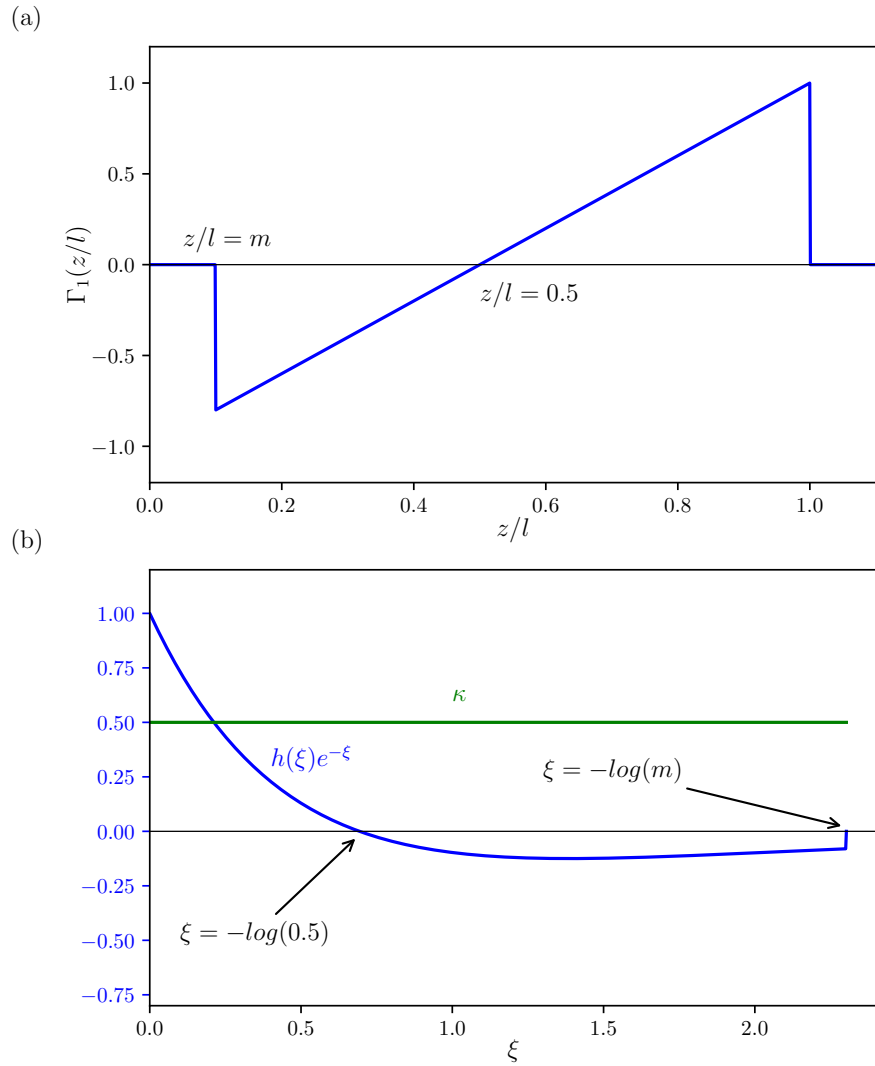


Figure 5.5: Vorticity distribution and transformed terms of equation (5.30) show similar behaviour to descriptions of third category of type-A eddy in AEM [131]. m refers to the ratio of δ_1 to the eddy size l considered.

Proving that the integral on the right-hand side of equation (5.30) is constant effectively shows that $d((U_\infty - \langle u_1 \rangle)/U_\tau)/d(\log(\delta_c/z))$ produces the log-law profile. To establish this constancy, we consider the terms in the integral as depicted in figure 5.5. The function $h(\xi)$ is non-zero only in the depicted range, and is multiplied by κ . Because κ is invariant in the considered range of ξ , the integral in equation (5.30) is independent of z , and the log law is hence recovered.

Now, considering the direct integration of equation (5.28), the probability density function $g_o(l)$ is substituted using expressions in Eqs. (5.16), (5.17) and (5.25). The evaluation of equation (5.28) involves a nested integral, where the expression for probability density accounts for all the eddies that induce vorticity at the considered location z , see equation (5.31).

$$\frac{d\langle u_1 \rangle(z)}{dz} = \int_{l=\delta_1}^{\delta_c} \underbrace{\frac{C}{l} \frac{4}{9l} u_1(z)(2z-l)H(l-z)}_I \underbrace{\left(\frac{g(0,l)}{\int_{l=\delta_1}^{\delta_c} g(0,l)dl} \right)}_{II} dl, \quad (5.31)$$

where,

$$g(0,l) = \frac{1}{\hat{\Lambda}l} \left| \frac{4}{9l^2} \int_0^l u_1(z')(2z'-l)dz' \right| \quad (5.32)$$

The velocity derivative $d\langle u_1 \rangle/dz$ obtained at each z is integrated, starting from zero velocity at the wall, to reconstruct the velocity profile for the next iteration. We add a multiplicative constant C in the integrand of equation (5.31) to adjust the turbulence intensity, analogous to the C parameter typically used in ODT simulations. Each iteration comprises of two steps: **(i)** the probability density $g_o(l)$ is computed for varying eddy sizes, using equation (5.25) and (5.32), as a functional of the current velocity profile $u_1(z)$ in term *(II)* of equation (5.31). As a result of the normalization of $g(0,l)$ to obtain $g_o(l)$ in term *(II)*, the parameter $\hat{\Lambda}$ is eliminated. **(ii)** Evaluation of the net vorticity induced at location z by the aggregate effect of individual eddies, which in turn is given by term *(I)*. The iterations are carried out until convergence to a steady-velocity profile is achieved.

The results obtained by numerical integration of equation (5.31) for various starting velocity profiles consistently produce the logarithmic region of the velocity profile, see

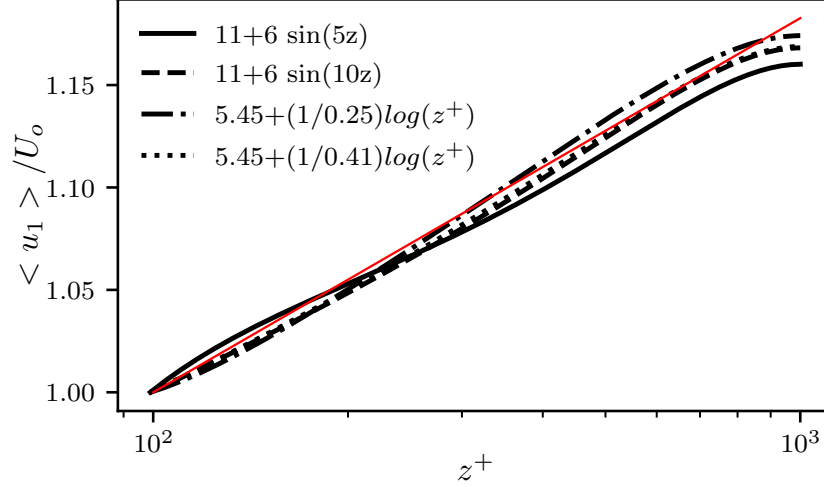


Figure 5.6: Mean streamwise-velocity profiles $\langle u_1 \rangle$ obtained for four different arbitrary initial conditions normalized with the streamwise velocity at start of log-layer $U_o(z = 100\delta_\nu)$ from the R-ODT formulation at $C = 2$ exhibit linear regions close to the wall. A line fitted to the straight section of the produced profiles are shown in red.

figure 5.6, showing that the R-ODT model captures the essence of the wall-attached eddy structure.

Increasing the ODT turbulence intensity parameter, C , causes an increased slope of the logarithmic velocity profile in the current model due to direct amplification via equation (5.31). However, increasing C in F-ODT models from Refs. [44, 140] flattens the velocity profiles farther from the wall due to the increased momentum transfer with increased eddy occurrence. This difference can be attributed to the higher occurrence of detached eddies in F-ODT models with higher values of C .

5.3.2 Reynolds stress reconstruction

F-ODT models have been reported to provide accurate predictions of turbulent stresses, with the exception of an under-prediction of the normal stresses [140]. This discrepancy is attributed to a modelling artifact arising from the inadequate treatment of three-dimensional information in the ODT formulation. Nevertheless, we study the essential elements of ODT that contribute most prominently to modelling the Reynolds stresses using the R-ODT model.

The AEM hypothesis uses the velocity components induced by the isolated eddies to infer Reynolds stresses, where the intensity functions $I_{ij}(z/l)$ are defined as being solely dependent on the geometry of the eddy. In this work, an aggregate effect of ODT eddies is considered to evaluate the Reynolds stresses. We do not use the Markov chain analogy to arrive at the steady state velocity profile for computing the Reynolds stresses. Instead, the analysis to obtain Reynolds stresses is restricted to the steady state where the logarithmic mean velocity profile is used to evaluate the eddy probabilities that are used to represent the cumulative effect of instantaneous velocity profiles. This approach of applying eddies to an assumed mean velocity profile has also been used by Movaghar *et al.* [119] to model the steady-state statistics of turbulence quantities.

Transverse normal stresses, $\langle u_3'^2 \rangle$, are estimated via the mapping-induced transverse velocity d/τ [78], see equation (5.33), where the mapping causes a displacement d over the eddy time scale τ . Here, $d(l|z)$ is the displacement induced at z by an eddy of length l ($z \leq l$), computed via the triplet-map definition [77]. The formulation for transverse normal stresses,

$$\langle u_3'^2 \rangle(z) = \int_{l=\delta_1}^{\delta_c} C \left(\frac{d(l|z)}{\tau(l)} \right)^2 H(l-z) g_o(l) dl, \quad (5.33)$$

resembles the form of equation (5.1) of AEM.

The probability density of an eddy of size l is identical to the expression substituted in equation (5.31). The integrals are evaluated only for the eddies that influence the velocity at location z . Only the eddies that encompass the current z location, with eddy size $l \geq z$, contribute to the Reynolds normal stresses, as enforced by $H(l-z)$. The transverse

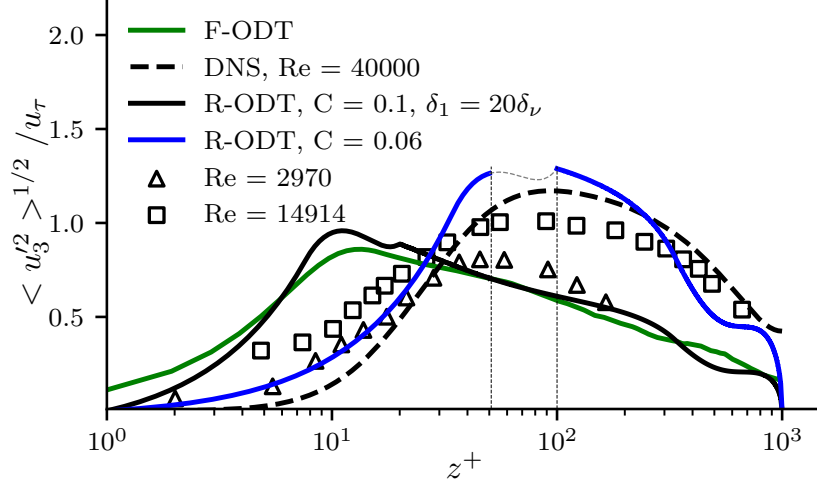


Figure 5.7: Transverse normal stress profile for two R-ODT cases and an F-ODT case at $Re = 22,000$. Experiments (symbols) from Wei and Willmarth [179] and DNS (dashed-line) results from Graham *et al.* [49]. The region between the two vertical dashed lines refers to the transition region between the buffer layer and the log-law region.

normal stress profile obtained from the current model matches the functional form from experimental results and F-ODT results, see figure 5.7. The constant C is used to scale the model results for ease of shape comparisons. The F-ODT results show a characteristic peak at about $z^+ = 10$, which was also previously reported [140]. The location of the peak in F-ODT is closer to the wall when compared with R-ODT, DNS and experimental results, and this peak location is an outcome of the smallest size of eddies considered in F-ODT. A close match of the current model with F-ODT is attained with peak location closer to the wall, if smaller eddies are permitted in R-ODT, as seen for $\delta_1 = 20\delta_\nu$ in figure 5.7. A slope discontinuity occurs at $z^+ = \delta_1/\delta_\nu$, which can be attributed to the fact that all sizes of eddies produce stresses at $z^+ < \delta_1/\delta_\nu$, however, once $z^+ > \delta_1/\delta_\nu$, the eddies that do not reach the analysed z^+ stop contributing to the stresses. This sudden jump is most pronounced in the computation of normal stresses in the vicinity of $z^+ = \delta_1/\delta_\nu$.

The ODT eddies induce mass and momentum transfer via linear eddies and the cross-correlation between streamwise and wall-normal fluctuations does not directly represent the shear Reynolds stresses $\langle u'_1 u'_3 \rangle$ in the ODT framework. An assessment of the Reynolds shear stresses follows from ensemble averaging of eddy-induced transfer of velocity components via the mapping process over time. A control volume analysis reveals that $\langle u'_1 u'_3 \rangle$ corresponds to the ensemble average net rate of advective transfer of $\langle u'_1 \rangle$ through a wall-normal location z [78, 80]. The logarithmic mean velocity profile $\langle u_1 \rangle(z)$ is used to evaluate the stresses. The evaluation of $\langle u'_1 u'_3 \rangle$ involves: **(i)** finding the net transfer of the streamwise-velocity component induced by ODT eddies, denoted by Δu_1 , per unit time interval (τ) considered. Similar to computation of Reynolds normal stresses, only the eddies that encompass the current z location contribute to the Reynolds shear stresses, as represented by $H(l - z)$. **(ii)** Integration of Δu_1 from the wall ($z = 0$) to the location z . An estimate of the net Δu_1 follows by integrating the effect of individual eddies, where the kinetic energy change induced by an eddy: $u_{1,K}^2$, is considered to compute the induced velocity. The time scale τ is computed by averaging the time scales associated with the individual eddies.

$$(\Delta u_1(z^*))_{\text{advective}} = \frac{1}{\tau} \int_{l=\delta_1}^{\delta_c} \frac{4C}{9l^2} u_1(z^*) (2z^* - l) H(l - z) g_o(l) dl \quad (5.34)$$

$$\langle u'_1 u'_3 \rangle(z) = \int_0^z (\Delta u_1(z^*))_{\text{advective}} dz^* \quad (5.35)$$

The recreated profiles for the shear Reynolds stress in figure 5.8 exhibit the characteristic $\langle u'_1 u'_3 \rangle$ profile reported for turbulent boundary layers [179]. The rise of shear Reynolds stress is observed in the viscous sub-layer and buffer layer, followed by an almost linear drop in the log-layer and beyond.

With inclusion of only the wall-attached eddies, as per the formulation in equation (5.34), the stresses drop to zero before half the thickness of the boundary layer is reached. For a realistic profile of the shear Reynolds stress, we include the detached eddies, with

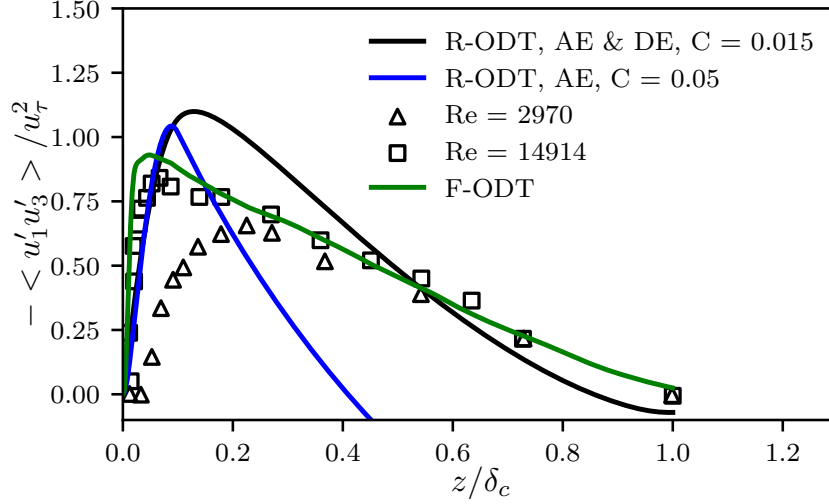


Figure 5.8: Reynolds shear stress variation in the boundary layer for two R-ODT cases and an F-ODT case at $Re = 22,000$. AE refers to R-ODT with only wall-attached eddies, and AE & DE refers to R-ODT with both attached and detached eddies. Experimental data is from Wei and Willmarth [179].

the probability density given in section 5.3.1:

$$\begin{aligned}
 (\Delta u_1(z^*))_{\text{advective}} &= \frac{1}{\tau} \int_{l=\delta_1}^{\delta_c - z_o} \int_{z_o=0}^{\delta_c} \frac{4C}{9l^2} u_1(z^*) (2(z^* - z_o) - l) \cdot \\
 &H(z_o + l - z) H(z - z_o) g(z_o, l) dz_o dl.
 \end{aligned} \tag{5.36}$$

Here, the Heaviside-step function H ensures that the eddy region $[z_o, z_o + l]$ includes the current z -location, for non-zero contribution to the Reynolds shear stresses. The obtained results for the cases including or excluding wall-detached eddies are depicted in figure 5.8, with C values chosen for ease of shape comparisons. The step increase in shear Reynolds stress in the immediate vicinity of the wall is produced by the large cumulative velocity Δu_1 induced by eddies (see figure 5.9(a)). Linear drop of $\langle u_1' u_3' \rangle$ for $z/\delta > 0.1$ is an outcome of the approximately constant value of Δu_1 in the log-law region as observed in figure 5.9(b).

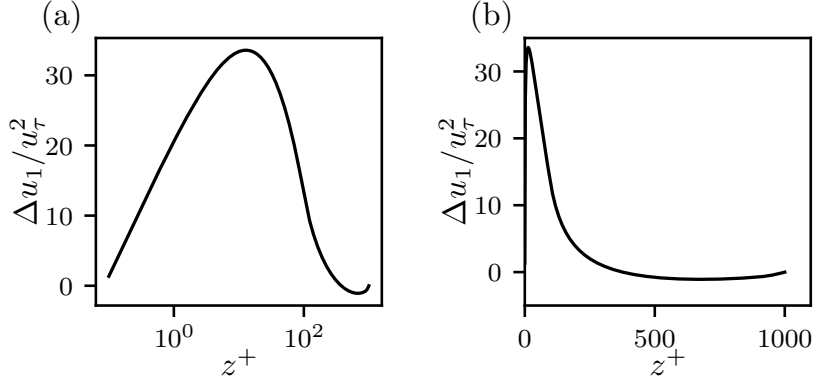


Figure 5.9: Variation of $\Delta u_1(z)$ with wall-normal distance to explain the evolution of shear Reynolds stresses in the R-ODT formulation with logarithmic (a) and linear (b) z^+ , at $Re = 22,000$.

The deliberate simplifications introduced to extract the essential features of ODT precludes exact agreement with established benchmarks reported in F-ODT simulations [140, 44]. However, the role of the velocity profiles in determining eddy probabilities, combined with the nature of the mapping, is found to have a central influence on turbulence characteristics. The transverse displacement induced by the ODT eddies, supported by the well-defined occurrence probabilities, turn out to be the major contributor in the Reynolds stress evolution with wall-normal distance. The formulation in R-ODT bears close resemblance to the AEM Reynolds stress formulations, and the role of AEM’s intensity function I_{ij} is played by the displacement function linked to the ODT eddies.

5.4 Discussion

ODT provides a dynamic one-dimensional representation of turbulence by virtue of the eddies that are operations that modify the flow state, unlike the AEM models with a hierarchy of static vortex structures that characterize the flow state. Despite this underlying difference in the nature of the two models, the averaged statistics from finite-duration ODT eddies capture the same effects as the static AEM structures in the turbulent boundary

layer.

This work isolated the essential features of ODT through a simplified formulation (R-ODT), addressing the probabilities of eddies and their aggregate effects on velocity profiles, which have been shown to produce desirable trends in wall-bounded turbulence characteristics. The simplification in complexity of the ODT model in the present work is done to recast the equations in a form that resembles AEM in order to fulfill the objectives of the work.

Following points are inferred to establish the core equivalence of the two methods, AEM and ODT , for turbulent boundary layer modelling:

1. Consistent representation of the statistics of eddy occurrences is a major factor for modelling wall-turbulence. ODT provides a generalized framework to generate eddy time-histories valid for diverse flows including free and bounded shear flows. The occurrence of ODT eddies is favoured when the mean flow gradients are high, resulting in a higher eddy frequency in the region closer to the wall, similar to the AEM hypothesis.
2. High velocity gradients arise close to the wall in ODT , irrespective of the initialized velocity profiles, by virtue of the no-slip boundary conditions. The presence of the wall is felt into the boundary layer generating the logarithmic velocity profile and AEM-like eddy structure at steady state.
3. The vorticity distribution induced by an ODT eddy, by virtue of the triplet-mapping, is similar in character to the one produced by some of the assumed eddy shapes in AEM, thus supporting the equivalence of ODT eddy geometry effects in addition to the similarity to eddy-occurrence probabilities of AEM.
4. AEM structures are not external to the flow field, but in fact they are the Fourier-packet equivalent of the velocity oscillations, and in turn reproduce the velocity profiles via the Biot-Savart law. The ODT eddies also are internal to the flow field deriving energy from the velocity profiles via their gradients and, in turn, inducing velocity changes.

The fundamental connection between the eddy frequency and the velocity profiles evident in ODT resembles the turbulent kinetic energy production term in RANS models. The inverse relation between eddy frequency and the distance of their centres from the wall in AEM is a specialized case of the ODT approach, where high velocity gradients close to the wall produce same effect as AEM. The downside with ODT lies chiefly in the incomplete representation of the three-dimensional eddy geometries.

Chapter 6

Predicting the hypersonic turbulent boundary layers with one-dimensional turbulence

Associated reference:

Nath, Pranav and Hickey, Jean-Pierre, “Predicting the hypersonic turbulent boundary layers with one-dimensional turbulence”, under revision in *Physical Review Fluids*.

Abstract

The scaling laws for the hypersonic turbulent boundary layer flows are assessed against a limited set of DNS available in the open literature. The computational expense of the DNS limits both Reynolds number and wall-to-recovery temperature ratios, which impacts the ability to generalize the scalings to extreme hypersonic conditions. In this work, we explore a reduced-dimensionality model, the one-dimensional turbulence (ODT), and develop a computationally tractable tool that can provide DNS-like near-wall statistics at a fraction of the computational cost. Unlike other modelling paradigms, ODT does not rely on classical RANS-based assumptions or on an assumed turbulent Prandtl number Pr_t . Instead, ODT is a stochastic tool that models the effects of the three-dimensional

eddies on the one-dimensional domain. This work explores the model parameters under diabatic turbulent boundary layer conditions and validates the statistics against published results at $M \approx 5.86$. Statistical sampling of ODT is shown to provide a quantification of the wall temperature and pressure probability distribution.

6.1 Introduction

The hypersonic non-adiabatic turbulent boundary layers (TBL), in a time-averaged sense, is characterized by a large mean flow temperature gradient, which strongly impacts the local viscosity and contributes to the shear stresses near the wall. The mean flow TBL quantities are important as they inform drag and aerothermal heat transfer necessary for the design of aerodynamic control and thermal protection systems. However, further characterization of the near-wall turbulence is critical as it is the strongly intermittent temperature, pressure, and shear stress fluctuations, often caused by the coherent structures in the boundary layer [98], that drive ablation [191], fluid-structure interactions [17], local dissociation and chemical kinetics [114, 34, 110]. Although these fluctuating quantities can be either modeled or even inferred, the characterization of the probability distribution and the frequency of occurrence of these extreme events in highly-cooled, hypersonic turbulent boundary layers demands careful consideration for predictive modelling.

The mean streamwise velocity profile in the cooled hypersonic TBL can be estimated, to a good degree, using the RANS model; a turbulence modelling strategy which remains the favored approach for industrial, high-speed CFD. Although the RANS turbulence models have been tuned to the specificities of hypersonic flows, they must rely on strong modelling assumptions to characterize the turbulent heat transfer [138]. In classical CFD modelling approaches, a constant turbulent Prandtl number, Pr_t , relates the turbulent momentum transport to turbulent heat transport. This convenient simplification is known to be problematic near the wall. Some works have proposed a variable Pr_t [182, 147, 128], but with these more complex modelling approaches, the user is faced with the conundrum of trading robustness and resilience of the model for a slightly more accurate heat transfer approxi-

mation. Furthermore, the strong thermodynamic non-linearities near the wall induce some errors in incorrectly accounting for the fluctuating component of the molecular viscosity, which is often lumped in with the mean field closure. Thus, although RANS provides an invaluable approximation, its limitations are reached due to the modelling assumptions. RANS exhibits an inability to deal with strong thermodynamic non-linearities, and to fully characterize the frequency of occurrence and probability distribution of extreme near-wall turbulent events which is necessary in hypersonic turbulent flows.

DNS of high-enthalpy TBL at hypersonic conditions is a valuable tool to assess the state of turbulence at the wall [107, 108, 35, 31, 32, 89, 137, 192]. The large computational expense of DNS precludes its use for applied hypersonic configurations but provides the ability to generate a database to quantify near-wall turbulence and help develop TBL scaling laws to address the challenges at highly cooled conditions. Trettel and Larsson [171] observed that the viscosity variation arising in high-speed flow explains the slight discrepancy observed in the van Driest scaling, which motivated a series of works to correct the near-wall velocity [51, 190, 23, 22] and temperature [24] scaling for highly cooled hypersonic boundary layers. These new scalings are critical towards the improvement of wall-modeled LES at hypersonics conditions. The generalizability of these scaling laws is limited by the relatively low Reynolds number of DNS and the extent of the existing DNS database in covering the relevant conditions—especially at low wall temperature. High-enthalpy experimental measurements, ground-based or in flight, present the best opportunity to characterize the turbulent quantities of interest but face the concurrent difficulty of combining an extremely high temporal resolution with the need to sample over a large measurement window to characterize extreme near-wall events.

A more extensive database of canonical cooled-wall hypersonic TBL is needed to improve existing RANS models, extend the generalizability of the scaling laws, and better characterize the frequency of near-wall turbulent events. In this context, we explore a reduced-dimensionality model as an alternative to the expensive DNS simulations to model the hypersonic TBL. The ODT model, proposed in the seminal work by Kerstein [78] and further developed since work by Refs. [6, 95], provides a computationally tractable alternative to DNS that is based on a number of modelling assumptions that need to be assessed for

hypersonic conditions. The ODT approach considers a one-dimensional domain normal to the wall and uses stochastic linear eddies to represent the effect of three-dimensional turbulence on the one-dimensional line. Incompressible wall turbulence was extensively studied with ODT by Kerstein [78], where only the streamwise-velocity component was considered; this was followed by the inclusion of transverse-velocity components in Ashurst and Kerstein [6]. ODT has been shown to capture the salient features of incompressible TBL in temporally [139] and spatially [140] developing boundary layers. Recent work by Nath and Hickey [121] has shown inherent similarities between the Attached Eddy Model and ODT; thus, further support the use of the approach for high-Reynolds number boundary layers. Jozefik *et al.* [73] used a pseudo-compressible solver in ODT to study the RM instability. Chen *et al.* [20] developed a Eulerian-based ODT approach of the compressible NS equations and validated their findings on high-Reynolds number compressible channel flow. To address some of the shortcomings of previous ODT formulations and explore the use of these models in highly cooled, hypersonic TBL, we developed a fully compressible fluid model in a Eulerian reference frame [122], coupled with the stochastic turbulence model of ODT. The current work provides a compressive assessment of ODT under relevant hypersonic conditions with a complete characterization of velocity and thermal profiles and near wall statistics. Once validated, the ODT framework can be used to generate a large dataset of hypersonic TBL that can be used to generalize wall scalings and improvement of RANS models at these extreme conditions.

In this work, we compute compressible TBL profiles up to $Re_\tau \approx 1221$ and Mach number $M \approx 6$, with wall-to-recovery temperature ratios: $T_w/T_r = 0.73, 0.45$ and 0.26 . The methodology for the compressible ODT formulation is first described, followed by a description of the simulations. The mean velocity and mean temperature profiles obtained by the current model, accompanied by Reynolds shear and normal stresses for the two cases of T_w/T_r are then provided. The obtained mean velocity and temperature profiles, along with the Reynolds stresses, are shown to align well with the comparative DNS results. Subsequently, the results pertaining to the energy transport and statistics of the thermal properties are described.

6.2 Model formulation

6.2.1 Governing equations

We model a high-Mach number, zero-pressure gradient, cooled-wall turbulent boundary layer flow using ODT. The ODT approach allows for a full resolution of all relevant spatial and temporal scales along a single dimension in the TBL. The one-dimensional domain is oriented normal to a non-slip moving wall and is bounded, far in the freestream, by a fixed, non-slip wall. The ODT approach solves the compressible form of the NS equations and utilizes a multiscale sequence of triplet mappings that stochastically represent the mechanistic behaviour of three-dimensional eddies acting along the one-dimensional domain. In this work, the conservation equations for mass, momentum and energy, closed with the ideal gas equation, are solved in a fully Eulerian framework, unlike the original Lagrangian formulation of ODT [78, 6].

The ODT domain is aligned along the spatial direction z , while x is along the streamwise direction and y is in the spanwise direction. The variable u_i represents the i^{th} velocity component, where the indices $i = 1, 2$ and 3 refer to the components along the x, y and z directions, respectively. The terms ρ, P, E represent the density, pressure, and total energy (sum of internal and kinetic energy: $E = e + 1/2(u_1^2 + u_2^2 + u_3^2)$), respectively. We use the conservative form of the NS equations with variables $\rho, \rho u_i$ ($i = 1, 2, 3$), and ρE , while neglecting the derivatives normal to the ODT domain:

$$\begin{aligned} \frac{\partial \rho}{\partial t} + \frac{\partial(\rho u_3)}{\partial z} &= 0, \\ \frac{\partial(\rho u_i)}{\partial t} + \frac{\partial(\rho u_i u_3)}{\partial z} &= -\frac{\partial P}{\partial z} \delta_{3i} + \frac{\partial \sigma_{i3}}{\partial z}, \\ \frac{\partial(\rho E)}{\partial t} + \frac{\partial(\rho E u_3)}{\partial z} &= -\frac{\partial(P u_3)}{\partial z} - \frac{\partial q_3}{\partial z} + \frac{\partial u_i \sigma_{i3}}{\partial z} \end{aligned} \quad (6.1)$$

Assuming the flow to be Newtonian, the simplified deviatoric stress components are computed in a truncated form as:

$$\sigma_{13} = \mu \frac{\partial u_1}{\partial z}, \quad \sigma_{23} = \mu \frac{\partial u_2}{\partial z}, \quad \text{and} \quad \sigma_{33} = 2\mu \frac{\partial u_3}{\partial z} + \lambda_s \frac{\partial u_3}{\partial z}, \quad (6.2)$$

where μ is the dynamic viscosity and λ_s is the second viscosity coefficient. The variation in μ with temperature, T , is given by a power law, $\mu \sim T^{3/4}$, and the second coefficient of viscosity is given by $\lambda_s(T) = -2/3 \mu(T)$. The heat flux, q_3 , is modeled using Fourier's law:

$$q_3 = -k_t \frac{\partial T}{\partial z}, \quad (6.3)$$

where k_t is the thermal conductivity.

The numerical implementation of the flow solver uses the WENO 5th order scheme in conjunction with the HLLC solver, as described in Houim and Kuo [55]. The time integration is done using a third-order Runge-Kutta scheme, and the time step is acoustically constrained using the obtained maximum values of the instantaneous flow velocity and sound speed. The current implementation is a modification of the formulation presented earlier in Nath and Hickey [122], which is an extended version of the open-source code originally developed by Stephens and Lignell [169]. An adaptive meshing scheme is used that refines the grid in the near-wall regions of higher gradients.

6.2.2 Turbulence model

Stochastic eddy using triplet-map

The turbulence model in the ODT approach employs stochastic one-dimensional eddies that represent the action of three-dimensional turbulence on the one-dimensional domain. The stochastic one-dimensional eddies were first introduced by Kerstein [77], and then later adopted in the seminal work describing the ODT method [78]. The one-dimensional (linear) eddies produce the energy cascade by transferring energy from the larger to the smaller scales via certain transformations in the flow properties. These transformations are stochastically carried out at sampled locations with an associated length and time scale of the turbulent eddies, using the predefined mapping known as the triplet mapping. The mapping is measure-preserving, and introduces higher wavenumbers in the domain without introducing any jump discontinuities. In the present formulation, the conservative

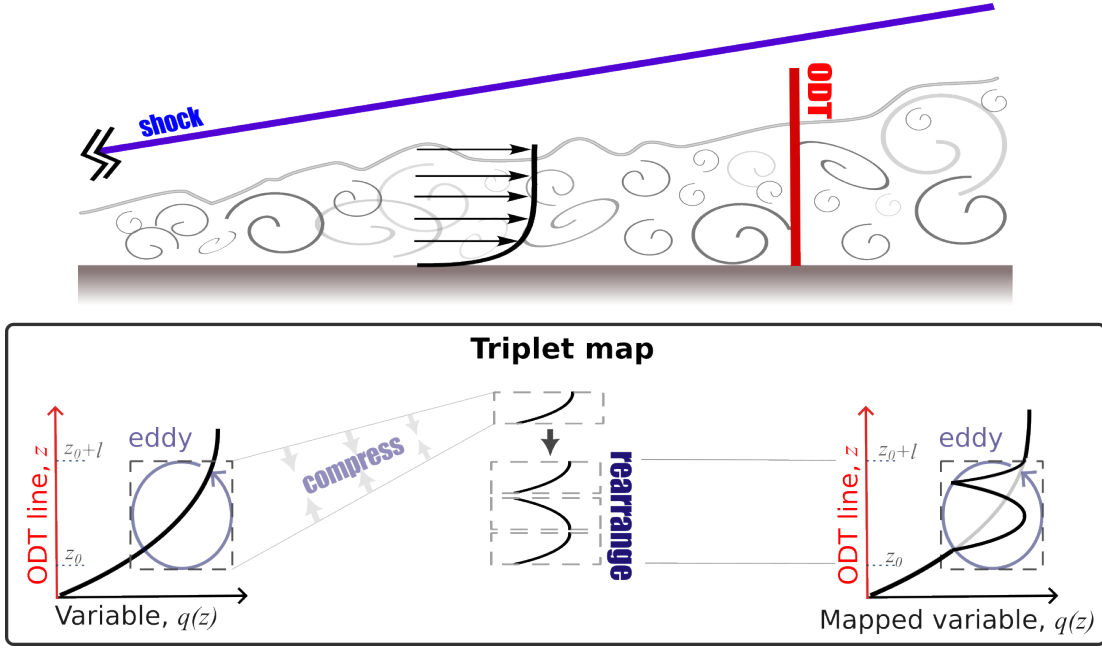


Figure 6.1: Conceptual illustration of the ODT domain in a turbulent boundary layer (top) and the representation of the triplet-map applied to the variable $q(z)$.

variables undergo triplet mapping, which is given as:

$$f(z) = z_o + \begin{cases} 3(z - z_o), & z_o \leq z \leq z_o + \frac{1}{3}l \\ 2l - 3(z - z_o), & z_o + \frac{1}{3}l \leq z \leq z_o + \frac{2}{3}l \\ 3(z - z_o) - 2l, & z_o + \frac{2}{3}l \leq z \leq z_o + l \\ z - z_o. & \text{otherwise} \end{cases} \quad (6.4)$$

Here, z_o and l are the start location and length of the eddy, respectively. In the region where the eddy is applied, three copies of the variable profile $q(z)$ are made, compressed, the middle copy is inverted, and then the three segments are stitched together, see figure 6.1. The displacement induced by the eddy is defined using a kernel function $K(z) = f(z) - z$, which integrates to zero over the eddy region by definition.

The original ODT formulation of Kerstein [78] considered a single velocity component; however, the later formulation in Ashurst and Kerstein [6] accounted for pressure-

scrambling effects while incorporating all the three velocity components. The pressure-scrambling causes a return-to-isotropy and, to model this effect in ODT, the available energy is redistributed among the velocity components using a transformation subsequent to the triplet mapping. Even though this energy transfer among the velocity components is energy-conserving, the momentum along each coordinate is not necessarily conserved, and an additional term is added to the post-triplet-map velocity transformation to ensure momentum conservation. Section 3.1.4 describes an energy balance during the post-triplet-map energy redistribution and associates a kinetic energy to the eddy per unit cross-sectional area of the ODT domain, given by E_{kin} .

Time scale associated with the eddies

The eddy time scale, τ , is a physical parameter dependent on the instantaneous state of the system over the region impacted by the eddy and changes as the system evolves.

The scaling of the eddy kinetic energy, $1/2m(l/\tau)^2$, helps to define the eddy-time scale, where m is the mass of the fluid inside the region impacted by the eddy and l/τ is the eddy-velocity scale. The mass can be expressed as $m = \langle \rho \rangle l A_c$, where $\langle \rho \rangle$ refers to the average density of the affected domain volume. The affected domain volume is given as $l A_c$, where A_c is a notional cross-sectional area normal to the one-dimensional ODT domain. The average density $\langle \rho \rangle$ is expressed as $\langle \rho \rangle = \rho_{KK} / KK$, where $KK = \int_{z_o}^{z_o+l} K^2(z) dz$ and $\rho_{KK} = \int_{z_o}^{z_o+l} \rho(z) K^2(z) dz$. Using the introduced definitions, the scaling for the eddy-kinetic energy per unit A_c is given as:

$$E_{kin} = \frac{1}{2} m \cdot u^2 \frac{1}{A_c} \approx \frac{1}{2} \langle \rho \rangle \frac{(l A_c)}{A_c} \frac{l^2}{\tau^2} = \frac{1}{2} \frac{\rho_{KK}}{KK} \frac{l^3}{\tau^2}. \quad (6.5)$$

Introducing the notation $\tau(z_o, l; t)$ for the time-scale of an eddy that occurs at an instant of time t , with start location z_o and length l , and rearranging equation (6.5) gives:

$$\frac{1}{\tau(z_o, l; t)} \approx \sqrt{\frac{2KK}{\rho_{KK} l^3} E_{kin}}. \quad (6.6)$$

where, E_{kin} is a measure of the kinetic energy as described in Sect. 3.1.4.

Previous ODT approaches typically subtract a viscous penalty E_{vp} from the term E_{kin} that sets the lower limit on the allowable eddy size [6]. Although E_{vp} affects the eddy selection criterion, it does not have an impact on the nature of the transformation by the eddy. The viscous penalty introduces a second mechanism of viscous dissipation, adding to the diffusive effects of the viscous terms in the governing equations.

$$\frac{1}{\tau(z_o, l; t)} = \sqrt{\frac{2KK}{\rho_{KK}l^3}(E_{kin} - ZE_{vp})}. \quad (6.7)$$

The viscous penalty is defined as $E_{vp} = \mu_{eddy}^2 / (2\rho_{eddy}l)$, where, ρ_{eddy} represents the average density of the flow and μ_{eddy} is the average dynamic viscosity, computed within the eddy region. A viscous penalty parameter Z is introduced to scale the viscous penalty term.

A potential energy term E_{pe} is often added to E_{kin} term in the ODT formulation to model the effect of other forces involved in the system, for example, the effects of unsteady dilatation and shock-turbulence interaction. However, the term is ignored in this work due to the absence of external forcing mechanisms.

Eddy occurrence rate

In ODT, each eddy is considered as an instantaneous event, and these eddies are sequentially invoked at a controlled rate. The rate of occurrence of eddies in the parameter range $z_o \in [z, z + dz]$ and $l \in [l, l + dl]$ at an instant of time t , can be expressed as $\lambda_r(z_o, l; t)dz_o dl$, where the eddy rate distribution $\lambda_r(z_o, l; t)$ is given as:

$$\lambda_r(z_o, l; t) = \frac{1}{l^2\tau(z_o, l; t)}. \quad (6.8)$$

Integrating $\lambda_r(z_o, l; t)dz_o dl$ over the entire parameter space for eddy start location (z_o) and size (l) gives the overall eddy rate:

$$\Lambda(t) = \int_{z_o} \int_l \lambda_r(z_o, l; t)dz_o dl \quad (6.9)$$

The ratio $\lambda_r(z_o, l; t)/\Lambda(t)$ gives the instantaneous joint probability density function for the occurrence of eddy with start location z_o and size l , and has direct dependence on the eddy time-scale $\tau(z_o, l; t)$.

In principle, the eddies could be sampled via a discrete Poisson process at the rate $\Lambda(t)$, depending on the instantaneous system state, and the admittance of the eddy could be tested based on the joint PDF given by $\lambda_r(z_o, l; t)/\Lambda(t)$. However, continually reevaluating $\Lambda(t)$ and $\tau(z_o, l; t)$ at each time-varying frozen flow state is too computationally expensive and the probability of the considered eddy is factored into two *guessed* probability distributions, $g_1(z_o)$ and $g_2(l)$, for eddy start locations and sizes, respectively.

We use a uniform distribution for the eddy start location, $g_1(z_o)$, along with the preset distribution for eddy size in Stephens and Lignell [169] with $s = 1$, $g_2(l)$:

$$g_2(l) = \frac{c_1}{l^{s+1}} \exp\left(-\frac{c_2}{l^s}\right). \quad (6.10)$$

Here, the parameters c_1 and c_2 are set to approximately achieve the desired flow-specific eddy-size distribution. The guessed distributions g_1 and g_2 have a negligible influence on the simulation results.

The sampled eddy is then subject to an acceptance-rejection method based on the probability:

$$p_e = \frac{C\Delta t_e}{l^2 g_1(z_o) g_2(l) \tau}, \quad (6.11)$$

where, the parameter C is an ODT parameter used to modify the turbulence intensity. Δt_e is the mean time interval for eddy sampling, which is usually chosen to be small enough so that the eddies are sampled at a rate much higher than the prescribed rate $\Lambda(t)$. The discrete sampling of eddies followed by the acceptance-rejection procedure produces the physically prescribed ensemble of eddies.

6.2.3 Set-up of the ODT simulation domain

In this work, a turbulent boundary layer is created by inducing a flow of air with molecular mass ($M = 28.96 \text{ g/mol}$) between two infinite parallel plates by moving one of the plates at high speeds ($M \geq 5$). The approach is similar to the incompressible regime ODT simulations of Rakhi *et al.* [139]. The considered setup was found to be beneficial to model a zero-pressure gradient boundary layer in the ODT framework, as opposed to

the approach used in Chen *et al.* [20], wherein the pressure-gradient-driven channel flow profiles are utilized to infer characteristics of the turbulent boundary layers. The separation between the plates is large enough so that a significant fraction of the flow close to the fixed plate does not experience any eddy-induced disturbances, and the velocity gradient at the fixed wall is zero. The variation of Reynolds stresses in Sect. 4.3 reveals that the fixed domain length adequately accommodates the turbulent boundary layer as the turbulent shear stress drops to zero at less than half the domain length.

The one-dimensional ODT domain extends from $z = 0$ at the moving plate all the way to the fixed plate. Dirichlet boundary conditions for the velocity components and the temperature are set at both ends of the domain. The plate at $z = 0$ is set at the desired wall temperature (T_A) and moves at a velocity $u_1 = u_{wall}$ along the streamwise direction, with zero u_2 and u_3 velocity components at the plate location. The fixed plate, at the other end, is held stationary with all velocity components set to zero, and temperature set as T_B , the freestream temperature.

6.3 Results

The results obtained from the simulations are transformed to represent the characteristics of the turbulent boundary layer developed by the zero-pressure gradient driven flow at a freestream Mach number (M_∞) over a fixed flat plate at $z = 0$. A Galilean transformation is performed by subtracting the streamwise velocity of the moving plate (u_{wall}) from the entire domain. The remaining properties such as temperature, density, pressure, and other velocity components remain unchanged. The freestream Mach number is set using $M_\infty = u_{wall}/c_\infty$, where c_∞ is the speed of sound in the freestream. The results presented henceforth have undergone the mentioned transformation and can be directly compared to the DNS studies of turbulent boundary layers over stationary flat plates.

<i>Case</i>	Re_τ	C	Z	M_∞	T_w/T_r	δ_ν (10^{-5})	U_τ (ms^{-1})	M_τ
I	401	10	100	5.97	0.734	5.0	38.4	0.111
II	497	15	100	5.97	0.733	4.4	43.3	0.125
III	517	20	100	5.96	0.737	4.3	45.0	0.130
IV	548	25	100	5.94	0.738	4.0	47.8	0.138
V	560	20	50	5.96	0.734	4.1	46.6	0.135
VI	495	20	200	5.96	0.734	4.4	43.1	0.125
VII	426	20	300	5.93	0.740	4.3	44.3	0.128

Table 6.1: List of cases of compressible TBL in the present study with a domain length $L = 0.05$, $L_{min} = 1.5 \times 10^{-5}$ and $T_w/T_r \approx 0.73$.

6.3.1 Mean-statistics obtained at $T_w/T_r \approx 0.73$

Table 6.1 provides the parameters and results for an initial set of simulations, in which the parameters C and Z , from Eqs. (6.11) and (6.7), are systematically varied. Figures 6.2 and 6.3 provide the profiles for mean velocity, mean temperature, Reynolds shear and normal stresses for the various ODT parameters. The domain length is given by L and the minimum allowable eddy size is L_{min} . Here, the wall-to-recovery temperature ratio is defined as T_w/T_r , where the recovery temperature is $T_r = T_\infty(1 + 0.89((\gamma - 1)/2)M_\infty^2)$. The mean velocity profile is presented after being subjected to the van Driest transformation:

$$\langle u_1 \rangle_{VD}/U_\tau = \frac{1}{U_\tau} \int_0^{\langle u_1 \rangle} \sqrt{\langle \rho \rangle / \langle \rho_{wall} \rangle} d\langle u_1 \rangle \quad (6.12)$$

The transformations introduced in Refs. [171, 190, 24] could also be used to compare the present results with DNS, however, we restrict the comparisons to van Driest transformed velocity profile as this transformation was reported in comparative DNS studies.

The Reynolds normal stresses are directly computed from time averaging the instantaneous streamwise velocity and are normalized by the friction velocity U_τ . On the contrary, Reynolds shear stress are not directly given by the cross-correlation of the fluctuating velocity components u'_1 and u'_3 , and an indirect approach is used. Ensemble averaging of the

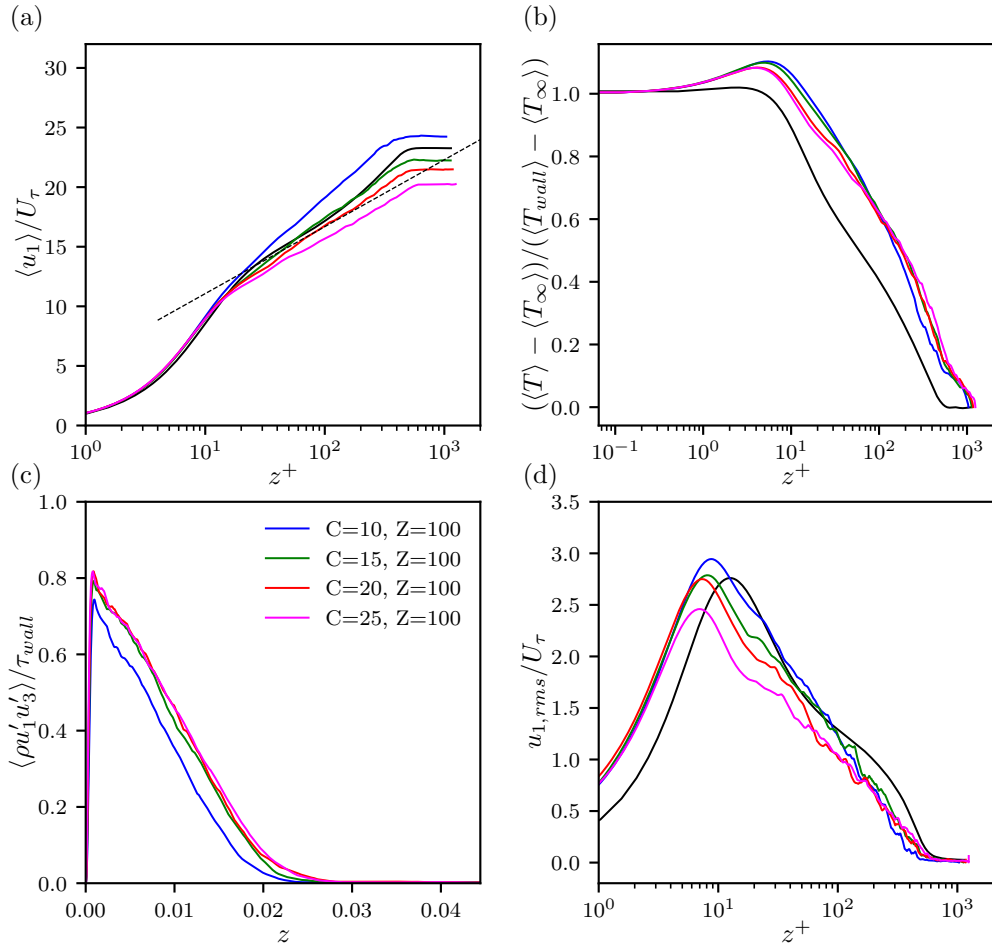


Figure 6.2: Comparison of ODT simulations with different C parameters at $T_w/T_\tau \approx 0.73$. The DNS results from Zhang *et al.* [192] are shown in solid black and the dashed line in (a) corresponds to the von Kármán's law of the wall.

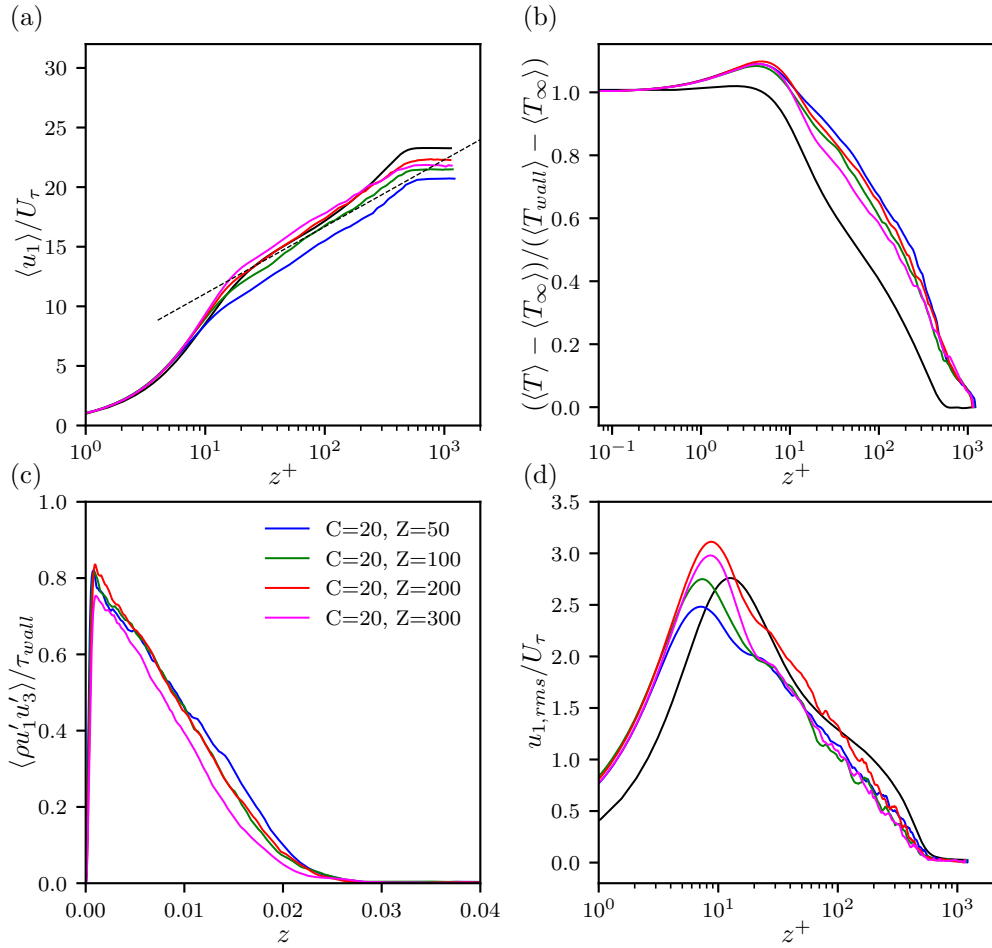


Figure 6.3: Comparison of ODT simulations with different Z parameters at $T_w/T_r \approx 0.73$. The DNS results from Zhang *et al.* [192] are shown in solid black and the dashed line in (a) corresponds to the von Kármán's law of the wall.

eddy-induced transport of velocity components through the mapping procedure over time yields an estimate of Reynolds shear stress. A control volume analysis shows that $\langle \rho u'_1 u'_3 \rangle$ represents the ensemble averaged net advective flux of streamwise momentum $\langle \rho u'_1 \rangle$ across a given wall-normal position z [78, 80]. The evaluation of $\langle \rho u'_1 u'_3 \rangle$ comprises of two steps: **(i)** compute the net rate of transfer of the streamwise momentum induced by the ODT eddies at a wall-normal location z^* , given by $\Delta \rho u_1(z^*)$, and **(ii)** Integration of $\Delta \rho u_1(z^*)$ from the wall ($z = 0$) to the location z .

The values of C and Z suitable for a close match with the DNS profiles differ from other studies, which is expected as the result of different TBL configurations, boundary layer thicknesses and flow physics in the current compressible formulation. The values of C and Z have a compound effect on the mean profiles, as observed in the results of Rakhi and Schmidt [139]. Increasing the value of C causes increased turbulent mixing in the logarithmic region, lowering the slope of the mean velocity profile. On the other hand, increasing the Z parameter keeps the slope of the mean-velocity profile virtually unaffected in the log region, and causes an increase in the $\langle u_1 \rangle / U_\tau$ profile uniformly across z . The predominant increase in $\langle u_1 \rangle / U_\tau$ occurs due to a reduction in U_τ with increasing Z , as evident from Table 6.1.

A notable observation is the significant improvement in the obtained streamwise Reynolds normal stresses $u_{1,rms}$ as compared to earlier ODT studies. The ODT profiles for Reynolds normal stresses were consistently reported to be underpredicted by previous ODT studies [139, 140] compared to DNS results. However, the current work with a compressible formulation shows a close match with DNS in terms of the shape and values of the streamwise Reynolds normal stresses. The other components of Reynolds stresses show subnominal values due to inadequate three-dimensional effects in ODT and have been omitted as they are not critical in the near-wall dynamics.

<i>Case</i>	Re_τ	L_{min} (10^{-6})	M_∞	T_w/T_r	δ_ν (10^{-6})	U_τ (ms^{-1})	M_τ
I	497	15	5.97	0.733	44.0	43.3	0.125
II	844	7.5	5.80	0.449	18.9	38.3	0.145
III	1221	3.0	5.81	0.260	7.4	36.6	0.184

Table 6.2: List of cases of compressible TBL in the present study with a domain length $L = 0.05$.

6.3.2 Prediction of compressible TBL profiles in flows over cold-walls

The compressible formulation of the current work allows ODT simulations at extreme scenarios of practical importance at a fraction of the computational cost of DNS. We tested the performance of the developed model at low values of T_w/T_r , which are often encountered in the TBL in hypersonic applications. The ODT parameters that give the closest match to the DNS results at $T_w/T_r \approx 0.73$ (from Sec. 6.3.1) are tested for their applicability to the case with cold walls ($T_w/T_r \approx 0.26, 0.45$).

The low wall temperature significantly impacts the computational cost. Since low wall temperature causes reduced dynamic viscosity, the viscous wall unit δ_ν is considerably lower. The reduction of δ_ν demands increased resolution close to the wall, which could be, in principle, achievable without a drastic increase in grid count by reducing the overall size of the domain. However, to maintain consistency across different ODT simulations with respect to the ODT parameters, we preserve the domain size in the cases with $T_w/T_r \approx 0.73$. The minimum allowable eddy size L_{min} is reduced when T_w/T_r is reduced; see Table 6.2.

Table 6.2 gives simulation results for three cases of compressible cold wall TBL, and figure 6.4 shows the corresponding profiles of important properties. The velocity profiles exhibit a linear region in the log layer, with slope consistent with the von Kármán’s theoretical solution, an expected result given the previously explained similarities with the Townsend’s Attached Eddy Model in the TBL [121]. The profiles in log-regions show a shallower slope with a lower T_w/T_r ratio, which can be counteracted by a slight reduction

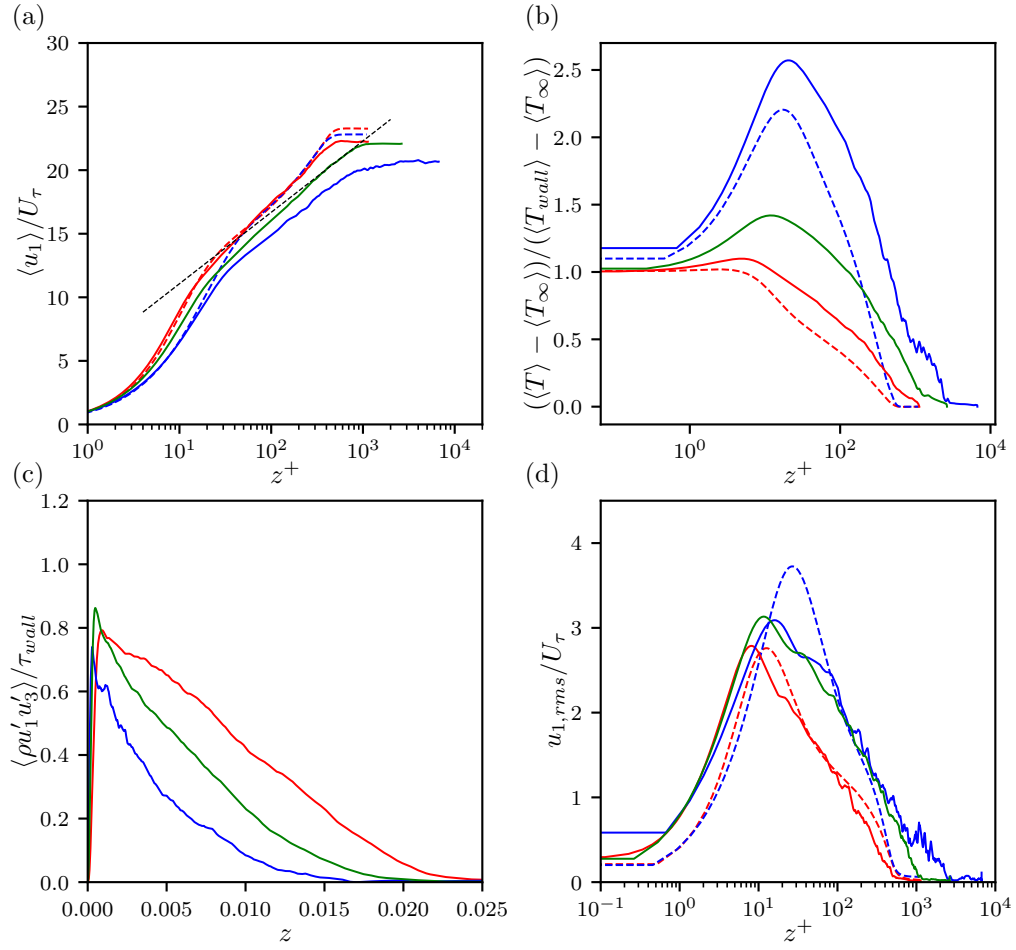


Figure 6.4: Comparison of ODT simulation results at Tw/Tr values of 0.26 (blue), 0.45 (green) and 0.73 (red) in solid lines with $C = 15$ and $Z = 100$. The DNS results from Zhang *et al.* [192] are shown in dashed lines with Tw/Tr values of 0.25 (blue) and 0.75 (red). The black dashed line in (a) corresponds to the von Kármán's law of the wall.

in the C parameter to achieve an exact match with the DNS profiles. The characteristic peak in the temperature profile observed in the DNS results at $z^+ \approx 20$ is captured with the developed formulation. As observed in the results at $T_w/T_r \approx 0.73$, the cold-wall cases with T_w/T_r of 0.26 and 0.45 exhibit a close match of the Reynolds normal stresses with the DNS results (see figure 6.4(d)).

The limitation of ODT simulations is approached as T_w/T_r is further reduced. Very low T_w/T_r is accompanied by a significantly reduced viscosity in proximity to the wall, which leads to extremely fine resolution requirement. Refined resolution leads to smaller eddies being accepted, and the extremely small eddies introduce massive velocity gradients after the triple-mappings. The large-gradient post-map energy and velocity profiles in such cases, coupled with the numerical diffusion and stochastic variations, intermittently introduce unphysical values of pressure via negative internal energy, e . Hence, we restrict T_w/T_r of the simulations to a lower limit of $T_w/T_r \approx 0.25$.

6.3.3 Turbulent energy transport

The developed model allows the investigation of the role of turbulence in heat and mass transport in the hypersonic TBL. The momentum and heat transfer induced by the eddies can be computed by comparing the streamwise velocity and temperature profiles, respectively, before and after the eddy occurrences.

The production rate of turbulent kinetic energy (TKE) is calculated using the product of shear Reynolds stresses $\langle \rho u'_1 u'_3 \rangle$, calculated as shown in Sec. 6.3.1, with the mean streamwise velocity gradient $d\langle u_1 \rangle/dz$. Figure 6.5 shows the TKE production rate normalized by the quantity $\langle \rho_{wall} \rangle^2 U_\tau^4 / \mu_{wall}$. Normalized production rate profiles exhibit a collapse with the maximum production rate located at approximately $z^+ = 10$.

An important quantity that relates the turbulent transfer of momentum to that of heat is the turbulent Prandtl number, Pr_t , which is defined using:

$$Pr_t = \left(\frac{\langle -u'_1 u'_3 \rangle}{\partial \langle u_1 \rangle / \partial z} \right) \left(\frac{\partial \langle T \rangle / \partial z}{\langle -T' u'_3 \rangle} \right). \quad (6.13)$$

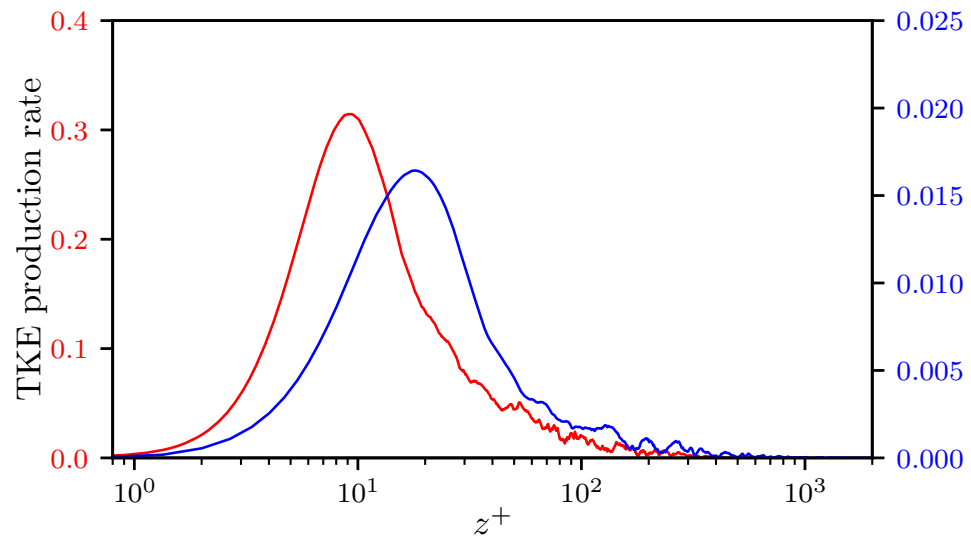


Figure 6.5: Variation of normalized TKE production rate with wall-normal distance for $T_w/T_r \approx 0.26$ (blue) and 0.73 (red).

RANS models heavily rely on the set value of the turbulent Prandtl number (Pr_t) to relate turbulent heat diffusion to turbulent mass diffusion. In contrast, in ODT, the instantaneous flow statistics can be used to directly compute Pr_t as an output of the simulations since the linear eddies physically represent transport of heat and momentum due to the fluid turbulence.

The Pr_t profiles converge to Pr_t 0.9 at the wall, which is slightly higher than the DNS just above the wall [192] but similar to what has been reported in the RANS modelling literature [58], see figure 6.6. However, the ODT simulations show larger oscillations in Pr_t with a higher mean as the outer region of the boundary layer approaches, similar to the DNS of Zhang *et al.* [192] but showing a discrepancy from Huang *et al.* [57]. The increased oscillations can be attributed to the combined effect of an insufficient number of eddies in the freestream and the turbulent transport term in the denominator $\langle -T'u'_3 \rangle$, tending towards zero in the freestream. However, individual ODT eddies singularly represent the physical transport of momentum and heat using the same underlying mapping process. The commonality of the mechanism for turbulent transport of momentum and heat, and a significant number of eddies close to the wall, lead to the Pr_t being just below unity on the wall.

6.3.4 Statistics of fluctuating thermodynamic quantities

RANS models provide averaged flow quantities; however, practical applications often require realistic estimates of the fluctuating quantities, for example, instantaneous temperature wall normal profiles. The fluctuation in temperature profiles causes large oscillations in the instantaneous heat transfer to the wall. The current model provides a framework to quantify these fluctuations, owing to the absence of time averaging in the governing equations. The probability distribution functions (PDFs) of the instantaneous temperature and temperature gradients are shown in Figs. 6.7 and 6.8, respectively. The PDFs have been normalized using the standard deviation at each wall normal location and the mean quantities have been subtracted from the abscissa coordinates. The PDFs are not Gaussian and show an inherent bias towards negative or positive values as a function of

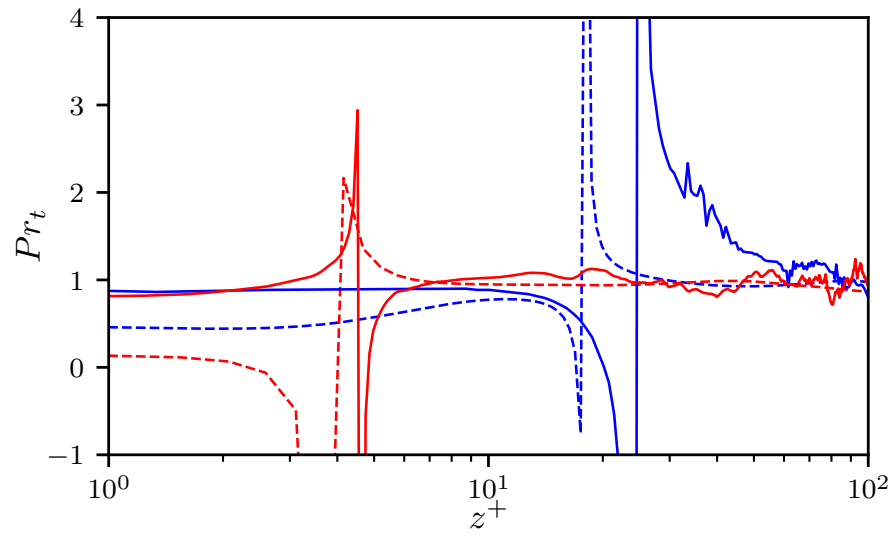


Figure 6.6: Variation of Pr_t with wall-normal distance, where the dashed black line shows $Pr_t = 1$. The colored lines are the ODT results (solid) and DNS (dashed) results from Zhang *et al.* [192], for $T_w/T_r = 0.26$ (blue) and 0.73 (red).

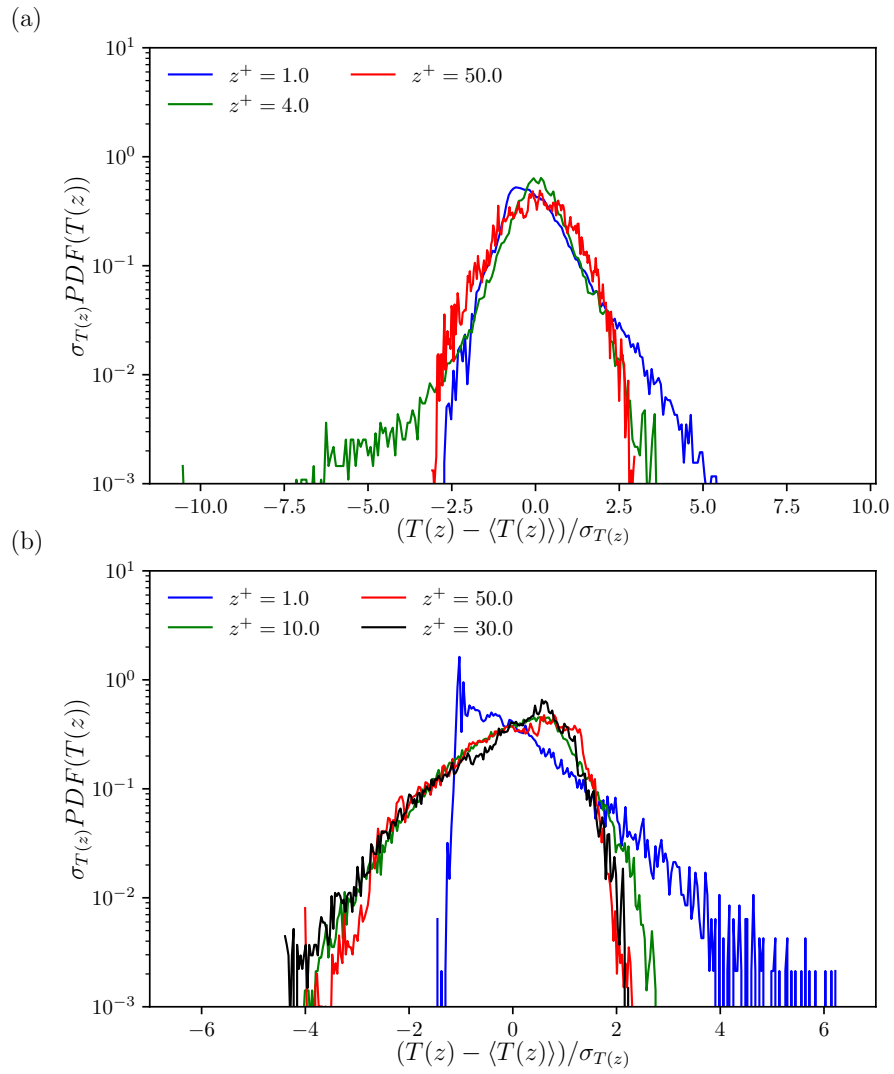


Figure 6.7: Normalized probability distribution function of $T(z)$ for (a) $Tw/Tr \approx 0.73$ and (b) $Tw/Tr \approx 0.26$.

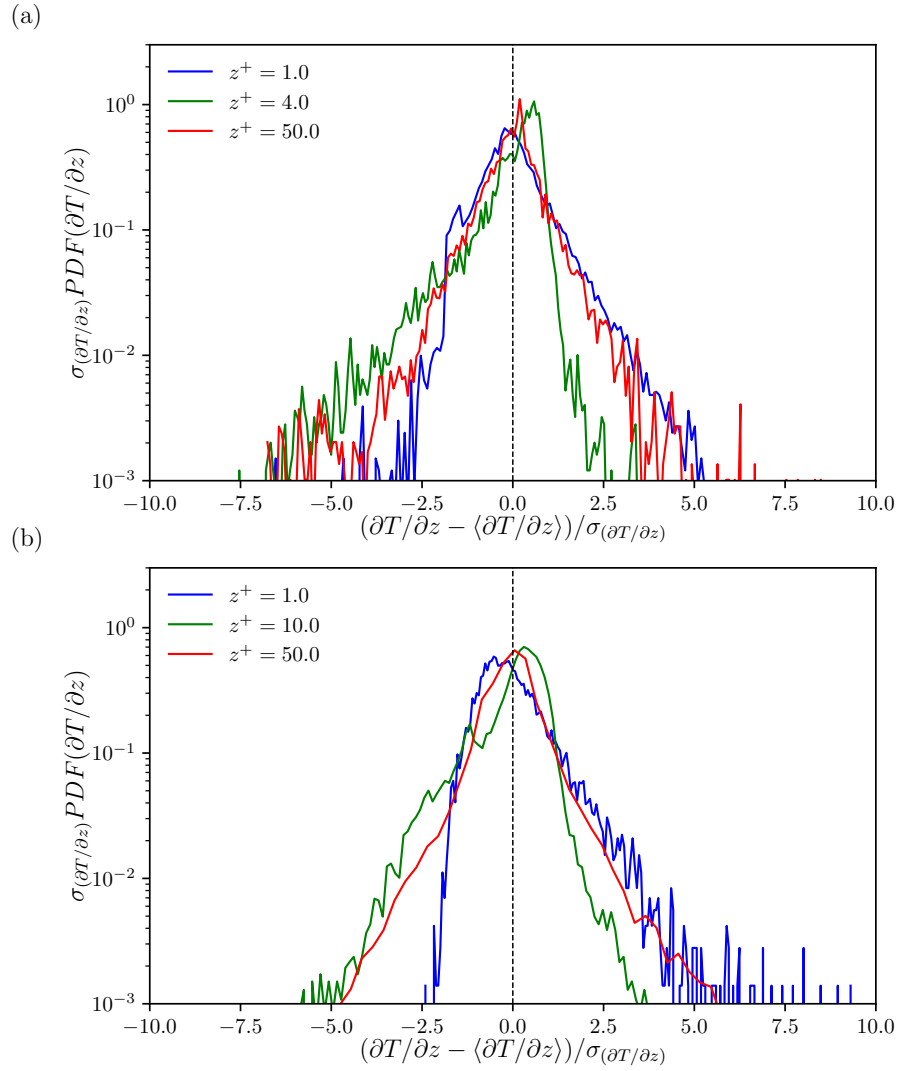


Figure 6.8: Normalized probability distribution function of dT/dz for (a) $Tw/Tr \approx 0.73$ and (b) $Tw/Tr \approx 0.26$.

wall-normal distances. Closest to the wall location ($z^+ = 1$), the temperature gradients exhibit a skewed distribution with higher occurrences of positive values ($\partial T/\partial z > \langle \partial T/\partial z \rangle$), with a reversal in the trend slightly further away from the wall (shown in green). The PDFs become symmetric higher up in the boundary layer. A similar skewness is seen in the normalized PDFs of $T(z)$, with the same nature of asymmetry as seen in temperature-gradient PDFs. However, the cold-wall cases ($T_w/T_r = 0.26$) exhibit sharp distortions even up to $z^+ = 50$.

Fluctuations in wall pressure induced by turbulence can cause significant structural loads in hypersonic vehicles, and quantifying them has been a focus of several DNS studies [9, 33] in the context of hypersonic TBL. Stack and Wagnild [168] uses a wall-modeled LES to study wall pressure fluctuations with hypersonic flow over a sharp cone. The pressure fluctuation spectra close to the wall are computed from the pressure oscillations measured in the current model, and comparisons are made with the analytical Liepmann model [93], see figure 6.9. The spectra for both cases: $T_w/T_r = 0.73$ and $T_w/T_r = 0.26$, show a match with the slope of the analytical curve. The spectrum for $T_w/T_r = 0.26$ shows a shift to a higher frequency range due to the presence of turbulent eddies with smaller length and time scales, which is expected due to the reduced dynamic viscosity at the wall. The developed model shows the applicability of the Liepmann model, which has been extensively studied in the incompressible regime, to the hypersonic flows.

6.4 Discussion

Presenting an alternative approach to the generation of exhaustive DNS datasets for compressible TBL, the current work shows the potential of ODT to produce important wall turbulence statistics with a significantly lower computational cost, which is attributable to the dimensionality reduction of the method. This approach can be used to explore a wide parameter space at hypersonic conditions and contribute to further validate wall scalings and inform near-wall RANS modelling. The obtained mean velocity and temperature profiles show the trends observed in DNS datasets, along with the expected variation

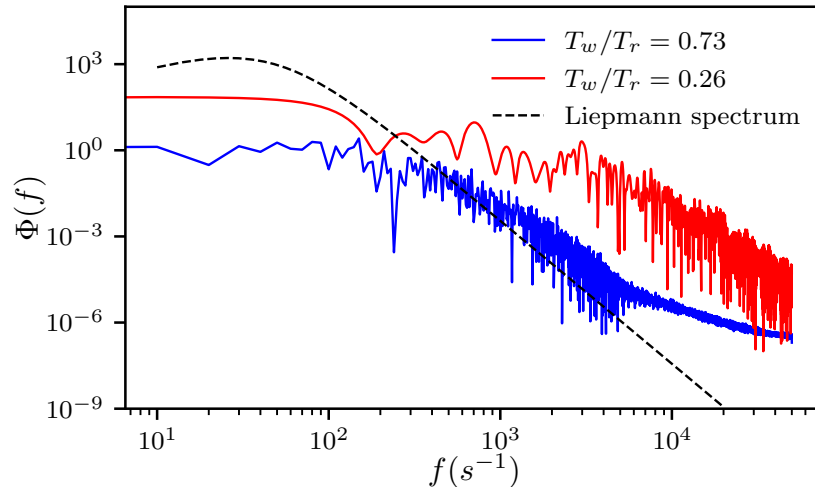


Figure 6.9: Spectrum of pressure fluctuations near wall compared with Liepmann spectrum [93] using the analytical formulation of Grasso *et al.* [50].

of Reynolds stresses. The ODT framework can characterize the heat transport and the momentum transport in the cold-wall hypersonic TBL, which is the first such attempt in a fully compressible framework, as per the author’s knowledge.

The developed model overcomes some of the shortcomings of the RANS models that are used predominantly in industrial settings for hypersonic applications. The Pr_t in the ODT framework is an outcome of the physical mechanism of transfer of momentum and heat by the eddies invoked, thus eliminating the arbitrary setting of Pr_t in RANS as input to the simulation. The developed formulation also provides access to statistics of fluctuating quantities, unlike the RANS simulations, which show only averaged statistics. PDFs of temperature statistics in the near-wall region of compressible TBL aid in the estimation of the fluctuating wall heat transport.

The assumptions inherent in the turbulence model of ODT are rooted in the multiscale nature of turbulence and thus do not bring in the same level of empiricism like RANS or LES. Although ODT shows significant promise as a predictive model for cases of com-

pressible TBL currently beyond the reach of DNS, it does not negate the importance of fully three-dimensional simulations in DNS, which are indispensable for complete characterization of wall-bounded flows. The developed model can be extended in the future to systematically generate exhaustive datasets for higher Reynolds numbers, by automatized setting up of the ODT domain based on the targeted Re_τ . Extension to $T_w/T_r < 0.25$ will potentially require smaller domains while maintaining the grid size, contrary to the present model, where the domain size is kept fixed for consistency among all simulations. Such simulations will require systematic variation of the C parameter to counteract the change in domain size. Finally, this work will be extended to investigate the thermal protection system with both ablation and transpiration cooling.

Chapter 7

Conclusions

This thesis explores the use of dimensionality reduction in turbulent flows as a methodology to develop a computationally tractable alternative to expensive DNS simulations, while retaining the essential physics of the problems. In this context, the canonical problems of homogeneous isotropic turbulence and turbulent boundary layers are studied. The models developed exhibit desirable characteristics of turbulence, reproducing characteristic results of the specific problem. For instance, the TKE spectra of HIT shows the $-5/3$ slope of the energy spectra in addition to the characteristics of dissipation region spectra. The TBL profiles have the desirable linear logarithmic region in the mean-velocity profiles with slopes matching with DNS results and other structural models such as AEM. Additional insights are gained with statistical variations of velocity-gradients and structure functions in HIT, and of fluctuations of thermal properties in the compressible TBL.

The primary benefit of advancing ODT lies in the computational savings in the exploration of extreme multi-scale turbulent flows. The computational cost of DNS scales with approximately Re_λ^6 , meaning that further high-Reynolds number flow exploration will be continue to be constrained, even under the most optimistic projections of hardware improvements. The computational expense of ODT scaling with Re_λ^3 means that continued exploration of high-Reynolds turbulent flow—without the conventional modelling assumptions—remains possible.

Chapter 3 first describes the foundational ODT model which was developed from using an incompressible assumption, and then introduces the essential elements that form the core of the developed compressible solver. An Eulerian framework is used to replace the original Lagrangian approach for compatibility with the compressible regime finite-volume schemes. The shift to an Eulerian framework aids in setting up of the zero-gradient boundary conditions, which require an intricate movement of cell walls in the Lagrangian approach. The ODT eddies are reformulated in the present model to transport conservative properties instead of primitive variables.

Chapter 4 evaluates the developed model for simulating high-Reynolds number HIT with Re_λ varying from 218 to 5428. The highest $Re_\lambda = 5428$ simulated is well beyond the current state-of-the-art DNS simulations. The potential of ODT to enable high Reynolds number modelling is rooted in the significantly lower computational cost of the one-dimensional system. The created turbulence datasets exhibit turbulent energy spectrum and energy flux spectra consistent with the DNS simulations and classical analytical findings. Extreme fluctuations are studied via probability distribution of velocity gradients, dissipation rate, and longitudinal structure functions. Stretched-exponential tails are observed in the dissipation rate statistics, which signify the intermittent characteristics of the generated turbulence. The intermittency is also quantified by analysing the scaling exponents of the high-order structure functions, and a clear deviation from the intermittency-free line is seen.

The focus of the work subsequently shifts to the turbulent boundary layers. Before proceeding to the analysis of compressible TBL, understanding the parallels of the ODT eddy model to the Attached-Eddy Model from Townsend was necessary; a foundational mechanistic model to extreme Reynolds number wall-bounded turbulent flows. In chapter 5, the ODT eddies show stark commonalities with the AEM approach in terms of the mathematical nature of the simplified R-ODT formulation, which is shown analytically and using numerical integration. ODT exhibits an inverse dependence of the eddy occurrence probability density with the eddy length scale, similar to AEM. In addition, the linear vorticity distribution and presence of a velocity scale in the expression for mean-spanwise vorticity show further equivalence of the ODT and AEM approaches. We further build on

the equivalence to use essential aspects of ODT to estimate Reynolds shear and normal stresses. The analysis identifies the central features of the ODT approach that produce the desirable trends in the TBL models.

The complete compressible ODT model was also used to simulate hypersonic TBL at $M \approx 5.86$ and its performance was assessed at low wall-to-recovery temperature ratios in chapter 6; conditions which are particularly challenging for both DNS and experiments. The low T_w/T_r flows are of practical importance as hypersonic vehicles often have cooled walls and such conditions are encountered. The availability of DNS datasets at these extreme conditions is limited, and the developed model can provide a valuable alternative to the expensive DNS models. The present work is the first known attempt to produce thermal property variation in the context of hypersonic turbulent boundary layers using ODT framework. From the developed model, we can directly compute the turbulent Prandtl number, Pr_t , as an output of the coupled heat and momentum transfer from turbulent eddies, contrary to RANS, where Pr_t is arbitrarily set to constant value, which significantly alters the simulation results. The stochastic nature of the model also enables collection of statistical properties of fluctuations of temperature and its gradients on the wall. The wall-pressure fluctuations predicted by the model for different T_w/T_r conditions show characteristics of the analytical spectrum, and provides inputs crucial for computation of structural loads on hypersonic vehicles.

Though ODT provides a nimble computational framework to model turbulence at high Reynolds numbers and compressible regime by virtue of reduced dimensionality, this work does not propose to replace the other well-established methods. DNS remains to be the cornerstone of complete three-dimensional simulation of turbulence introducing no approximations in the procedure—other than the inherent approximations used to derive the NS equations. The present model nevertheless provides an insight into the characteristics of turbulence at Reynolds numbers beyond the reach of the current models. The current model can be used as a stand-alone tool in situations where a clear characteristic dimension exists, which is the case with canonical turbulent flows. For complex three-dimensional flows, the model can aid in the development of sub-grid scale models, as is done in some LES formulations.

7.1 Future work

Multiple future directions can be undertaken to build on the developed ODT model. These relate to the parallelization of the algorithm and alternate configurations of the turbulent eddies.

- The simulations conducted in this work are performed on a serial algorithm on single-core machines. The sequential implementation of the ODT eddies for manifestation of energy cascade was important, hence a parallelized approach was not followed. However, to further accelerate the algorithms, it will be necessary to explore parallel implementation of ODT eddies. This parallel implementation is supported by the stochastic nature of the eddy implementation procedure; however, the maintenance of the correct eddy occurrence rate and correct energy flux spectra requires careful consideration. Future ODT algorithms could use massively parallel implementation of eddies if the base state is already stabilized. Other works have considered massively parallel realizations of the entire ODT simulations and collection of statistics in this regard, however, it will be particularly beneficial to have multiple eddies occurring in parallel.
- The extension of the model to compressible TBL revealed a limitation at low wall-to-recovery temperature ratios (T_w/T_r). The extremely fine resolution leads to unphysical oscillations as a result of the triplet mappings and leads to sudden crash of the simulations. This was avoided in the current simulations by restricting the lower limit of T_w/T_r . It will be important to explore alternate methodology for eddy implementation to avoid these large spurious oscillations.
- The systemization of ODT parameters C and Z over a range of flow configurations for HIT or compressible TBL is desirable for future exploration of a wider solution space. It will be beneficial to estimate the required values C and Z even before establishing the simulations, based on specific details of the flow configurations, to associate universality with the values of the parameters.

Letters of copyright permissions

The letter of permission for figure 1.2

CAMBRIDGE UNIVERSITY PRESS LICENSE
TERMS AND CONDITIONS

Jul 17, 2025

This Agreement between Pranav Nath ("You") and Cambridge University Press ("Cambridge University Press") consists of your license details and the terms and conditions provided by Cambridge University Press and Copyright Clearance Center.

License Number	6071521186606
License date	Jul 17, 2025
Licensed Content Publisher	Cambridge University Press
Licensed Content Publication	Journal of Fluid Mechanics
Licensed Content Title	Linear-eddy modelling of turbulent transport. Part 6. Microstructure of diffusive scalar mixing fields
Licensed Content Author	Alan R. Kerstein
Licensed Content Date	Apr 26, 2006
Licensed Content Volume	231
Start page	361
End page	394
Type of Use	Book/Textbook
Requestor type	Author

Requestor details	Not-for-profit
Format	Electronic
Portion	Figure/table
Number of figures/tables	1
Author of this Cambridge University Press article	No
Author / editor of the new work	Yes
Title of new book	One-Dimensional Turbulence: From Extreme Reynolds Number Turbulence to Hypersonic Turbulent Boundary Layers
Lead author	Pranav Nath
Publisher	University of Waterloo
Expected publication date	Aug 2025
Expected number of pages	223
Portions	Figure 2
The Requesting Person / Organization to Appear on the License	Pranav Nath
Territory for reuse	World
If publisher of new book has its main base in USA, Canada or Mexico	Yes

Requestor Location	Mr. Pranav Nath 350 Columbia St W Unit 331 Waterloo, ON N2L 6P8 Canada
Publisher Tax ID	123258667RT0001
Billing Type	Invoice
Billing Address	Mr. Pranav Nath 350 Columbia St W Unit 331 Waterloo, ON N2L 6P8 Canada
Total	0.00 CAD

Terms and Conditions

TERMS & CONDITIONS

Cambridge University Press grants the Licensee permission on a non-exclusive non-transferable basis to reproduce, make available or otherwise use the Licensed content 'Content' in the named territory 'Territory' for the purpose listed 'the Use' on Page 1 of this Agreement subject to the following terms and conditions.

1. The License is limited to the permission granted and the Content detailed herein and does not extend to any other permission or content.
2. Cambridge gives no warranty or indemnity in respect of any third-party copyright material included in the Content, for which the Licensee should seek separate permission clearance.
3. The integrity of the Content must be ensured.
4. The License does extend to any edition published specifically for the use of handicapped or reading-impaired individuals.
5. The Licensee shall provide a prominent acknowledgement in the following format: author/s, title of article, name of journal, volume number, issue number, page references, , reproduced with permission.

Other terms and conditions:

v1.0

Questions? customercare@copyright.com.

The letter of permission for figure 2.2

CAMBRIDGE UNIVERSITY PRESS LICENSE
TERMS AND CONDITIONS

Jul 17, 2025

This Agreement between Pranav Nath ("You") and Cambridge University Press ("Cambridge University Press") consists of your license details and the terms and conditions provided by Cambridge University Press and Copyright Clearance Center.

License Number	6071520759249
License date	Jul 17, 2025
Licensed Content Publisher	Cambridge University Press
Licensed Content Publication	Journal of Fluid Mechanics
Licensed Content Title	Vortical structure in the wake of a transverse jet
Licensed Content Author	T. F. Fric, A. Roshko
Licensed Content Date	Apr 26, 2006
Licensed Content Volume	279
Start page	1
End page	47
Type of Use	Book/Textbook
Requestor type	Author
Requestor details	Not-for-profit

Format	Electronic
Portion	Figure/table
Number of figures/tables	1
Author of this Cambridge University Press article	No
Author / editor of the new work	Yes
Title of new book	One-Dimensional Turbulence: From Extreme Reynolds Number Turbulence to Hypersonic Turbulent Boundary Layers
Lead author	Pranav Nath
Publisher	University of Waterloo
Expected publication date	Aug 2025
Expected number of pages	223
Portions	Figure 1
The Requesting Person / Organization to Appear on the License	Pranav Nath
Territory for reuse	World
If publisher of new book has its main base in USA, Canada or Mexico	Yes
Requestor Location	Mr. Pranav Nath 350 Columbia St W Unit 331

Waterloo, ON N2L 6P8
Canada

Publisher Tax ID 123258667RT0001

Billing Type Invoice

Billing Address Mr. Pranav Nath
350 Columbia St W
Unit 331

Waterloo, ON N2L 6P8
Canada

Total 0.00 CAD

Terms and Conditions

TERMS & CONDITIONS

Cambridge University Press grants the Licensee permission on a non-exclusive non-transferable basis to reproduce, make available or otherwise use the Licensed content 'Content' in the named territory 'Territory' for the purpose listed 'the Use' on Page 1 of this Agreement subject to the following terms and conditions.

1. The License is limited to the permission granted and the Content detailed herein and does not extend to any other permission or content.
2. Cambridge gives no warranty or indemnity in respect of any third-party copyright material included in the Content, for which the Licensee should seek separate permission clearance.
3. The integrity of the Content must be ensured.
4. The License does extend to any edition published specifically for the use of handicapped or reading-impaired individuals.
5. The Licensee shall provide a prominent acknowledgement in the following format: author/s, title of article, name of journal, volume number, issue number, page references, , reproduced with permission.

Other terms and conditions:

v1.0

Questions? customercare@copyright.com.

The letter of permission for figure 2.3

CAMBRIDGE UNIVERSITY PRESS LICENSE
TERMS AND CONDITIONS

Jul 17, 2025

This Agreement between Pranav Nath ("You") and Cambridge University Press ("Cambridge University Press") consists of your license details and the terms and conditions provided by Cambridge University Press and Copyright Clearance Center.

License Number	6071521032344
License date	Jul 17, 2025
Licensed Content Publisher	Cambridge University Press
Licensed Content Publication	Journal of Fluid Mechanics
Licensed Content Title	Compressibility effects on the structural evolution of transitional high-speed planar wakes
Licensed Content Author	Jean-Pierre Hickey, Fazle Hussain, Xiaohua Wu
Licensed Content Date	Apr 28, 2016
Licensed Content Volume	796
Start page	5
End page	39
Type of Use	Book/Textbook
Requestor type	Author

Requestor details	Not-for-profit
Format	Electronic
Portion	Figure/table
Number of figures/tables	1
Author of this Cambridge University Press article	No
Author / editor of the new work	Yes
Title of new book	One-Dimensional Turbulence: From Extreme Reynolds Number Turbulence to Hypersonic Turbulent Boundary Layers
Lead author	Pranav Nath
Publisher	University of Waterloo
Expected publication date	Aug 2025
Expected number of pages	223
Portions	Figure 17
The Requesting Person / Organization to Appear on the License	Pranav Nath
Territory for reuse	World
If publisher of new book has its main base in USA, Canada or Mexico	Yes

Requestor Location	Mr. Pranav Nath 350 Columbia St W Unit 331 Waterloo, ON N2L 6P8 Canada
Publisher Tax ID	123258667RT0001
Billing Type	Invoice
Billing Address	Mr. Pranav Nath 350 Columbia St W Unit 331 Waterloo, ON N2L 6P8 Canada
Total	0.00 CAD

Terms and Conditions

TERMS & CONDITIONS

Cambridge University Press grants the Licensee permission on a non-exclusive non-transferable basis to reproduce, make available or otherwise use the Licensed content 'Content' in the named territory 'Territory' for the purpose listed 'the Use' on Page 1 of this Agreement subject to the following terms and conditions.

1. The License is limited to the permission granted and the Content detailed herein and does not extend to any other permission or content.
2. Cambridge gives no warranty or indemnity in respect of any third-party copyright material included in the Content, for which the Licensee should seek separate permission clearance.
3. The integrity of the Content must be ensured.
4. The License does extend to any edition published specifically for the use of handicapped or reading-impaired individuals.
5. The Licensee shall provide a prominent acknowledgement in the following format: author/s, title of article, name of journal, volume number, issue number, page references, , reproduced with permission.

Other terms and conditions:

v1.0

Questions? customercare@copyright.com.

The letter of permission for chapter 4



13-Aug-2025

This license agreement between the American Physical Society ("APS") and Pranav Nath ("You") consists of your license details and the terms and conditions provided by the American Physical Society and SciPris.

Licensed Content Information

License Number: RNP/25/AUG/094458
License date: 13-Aug-2025
DOI: 10.1103/PhysRevFluids.10.054602
Title: High-order statistics and extreme fluctuations in stationary turbulence via one-dimensional turbulence
Author: Pranav Nath and Jean-Pierre Hickey
Publication: Physical Review Fluids
Publisher: American Physical Society
Cost: USD \$ 0.00

Request Details

Does your reuse require significant modifications: No
Specify intended distribution locations: Worldwide
Reuse Category: Reuse in a thesis/dissertation
Requestor Type: Student
Items for Reuse: Whole Article
Format for Reuse: Electronic

Information about New Publication:

University/Publisher: University of Waterloo
Title of dissertation/thesis: One-Dimensional Turbulence: From Extreme Reynolds Number Turbulence to Hypersonic Turbulent Boundary Layers
Author(s): Pranav Nath
Expected completion date: Aug. 2025

License Requestor Information

Name: Pranav Nath
Affiliation: Individual
Email Id: p2nath@uwaterloo.ca
Country: Canada



TERMS AND CONDITIONS

The American Physical Society (APS) is pleased to grant the Requestor of this license a non-exclusive, non-transferable permission, limited to Electronic format, provided all criteria outlined below are followed.

1. You must also obtain permission from at least one of the lead authors for each separate work, if you haven't done so already. The author's name and affiliation can be found on the first page of the published Article.
2. For electronic format permissions, Requestor agrees to provide a hyperlink from the reprinted APS material using the source material's DOI on the web page where the work appears. The hyperlink should use the standard DOI resolution URL, <http://dx.doi.org/{DOI}>. The hyperlink may be embedded in the copyright credit line.
3. For print format permissions, Requestor agrees to print the required copyright credit line on the first page where the material appears: "Reprinted (abstract/excerpt/figure) with permission from [(FULL REFERENCE CITATION) as follows: Author's Names, APS Journal Title, Volume Number, Page Number and Year of Publication.] Copyright (YEAR) by the American Physical Society."
4. Permission granted in this license is for a one-time use and does not include permission for any future editions, updates, databases, formats or other matters. Permission must be sought for any additional use.
5. Use of the material does not and must not imply any endorsement by APS.
6. APS does not imply, purport or intend to grant permission to reuse materials to which it does not hold copyright. It is the requestor's sole responsibility to ensure the licensed material is original to APS and does not contain the copyright of another entity, and that the copyright notice of the figure, photograph, cover or table does not indicate it was reprinted by APS with permission from another source.
7. The permission granted herein is personal to the Requestor for the use specified and is not transferable or assignable without express written permission of APS. This license may not be amended except in writing by APS.
8. You may not alter, edit or modify the material in any manner.
9. You may translate the materials only when translation rights have been granted.
10. APS is not responsible for any errors or omissions due to translation.
11. You may not use the material for promotional, sales, advertising or marketing purposes.
12. The foregoing license shall not take effect unless and until APS or its agent, Aptara, receives payment in full in accordance with Aptara Billing and Payment Terms and Conditions, which are incorporated herein by reference.
13. Should the terms of this license be violated at any time, APS or Aptara may revoke the license with no refund to you and seek relief to the fullest extent of the laws of the USA. Official written notice will be made using the contact information provided with the permission request. Failure to receive such notice will not nullify revocation of the permission.
14. APS reserves all rights not specifically granted herein.
15. This document, including the Aptara Billing and Payment Terms and Conditions, shall be the entire agreement between the parties relating to the subject matter hereof.

References

- [1] R. J. Adrian. Hairpin vortex organization in wall turbulence. *Physics of Fluids*, 19(4):041301, 04 2007.
- [2] R. J. Adrian and I. Marusic. Coherent structures in flow over hydraulic engineering surfaces. *Journal of Hydraulic Research*, 50(5):451–464, 2012.
- [3] R. J. Adrian, C. D. Meinhart, and C. D. Tomkins. Vortex organization in the outer region of the turbulent boundary layer. *Journal of Fluid Mechanics*, 422:1–54, 2000.
- [4] F. Anselmet, Y. Gagne, E. J. Hopfinger, and R. A. Antonia. High-order velocity structure functions in turbulent shear flows. *Journal of Fluid Mechanics*, 140:63–89, 1984.
- [5] R. A. Antonia, S. L. Tang, L. Djenidi, and L. Danaila. Boundedness of the velocity derivative skewness in various turbulent flows. *Journal of Fluid Mechanics*, 781:727–744, 10 2015.
- [6] W. T. Ashurst and A. R. Kerstein. One-dimensional turbulence: Variable-density formulation and application to mixing layers. *Physics of Fluids*, 17:025107, 2005.
- [7] P. Bagade and S. B. Krishnan. DNS of low Reynolds number aerodynamics in the presence of free stream turbulence. *Journal of Aerospace Engineering*, 4:20–34, 04 2015.

- [8] G. K. Batchelor. *The theory of homogeneous turbulence*. Cambridge Science Classics. Cambridge University Press, 1982.
- [9] M. Bernardini and S. Pirozzoli. Wall pressure fluctuations beneath supersonic turbulent boundary layers. *Physics of Fluids*, 23(8):085102, 08 2011.
- [10] L. Biferale. Shell models of energy cascade in turbulence. *Annual Review of Fluid Mechanics*, 35:441–468, 2003.
- [11] W. J. T. Bos, L. Shao, and J.P. Bertoglio. Spectral imbalance and the normalized dissipation rate of turbulence. *Physics of Fluids*, 19(4):045101, 04 2007.
- [12] P. Bradshaw, G. P. Huang, and B. E. Launder. The law of the wall in turbulent flow. *Proceedings of the Royal Society of London. Series A: Mathematical and Physical Sciences*, 451(1941):165–188, 1995.
- [13] G.L. Brown and A. Roshko. On density effects and large structure in turbulent mixing layers. *J. Fluid Mech.*, 64:775–816, 1974.
- [14] D. Buaria and K. R. Sreenivasan. Forecasting small scale dynamics of fluid turbulence using deep neural networks. *Applied Physical Sciences*, 4 2023.
- [15] P. Burattini, P. Lavoie, and R. A. Antonia. On the normalized turbulent energy dissipation rate. *Physics of Fluids*, 17(9):098103, 09 2005.
- [16] V. M. Canuto and J. Christensen-Dalsgaard. Turbulence in astrophysics: Stars. *Annual Review of Fluid Mechanics*, 30:167–198, 1998.
- [17] K. M. Casper, S. J. Beresh, J. F. Henfling, R. W. Spillers, P. Hunter, and S. Spitzer. Hypersonic fluid–structure interactions due to intermittent turbulent spots on a slender cone. *AIAA Journal*, 57(2):749–759, 2019.
- [18] J.M. Catalán, S. Olivieri, M. García-Villalba, and O. Flores. On the generation of free-stream turbulence at low Reynolds number: A numerical study. *Computers and Fluids*, 280:106345, 2024.

- [19] G. T Chapman and M. Tobak. Observations, theoretical ideas, and modeling of turbulent flows—past, present, and future. In *Theoretical approaches to turbulence*, pages 19–49. Springer, 1985.
- [20] C. Chen, J. Liang, T. Gao, X. Wu, W. Zhao, and L. Zhang. Conservative compressible one-dimensional turbulence formulation and application to high-Reynolds-number compressible turbulent channel flows. *Physics of Fluids*, 34:065121, 6 2022.
- [21] S. Chen, K. R. Sreenivasan, and M. Nelkin. Inertial range scalings of dissipation and enstrophy in isotropic turbulence. *Phys. Rev. Lett.*, 79:1253–1256, Aug 1997.
- [22] C. Cheng, X. Chen, W. Zhu, W. Shyy, and L. Fu. Progress in physical modeling of compressible wall-bounded turbulent flows. *Acta Mechanica Sinica*, 40(1):323663, 2024.
- [23] C. Cheng and L. Fu. Comparisons between the first- and second-order spectral stochastic estimations in investigating the multiphysics couplings for a supersonic turbulent channel flow. *Phys. Rev. Fluids*, 9:104607, Oct 2024.
- [24] C. Cheng and L. Fu. Mean temperature scalings in compressible wall turbulence. *Phys. Rev. Fluids*, 9:054610, May 2024.
- [25] P. Constantin, B. Levant, and E. S. Titi. Analytic study of shell models of turbulence. *Physica D: Nonlinear Phenomena*, 219(2):120–141, 2006.
- [26] J. W. Deardorff. Three-dimensional numerical study of the height and mean structure of a heated planetary boundary layer. *Boundary-Layer Meteorology*, 7:81–106, 1974.
- [27] J. C. del Álamo, J. Jiménez, P. Zandonade, and R. D. Moser. Scaling of the energy spectra of turbulent channels. *Journal of Fluid Mechanics*, 500:135–144, 2004.
- [28] J. C. del Álamo, J. Jiménez, P. Zandonade, and R. D. Moser. Self-similar vortex clusters in the turbulent logarithmic region. *Journal of Fluid Mechanics*, 561:329–358, 2006.

- [29] D. A. Donzis, K. R. Sreenivasan, and P. K. Yeung. Scalar dissipation rate and dissipative anomaly in isotropic turbulence. *Journal of Fluid Mechanics*, 532:199–216, 6 2005.
- [30] D. A. Donzis, P. K. Yeung, and K. R. Sreenivasan. Dissipation and enstrophy in isotropic turbulence: Resolution effects and scaling in direct numerical simulations. *Physics of Fluids*, 20(4):045108, 04 2008.
- [31] L. Duan, I. Beekman, and M. P. Martín. Direct numerical simulation of hypersonic turbulent boundary layers. Part 2. Effect of wall temperature. *Journal of Fluid Mechanics*, 655:419–445, 2010.
- [32] L. Duan, I. Beekman, and M. P. Martín. Direct numerical simulation of hypersonic turbulent boundary layers. Part 3. Effect of Mach number. *Journal of Fluid Mechanics*, 672:245–267, 2011.
- [33] L. Duan, M. M. Choudhari, and C. Zhang. Pressure fluctuations induced by a hypersonic turbulent boundary layer. *Journal of Fluid Mechanics*, 804:578–607, 2016.
- [34] L. Duan and M. P. Martin. Effect of finite-rate chemical reactions on turbulence in hypersonic turbulence boundary layers. In *47th AIAA Aerospace Sciences Meeting including The New Horizons Forum and Aerospace Exposition, Orlando, Florida*, 2009.
- [35] L. Duan and M. P. Martín. Direct numerical simulation of hypersonic turbulent boundary layers. Part 4. Effect of high enthalpy. *Journal of Fluid Mechanics*, 684:25–59, 2011.
- [36] B. Dubrulle. Anomalous scaling and generic structure function in turbulence. *Journal de Physique II*, 6:1825–1840, 06 2011.
- [37] B. Eisfeld. Implementation of Reynolds stress models into the DLR-FLOWer code. Technical report, Institute of Aerodynamics and Flow Technology, 2004. LIDO-Berichtsjahr=2005,.

- [38] G. E. Elsinga, T. Ishihara, and J. C. R. Hunt. Extreme dissipation and intermittency in turbulence at very high Reynolds numbers. *Proceedings of the Royal Society A: Mathematical, Physical and Engineering Sciences*, 476(2243):20200591, November 2020.
- [39] H. E. Fiedler. Coherent structures in turbulent flows. *Progress in Aerospace Sciences*, 25(3):231–269, 1988.
- [40] M. Fistler, A. R. Kerstein, D. O. Lignell, and M. Oevermann. Turbulence modulation in particle-laden stationary homogeneous isotropic turbulence using one-dimensional turbulence. *Physical Review Fluids*, 5:044308, 4 2020.
- [41] L. S. Freire and M. Chamecki. Large-eddy simulation of smooth and rough channel flows using a one-dimensional stochastic wall model. *Computers and Fluids*, 230:105135, 2021.
- [42] T. F. Fric and A. Roshko. Vortical structure in the wake of a transverse jet. *Journal of Fluid Mechanics*, 279:1–47, 1994.
- [43] U. Frisch. *Turbulence: The Legacy of A. N. Kolmogorov*. Cambridge University Press, 1995.
- [44] T. Gao, H. Schmidt, M. Klein, J. Liang, M. Sun, C. Chen, and Q. Guan. One-dimensional turbulence modeling of compressible flows. I. Conservative Eulerian formulation and application to supersonic channel flow. *Physics of Fluids*, 35(3):035115, 03 2023.
- [45] T. Gao, H. Schmidt, M. Klein, J. Liang, M. Sun, C. Chen, and Q. Guan. One-dimensional turbulence modeling of compressible flows: II. Full compressible modification and application to shock–turbulence interaction. *Physics of Fluids*, 35:035116, 3 2023.
- [46] E. D. Gonzalez-Juez, A. R. Kerstein, and D. O. Lignell. Reactive Rayleigh–Taylor turbulent mixing: a one-dimensional-turbulence study. *Geophysical & Astrophysical Fluid Dynamics*, 107(5):506–525, 2013.

- [47] T. Gotoh, D. Fukayama, and T. Nakano. Velocity field statistics in homogeneous steady turbulence obtained using a high-resolution direct numerical simulation. *Physics of Fluids*, 14(3):1065–1081, 03 2002.
- [48] T. Gotoh and T. Watanabe. Statistics of transfer fluxes of the kinetic energy and scalar variance. *Journal of Turbulence*, 6:N33, 2005.
- [49] J. Graham, K. Kanov, X. I. A. Yang, M. Lee, N. Malaya, C. C. Lalescu, R. Burns, G. Eyink, A. Szalay, R. D. Moser, and C. Meneveau. A web services accessible database of turbulent channel flow and its use for testing a new integral wall model for LES. *Journal of Turbulence*, 17:181–215, 2016.
- [50] G. Grasso, P. Jaiswal, H. Wu, S. Moreau, and M. Roger. Analytical models of the wall-pressure spectrum under a turbulent boundary layer with adverse pressure gradient. *Journal of Fluid Mechanics*, 877:1007–1062, 2019.
- [51] K. P. Griffin, L. Fu, and P. Moin. Velocity transformation for compressible wall-bounded turbulent flows with and without heat transfer. *Proceedings of the National Academy of Sciences*, 118(34):e2111144118, 2021.
- [52] J. P. Hickey, F. Hussain, and X. Wu. Role of coherent structures in multiple self-similar states of turbulent planar wakes. *Journal of Fluid Mechanics*, 731:312–363, 2013.
- [53] J. P. Hickey, F. Hussain, and X. Wu. Compressibility effects on the structural evolution of transitional high-speed planar wakes. *Journal of Fluid Mechanics*, 796:5–39, 2016.
- [54] C. M. Ho and P. Huerre. Perturbed free shear layers. *Annual Review of Fluid Mechanics*, 16(Volume 16, 1984):365–422, 1984.
- [55] R. W. Houim and K. K. Kuo. A low-dissipation and time-accurate method for compressible multi-component flow with variable specific heat ratios. *Journal of Computational Physics*, 230:8527–8553, 2011.

- [56] S. Hoyas and J. Jiménez. Scaling of the velocity fluctuations in turbulent channels up to $Re_\tau=2003$. *Physics of Fluids*, 18(1):011702, 01 2006.
- [57] J. Huang, L. Duan, and M. M. Choudhari. Direct numerical simulation of hypersonic turbulent boundary layers: effect of spatial evolution and Reynolds number. *Journal of Fluid Mechanics*, 937:A3, 2022.
- [58] J. Huang, G. L. Nicholson, L. Duan, M. M. Choudhari, and R. D. Bowersox. Simulation and modeling of cold-wall hypersonic turbulent boundary layers on flat plate. In *AIAA Scitech 2020 Forum, Orlando, Florida*, 2020.
- [59] G. D. Huffman and P. Bradshaw. A note on von Kármán’s constant in low Reynolds number turbulent flows. *Journal of Fluid Mechanics*, 53(1):45–60, 1972.
- [60] J. C. R. Hunt, A. A. Wray, and P. Moin. Eddies, streams, and convergence zones in turbulent flows. Technical report, Center for turbulence research, 1988.
- [61] Clay Mathematics Institute. *The Millennium Prize Problems*. Providence, RI: American Mathematical Society and Clay Mathematics Institute. ISBN 978-0-8218-3679-8, 2006.
- [62] T. Ishihara, T. Gotoh, and Y. Kaneda. Study of high-Reynolds number isotropic turbulence by direct numerical simulation. *Annual Review of Fluid Mechanics*, 41:165–180, 1 2009.
- [63] T. Ishihara, Y. Kaneda, and J. C. R. Hunt. Thin shear layers in high Reynolds number turbulence—DNS results. *Flow Turbulence Combust*, 91:895–929, 2013.
- [64] T. Ishihara, Y. Kaneda, K. Morishita, M. Yokokawa, and A. Uno. Second-order velocity structure functions in direct numerical simulations of turbulence with R_λ up to 2250. *Physical Review Fluids*, 5:104608, 10 2020.
- [65] T. Ishihara, Y. Kaneda, M. Yokokawa, K. Itakura, and A. Uno. Energy spectrum in the near dissipation range of high resolution direct numerical simulation of turbulence. *Journal of the Physical Society of Japan*, 74(5):1464–1471, 2005.

- [66] T. Ishihara, Y. Kaneda, M. Yokokawa, K. Itakura, and A. Uno. Small-scale statistics in high-resolution direct numerical simulation of turbulence: Reynolds number dependence of one-point velocity gradient statistics. *Journal of Fluid Mechanics*, 592:335–366, 12 2007.
- [67] T. Ishihara, K. Morishita, M. Yokokawa, A. Uno, and Y. Kaneda. Energy spectrum in high-resolution direct numerical simulations of turbulence. *Physical Review Fluids*, 1, 12 2016.
- [68] K. P. Iyer, K. R. Sreenivasan, and P. K. Yeung. Reynolds number scaling of velocity increments in isotropic turbulence. *Phys. Rev. E*, 95:021101, Feb 2017.
- [69] K. P. Iyer, K. R. Sreenivasan, and P. K. Yeung. Scaling exponents saturate in three-dimensional isotropic turbulence. *Physical Review Fluids*, 5:054605, May 2020.
- [70] J. Jeong and F. Hussain. On the identification of a vortex. *Journal of Fluid Mechanics*, 285:69–94, 1995.
- [71] J. Jiménez. Coherent structures in wall-bounded turbulence. *Journal of Fluid Mechanics*, 842:P1, 2018.
- [72] W. P. Jones and B. E. Launder. The prediction of laminarization with a two-equation model of turbulence. *International Journal of Heat and Mass Transfer*, 15(2):301–314, 1972.
- [73] Z. Jozefik, A. R. Kerstein, and H. Schmidt. Simulation of shock-turbulence interaction in non-reactive flow and in turbulent deflagration and detonation regimes using one-dimensional turbulence. *Combustion and Flame*, 164:53–67, 2 2016.
- [74] Z. Jozefik, A. R. Kerstein, H. Schmidt, S. Lyra, H. Kolla, and J. Chen. One-dimensional turbulence modeling of a turbulent counterflow flame with comparison to DNS. *Combustion and Flame*, 162, 06 2015.
- [75] B. A. Kader. Temperature and concentration profiles in fully turbulent boundary layers. *International Journal of Heat and Mass Transfer*, 24(9):1541–1544, 1981.

- [76] Y. Kaneda, T. Ishihara, M. Yokokawa, K. Itakura, and A. Uno. Energy dissipation rate and energy spectrum in high resolution direct numerical simulations of turbulence in a periodic box. *Physics of Fluids*, 15(2):L21–L24, 02 2003.
- [77] A. R. Kerstein. Linear-eddy modelling of turbulent transport. Part 6. Microstructure of diffusive scalar mixing fields. *Journal of Fluid Mechanics*, 231:361–394, 1991.
- [78] A. R. Kerstein. One-dimensional turbulence: Model formulation and application to homogeneous turbulence, shear flows, and buoyant stratified flows. *Journal of Fluid Mechanics*, 392:277–334, 8 1999.
- [79] A. R. Kerstein. Reduced numerical modeling of turbulent flow with fully resolved time advancement. Part 1. Theory and physical interpretation. *Fluids*, 7(2), 2022.
- [80] A. R. Kerstein, W. T. Ashurst, S. Wunsch, and V. Nilsen. One-dimensional turbulence: Vector formulation and application to free shear flows. *Journal of Fluid Mechanics*, 447:85–109, 11 2001.
- [81] A. R. Kerstein and P. A. McMurtry. Low-wave-number statistics of randomly advected passive scalars. *Physical Review E*, 50:2057–2063, Sep 1994.
- [82] S. Khurshid, D. A. Donzis, and K. R. Sreenivasan. Energy spectrum in the dissipation range. *Phys. Rev. Fluids*, 3:082601, Aug 2018.
- [83] J. Kim, P. Moin, and R. Moser. Turbulence statistics in fully developed channel flow at low Reynolds number. *Journal of Fluid Mechanics*, 177:133–166, 1987.
- [84] M. Klein and H. Schmidt. Capturing features of turbulent Ekman-Stokes boundary layers with a stochastic modeling approach. *Advances in Science and Research*, 20:55–64, 7 2023.
- [85] M. Klein, H. Schmidt, and D. O. Lignell. Stochastic modeling of surface scalar-flux fluctuations in turbulent channel flow using one-dimensional turbulence. *International Journal of Heat and Fluid Flow*, 93, 2 2022.

- [86] A. N. Kolmogorov. Dissipation of energy in the locally isotropic turbulence. *Akademiia Nauk SSSR Doklady*, 32:19–21 [In Russian], 1941.
- [87] A. N. Kolmogorov. The local structure of turbulence in incompressible viscous fluid for very large Reynolds numbers. *Akademiia Nauk SSSR Doklady*, 30:299–303 [In Russian], 1941.
- [88] A. N. Kolmogorov. A refinement of previous hypotheses concerning the local structure of turbulence in a viscous incompressible fluid at high Reynolds number. *Journal of Fluid Mechanics*, 13(1):82–85, 1962.
- [89] M. Lagha, J. Kim, J. D. Eldredge, and X. Zhong. A numerical study of compressible turbulent boundary layers. *Physics of Fluids*, 23(1):015106, 01 2011.
- [90] J. Larsson, S. Kawai, J. Bodart, and I. Bermejo-Moreno. Large eddy simulation with modeled wall-stress: recent progress and future directions. *Mechanical Engineering Reviews*, 3(1):15–00418–15–00418, 2016.
- [91] B. E. Launder and B. I. Sharma. Application of the energy-dissipation model of turbulence to the calculation of flow near a spinning disc. *Letters in Heat and Mass Transfer*, 1(2):131–137, 1974.
- [92] M. Lee and R. D. Moser. Direct numerical simulation of turbulent channel flow up to $Re_\tau \approx 5200$. *Journal of Fluid Mechanics*, 774:395–415, 2015.
- [93] H. W. Liepmann, J. Laufer, and K. Liepmann. On the spectrum of isotropic turbulence (no. NACA-TN-2473). Technical report, California Institute of Technology, 1951.
- [94] D. O. Lignell, A. R. Kerstein, G. Sun, and E. I. Monson. Mesh adaption for efficient multiscale implementation of one-dimensional turbulence. In *Theoretical and Computational Fluid Dynamics*, volume 27, pages 273–295, 6 2013.
- [95] D. O. Lignell, V. B. Lansinger, J. Medina, M. Klein, A. R. Kerstein, H. Schmidt, M. Fistler, and M. Oevermann. One-dimensional turbulence modeling for cylindrical

- and spherical flows: model formulation and application. *Theoretical and Computational Fluid Dynamics*, 32:495–520, 8 2018.
- [96] D. O. Lignell and D. S. Rappleye. One-dimensional-turbulence simulation of flame extinction and reignition in planar ethylene jet flames. *Combustion and Flame*, 159(9):2930–2943, 2012.
- [97] D. K. Lilly. The representation of small-scale turbulence in numerical simulation experiments. Technical report, National Center for Atmospheric Research (U.S.), 1966.
- [98] J. Limei, X. Yuan, S. Dong, X. Li, and F. Tong. Extremely high wall pressure events in shock wave and turbulent boundary layer interactions using DNS data. *Chinese Journal of Aeronautics*, 37(11):81–93, 2024.
- [99] A. Lozano-Durán, O. Flores, and J. Jiménez. The three-dimensional structure of momentum transfer in turbulent channels. *Journal of Fluid Mechanics*, 694:100–130, 2012.
- [100] A. Lozano-Durán and J. Jiménez. Effect of the computational domain on direct simulations of turbulent channels up to $Re_\tau = 4200$. *Physics of Fluids*, 26(1):011702, 01 2014.
- [101] A. Lozano-Durán and J. Jiménez. Time-resolved evolution of coherent structures in turbulent channels: characterization of eddies and cascades. *Journal of Fluid Mechanics*, 759:432–471, 2014.
- [102] J. L. Lumley. Turbulence modeling. *ASME Journal of Applied Mechanics*, 50:1097–1103, December 1983.
- [103] J. R. Luévano. Statistical features of the stretched exponential densities. *Journal of Physics: Conference Series*, 475(1):012008, dec 2013.

- [104] S. L. Lyons, T. J. Hanratty, and J. B. McLaughlin. Large-scale computer simulation of fully developed turbulent channel flow with heat transfer. *International Journal for Numerical Methods in Fluids*, 13(8):999–1028, 1991.
- [105] B. B. Mandelbrot. Intermittent turbulence in self-similar cascades: divergence of high moments and dimension of the carrier. *Journal of Fluid Mechanics*, 62(2):331–358, 1974.
- [106] H. Marmanis, C. W. Hamman, and R. M. Kirby. A one-dimensional model of the Navier-Stokes. *Technical Report No. UUSCI-2006-012, Scientific Computing and Imaging Institute, University of Utah, Salt Lake City, USA*, 2006.
- [107] M. P. Martin. DNS of hypersonic turbulent boundary layers. In *34th AIAA Fluid Dynamics Conference and Exhibit, Portland, Oregon, 2004*.
- [108] M. P. Martin. Direct numerical simulation of hypersonic turbulent boundary layers. Part 1. Initialization and comparison with experiments. *Journal of Fluid Mechanics*, 570:347–364, 2007.
- [109] D. O. Martínez, S. Chen, G. D. Doolen, R. H. Kraichnan, L.-P. Wang, and Y. Zhou. Energy spectrum in the dissipation range of fluid turbulence. *Journal of Plasma Physics*, 57(1):195–201, 1997.
- [110] M. P. Martín and L. Duan. Assessment of turbulence-chemistry interaction in hypersonic turbulent boundary layers. *AIAA Journal*, 49:172–184, 06 2011.
- [111] I. Marusic. On the role of large-scale structures in wall turbulence. *Physics of Fluids*, 13(3):735–743, 03 2001.
- [112] I. Marusic and J. P. Monty. Attached eddy model of wall turbulence. *Annual Review of Fluid Mechanics*, 51:49–74, 2019.
- [113] I. Marusic, J. P. Monty, M. Hultmark, and A. J. Smits. On the logarithmic region in wall turbulence. *Journal of Fluid Mechanics*, 716:R3, 2013.

- [114] O. Marxen, T. E. Magin, E. S. G. Shaqfeh, and G. Iaccarino. A method for the direct numerical simulation of hypersonic boundary-layer instability with finite-rate chemistry. *Journal of Computational Physics*, 255:572–589, 2013.
- [115] S. Menon and A. R. Kerstein. The linear-eddy model. pages 221–247, 2011.
- [116] E. I. Monson, D. O. Lignell, M. A. Finney, C. Werner, Z. Jozefik, A. R. Kerstein, and R. S. Hintze. Simulation of ethylene wall fires using the spatially-evolving one-dimensional turbulence model. *Fire technology*, 52:167–196, 2016.
- [117] M. Morkovin. Effects of compressibility on turbulent flows. *Mécanique de la Turbulence, edited by A. Favre (CNRS)*, 1969.
- [118] R. D. Moser, J. Kim, and N. N. Mansour. Direct numerical simulation of turbulent channel flow up to $Re_\tau=590$. *Physics of Fluids*, 11:943–945, 1999.
- [119] A. Movaghar, R. Chiodi, O. Desjardins, M. Oevermann, and A. R. Kerstein. A subgrid-scale model for large-eddy simulation of liquid/gas interfaces based on one-dimensional turbulence. In Mikhael Gorokhovski and Fabien S. Godefert, editors, *Turbulent Cascades II*, pages 83–91, Cham, 2019. Springer International Publishing.
- [120] A. Movaghar, R. Chiodi, M. Oevermann, O. Desjardins, and A. R. Kerstein. Assessment of a multiphase formulation of one-dimensional turbulence using direct numerical simulation of a decaying turbulent interfacial flow. *Physical Review Fluids*, 9:104003, Oct 2024.
- [121] P. Nath and J. P. Hickey. Features of the attached-eddy hypothesis in one-dimensional turbulence models of turbulent boundary layers. *under consideration for publication in Physical Review Fluids*.
- [122] P. Nath and J. P. Hickey. High-order statistics and extreme fluctuations in stationary turbulence via one-dimensional turbulence. *Phys. Rev. Fluids*, 10:054602, May 2025.

- [123] M. Nelkin. Enstrophy and dissipation must have the same scaling exponent in the high Reynolds number limit of fluid turbulence. *Physics of Fluids*, 11(8):2202–2204, 08 1999.
- [124] J. Nikuradse. Untersuchungen über die strömungen des wassers in konvergenten und divergenten röhren. *Forsch. Geb. Ing. Wes.*, Heft 289, 1929.
- [125] A. M. Oboukhov. Some specific features of atmospheric turbulence. *Journal of Fluid Mechanics*, 13(1):77–81, 1962.
- [126] S. A. Orszag and G. S. Patterson. Numerical simulation of three-dimensional homogeneous isotropic turbulence. *Phys. Rev. Lett.*, 28:76–79, Jan 1972.
- [127] W. D. Ostwal. Ueber die rechnerische darstellung des strukturgebietes der viskosität. *Kolloid-Zeitschrift*, 47:176–187, 1929.
- [128] E. Parish, D. S. Ching, C. Jordan, G. Nicholson, N. E. Miller, S. Beresh, M. Barone, N. Gupta, and K. Duraisamy. Data-driven turbulent Prandtl number modeling for hypersonic shock–boundary-layer interactions. *AIAA Journal*, 63(5):1671–1692, 2025.
- [129] A. Patel, B. J. Boersma, and R. Pecnik. The influence of near-wall density and viscosity gradients on turbulence in channel flows. *Journal of Fluid Mechanics*, 809:793–820, 2016.
- [130] A. E. Perry and M. S. Chong. On the mechanism of wall turbulence. *Journal of Fluid Mechanics*, 119:173–217, 1982.
- [131] A. E. Perry and I. Marusic. A wall-wake model for the turbulence structure of boundary layers. Part 1. Extension of the attached eddy hypothesis. *Journal of Fluid Mechanics*, 298:361–388, 1995.
- [132] M. R. Petersen and D. Livescu. Forcing for statistically stationary compressible isotropic turbulence. *Physics of Fluids*, 22(11):116101, 11 2010.

- [133] S. Pirozzoli. An explicit representation for mean profiles and fluxes in forced passive scalar convection. *Journal of Fluid Mechanics*, 968:R1, 2023.
- [134] S. Pirozzoli and M. Bernardini. Turbulence in supersonic boundary layers at moderate Reynolds number. *Journal of Fluid Mechanics*, 688:120–168, 2011.
- [135] S. Pirozzoli, J. Romero, M. Fatica, R. Verzicco, and P. Orlandi. DNS of passive scalars in turbulent pipe flow. *Journal of Fluid Mechanics*, 940:A45, 2022.
- [136] S. B. Pope. *Turbulent Flows*. Cambridge University Press, 2000.
- [137] S. Priebe and M. P. Martin. Direct numerical simulation of a hypersonic turbulent boundary layer on a large domain. In *41st AIAA Fluid Dynamics Conference and Exhibit, Honolulu, Hawaii*, 2012.
- [138] P. Raje, E. Parish, J. P. Hickey, P. Cinnella, and K. Duraisamy. Recent developments and research needs in turbulence modeling of hypersonic flows. *Physics of Fluids*, 37(3):031304, 03 2025.
- [139] Rakhi, M. Klein, J. Medina, and H. Schmidt. One-dimensional turbulence modelling of incompressible temporally developing turbulent boundary layers with comparison to DNS. *Journal of Turbulence*, 20(8):506–543, 2019.
- [140] Rakhi and H. Schmidt. One-dimensional turbulence: Application to incompressible spatially developing turbulent boundary layers. *International Journal of Heat and Fluid Flow*, 85:108626, 2020.
- [141] H. Reichardt. Messungen turbulenter schwankungen. naturwissenschaften. *Jahrg. 26*, Heft 24/25:404, 1938.
- [142] O. Reynolds. An experimental investigation of the circumstances which determine whether the motion of water shall be direct or sinuous, and of the law of resistance in parallel channels. *Philosophical Transactions of the Royal Society of London*, 174:935–982, 1883.

- [143] O. Reynolds. On the dynamical theory of incompressible viscous fluids and the determination of the criterion. [abstract]. *Proceedings of the Royal Society of London*, 56:40–45, 1894.
- [144] L. F. Richardson and P. Lynch. *Weather Prediction by Numerical Process*. Cambridge University Press, 1922.
- [145] W. Rodi and N. N. Mansour. Low reynolds number $k-\epsilon$ modelling with the aid of direct simulation data. *Journal of Fluid Mechanics*, 250:509–529, 1993.
- [146] R. S. Rogallo. *Numerical experiments in homogeneous turbulence*, volume 81315. National Aeronautics and Space Administration, 1981.
- [147] S. Roy, U. Pathak, and K. Sinha. Variable turbulent Prandtl number model for shock/boundary-layer interaction. *AIAA Journal*, 56(1):342–355, 2018.
- [148] J. Rutledge and C. A. Sleicher. Direct simulation of turbulent flow and heat transfer in a channel. Part I: Smooth walls. *International Journal for Numerical Methods in Fluids*, 16(12):1051–1078, 1993.
- [149] S. G. Saddoughi and S. V. Veeravalli. Local isotropy in turbulent boundary layers at high Reynolds number. *Journal of Fluid Mechanics*, 268:333–372, 1994.
- [150] R. C. Schmidt, A. R. Kerstein, and R. McDermott. ODTLES: A multi-scale model for 3d turbulent flow based on one-dimensional turbulence modeling. *Computer Methods in Applied Mechanics and Engineering*, 199(13):865–880, 2010.
- [151] J. Schumacher. Sub-kolmogorov-scale fluctuations in fluid turbulence. *Europhysics Letters*, 80(5):54001, oct 2007.
- [152] J. Schumacher, K. R. Sreenivasan, and P. K. Yeung. Very fine structures in scalar mixing. *Journal of Fluid Mechanics*, 531:113–122, 5 2005.
- [153] J. Seidel, C. Fagley, and T. McLaughlin. Structure identification in turbulent flows for feedback flow control. *Physica Scripta*, 2010(T142):014008, 2010.

- [154] S. Sharma, M. Klein, and H. Schmidt. Features of far-downstream asymptotic velocity fluctuations in a round jet: A one-dimensional turbulence study. *Physics of Fluids*, 34:085134, 2022.
- [155] Z. S. She. Hierarchical structures and scalings in turbulence. In Oluş Boratav, Alp Eden, and Ayse Erzan, editors, *Turbulence Modeling and Vortex Dynamics*, pages 28–52, Berlin, Heidelberg, 1997. Springer Berlin Heidelberg.
- [156] W. Shen, J. Yao, and Y. Yang. Designing turbulence with entangled vortices. *Proceedings of the National Academy of Sciences*, 121(35):e2405351121, 2024.
- [157] X. Shen and Z. Warhaft. Longitudinal and transverse structure functions in sheared and unsheared wind-tunnel turbulence. *Physics of Fluids*, 14(1):370–381, 01 2002.
- [158] C. M. De Silva, N. Hutchins, and I. Marusic. Uniform momentum zones in turbulent boundary layers. *Journal of Fluid Mechanics*, 786:309–331, 12 2015.
- [159] J. Smagorinsky. General circulation experiments with the primitive equations: I. the basic experiment. *Monthly weather review*, 91(3):99–164, 1963.
- [160] G. A. Sod. A survey of several finite difference methods for systems of nonlinear hyperbolic conservation laws. *Journal of computational physics*, 27(1):1–31, 1978.
- [161] P. R. Spalart and S. R. Allamaras. A one-equation turbulence model for aerodynamic flows. *Recherche Aerospaciale*, 1:5–21, 1994.
- [162] K. R. Sreenivasan. On the scaling of the turbulence energy dissipation rate. *The Physics of Fluids*, 27(5):1048–1051, 05 1984.
- [163] K. R. Sreenivasan. On the universality of the Kolmogorov constant. *Physics of Fluids*, 7:2778–2784, 11 1995.
- [164] K. R. Sreenivasan. An update on the energy dissipation rate in isotropic turbulence. *Physics of Fluids*, 10(2):528–529, 02 1998.

- [165] K. R. Sreenivasan and R. A. Antonia. The phenomenology of small-scale turbulence, 1997.
- [166] K. R. Sreenivasan and P. Kailasnath. An update on the intermittency exponent in turbulence. *Physics of Fluids A: Fluid Dynamics*, 5(2):512–514, 02 1993.
- [167] K. R. Sreenivasan and C. Meneveau. Singularities of the equations of fluid motion. *Phys. Rev. A*, 38:6287–6295, Dec 1988.
- [168] C. Stack and R. M. Wagnild. Surface pressure fluctuations induced by a hypersonic turbulent boundary layer on a sharp cone at angle of attack. Technical report, Sandia National Lab. (SNL-NM), Albuquerque, NM (United States), 05 2024.
- [169] V. B. Stephens and D. O. Lignell. One-dimensional turbulence (ODT): Computationally efficient modeling and simulation of turbulent flows. *SoftwareX*, 13:100641, 1 2021.
- [170] A. A. Townsend. *The structure of turbulent shear flow, 2nd edition*. Cambridge University Press, Cambridge, 1976.
- [171] A. Trettel and J. Larsson. Mean velocity scaling for compressible wall turbulence with heat transfer. *Physics of Fluids*, 28(2):026102, 02 2016.
- [172] B. Urhobo and D. Ugwuegbulam. What comes after Moore’s law: A comprehensive review of emerging computing paradigms. *World Journal of Advanced Research and Reviews*, 24:2997–3007, 01 2025.
- [173] W. Van De Water and J. A. Herweijer. High-order structure functions of turbulence. *Journal of Fluid Mechanics*, 387:3–37, 1999.
- [174] E. R. Van Driest. Turbulent boundary layer in compressible fluids. *Journal of the Aeronautical Sciences*, 18(3):145–160, 1951.
- [175] P. S. Volpiani, M. Bernardini, and J. Larsson. Effects of a nonadiabatic wall on hypersonic shock/boundary-layer interactions. *Phys. Rev. Fluids*, 5:014602, Jan 2020.

- [176] T. Von Kármán. Mechanische Ähnlichkeit und turbulenz. *In Proceedings of the 3rd International Congress on Applied Mechanics*, 1930.
- [177] X. Wang, J. Hussong, and S. Jakirlić. Curvature influence on flow and heat transfer in a concentric annulus: Conventional and sensitized Reynolds stress modeling study. *International Journal of Heat and Mass Transfer*, 249:127192, 2025.
- [178] Z. Warhaft. Why we need experiments at high Reynolds numbers. *Fluid Dynamics Research*, 41:021401, 2009.
- [179] T. Wei and W. W. Willmarth. Reynolds-number effects on the structure of a turbulent channel flow. *Journal of Fluid Mechanics*, 204:57–95, 1989.
- [180] D.C. Wilcox. *Turbulence Modeling for CFD*. DCW Industries, 2004.
- [181] X. Wu and P. Moin. Direct numerical simulation of turbulence in a nominally zero-pressure-gradient flat-plate boundary layer. *Journal of Fluid Mechanics*, 630:5–41, 2009.
- [182] X. Xiao, H. A. Hassan, J. R. Edwards, and R. L. Gaffney Jr. Role of turbulent Prandtl numbers on heat flux at hypersonic Mach numbers. *AIAA journal*, 45(4):806–813, 2007.
- [183] V. Yakhot and K. R. Sreenivasan. Anomalous scaling of structure functions and dynamic constraints on turbulence simulations. *Journal of Statistical Physics*, 121:823–841, 12 2005.
- [184] J. Yao and F. Hussain. A physical model of turbulence cascade via vortex reconnection sequence and avalanche. *Journal of Fluid Mechanics*, 883:A51, 2020.
- [185] P. K. Yeung, K. Ravikumar, S. Nichols, and R. Uma-Vaideswaran. GPU-enabled extreme-scale turbulence simulations: Fourier pseudo-spectral algorithms at the exascale using openmp offloading. *Computer Physics Communications*, 306:109364, 2025.

- [186] P. K. Yeung, K. Ravikumar, R. U. Vaideswaran, C. Meneveau, K.R. Sreenivasan, and S. Nichols. Turbulence simulations at grid resolution up to 32768^3 enabled by exascale computing. In *76th Annual Meeting of the Division of Fluid Dynamics*. Bulletin of the American Physical Society, 2023.
- [187] P. K. Yeung, K. R. Sreenivasan, and S. B. Pope. Effects of finite spatial and temporal resolution in direct numerical simulations of incompressible isotropic turbulence. *Physical Review Fluids*, 3:064603, 6 2018.
- [188] P. K. Yeung, X. M. Zhai, and K. R. Sreenivasan. Extreme events in computational turbulence. *Proceedings of the National Academy of Sciences of the United States of America*, 112:12633–12638, 10 2015.
- [189] J. L. Yin, D. Z. Wang, H. Cheng, and W. G. Gu. Assessment of RANS to predict flows with large streamline curvature. *IOP Conference Series: Materials Science and Engineering*, 52(2):022002, dec 2013.
- [190] K. Younes and J. P. Hickey. Mean velocity scaling of high-speed turbulent flows under nonadiabatic wall conditions. *AIAA Journal*, 61(4):1532–1539, 2023.
- [191] M. Yu, B. Li, Q. Zhou, D. Sun, and X. Yuan. Turbulent heat flux and wall heat transfer in hypersonic turbulent boundary layers with wall disturbances. *Aerospace Science and Technology*, 145:108879, 2024.
- [192] C. Zhang, L. Duan, and M. M. Choudhari. Direct numerical simulation database for supersonic and hypersonic turbulent boundary layers. *AIAA Journal*, 56(11):4297–4311, 2018.
- [193] Y. S. Zhang, W. T. Bi, F. Hussain, X. L. Li, and Z. S. She. Mach-number-invariant mean-velocity profile of compressible turbulent boundary layers. *Phys. Rev. Lett.*, 109:054502, Jul 2012.
- [194] J. Zhou, R. J. Adrian, S. Balachandar, and T. M. Kendall. Mechanisms for generating coherent packets of hairpin vortices in channel flow. *Journal of Fluid Mechanics*, 387:353–396, 1999.

- [195] T. Zhou and R. A. Antonia. Reynolds number dependence of the small-scale structure of grid turbulence. *Journal of Fluid Mechanics*, 406:81–107, 2000.

APPENDICES

Appendix A

Algorithms for the reduced-ODT model

This appendix describes the implementation of the algorithms utilized to integrate the equations in Chapter 5. The codes were written in MATLAB R2024a.

A.1 Mean-velocity profile

This code carries out the iterations to find a steady-state mean-velocity profile. The code uses 'y' as the wall-normal direction. We begin by setting up the case in terms of kinematic viscosity (ν), boundary layer thickness (δ_{ac}) and Taylor scale Reynolds number (kt). This is then used to find out u_{τ} and viscous wall unit (δ_{ν}).

```
nu = 5e-5;
deltac = 1;
kt = 1.0e3;

utau = kt*nu/(deltac);
delnu = nu/utau;
```

Initialize the velocity profile. Here, the constants a, b and g are used to define various initial scenarios for the velocity profile. The vector visc provides the velocity profile in viscous region and buffer layer, which is used for velocity values before the start of the region of analysis defined later. The value "val200" is used to provide a notional point at z+ value of 200. Typically, our analysis begins at y=99*delnu and the visc table is useful upto y=99*delnu.

```

a = 5;
b = 11;
g = 6;

val200 = (1/0.41*log(200.0))+5.45; %g*sin(a*200*delnu)+b;
%(1/0.25*log(200.0))+5.45; %4*sin(10*200*delnu)+6.5;
%(1/0.25*log(100.0))+5.45;

visc = [0.001 0.101
0.100000000000000013 0.10198604401502892
0.1264304989484073 0.09677623062107235
0.14782676955877883 0.11887846926210022
0.17162000142216907 0.16671402860661066
0.202094993819108 0.18865839411448823
0.23798150674918608 0.21060275962236905
0.27825594022071265 0.23270499826339688
0.3139883829881841 0.2555966025701759
0.35683638893327674 0.3039057813141367
0.39980834238849017 0.352530706324398
0.4674692909505851 0.42578384010609066
0.5312618643164371 0.499668466420384
0.6167703060931606 0.5219285781945622
0.7059361662912154 0.6212307789460381
0.837219829782166 0.7964699567427627

```

0.9582558549602653 0.870196709923906
1.07365363185358 0.9955479776451627
1.211527658628589 1.1463168198036044
1.416558674495616 1.3218717438666285
1.60986746486779 1.4980581604622525
1.8037354444652878 1.70013577089451
2.03536346824042 1.9276309557639484
2.313116629544072 2.2828455053518986
2.5733201883099692 2.5106564364876376
2.8627941656659495 2.7640428151937098
3.0736493532164832 2.992643111995201
3.3472747235998144 3.272078557671057
3.671257230035043 3.525780682643428
3.969770792519964 3.8565248965930974
4.292556788507616 4.187269110542767
4.708033085553415 4.466546683085474
4.983458708779379 4.79776451643459
5.312618643164365 5.052098133939563
5.703912300886461 5.383000221022384
6.0806585545255025 5.662909286097688
6.390804841860306 6.071011335290959
6.81292069057961 6.42764674307726
7.472342848526841 6.860377001041963
7.965894822257484 7.293738751539262
8.49204615012796 7.5736478166145655
8.861982012601525 7.981907738940985
9.447320346528107 8.33854314672729
10.435626297753902 8.898992769410498
11.2042480752502 9.40892298948565
12.28870652992936 9.841653247450346

```

13.287913432286864 10.32585014682201
14.470842848333056 10.73316283034953
15.759080145144576 11.24277730415838
17.16200014221688 11.701240882826557
19.22873070608773 12.235799311673137
21.391779510618306 12.770515613652865
24.138820729041992 13.279340721795963
27.04573356921785 13.813899150642536
29.037750072735033 14.144801237725362
32.76665426700715 14.47459821287613
35.430943387348236 14.626314293833476
200.0          val200];

```

Define the smallest eddy size $l1$ and largest eddy size $l2$ (which is same as δ_{tac}). Define arrays to perform integration. The array l includes all eddy sizes, the array y starts after the viscous region. Array yt starts from very close to the wall, all the way to the boundary layer edge. Then we define the elements dy , dyt and dl to be used for integration.

```

l1 = 99*delnu;
l2 = 1;

l = linspace(l1,l2,10000);
y = linspace(l1,l2,10000);
yt = linspace(delnu,l2,20000);

dy =y(1,2)-y(1,1);
dyt = yt(1,2)-yt(1,1);
dl =l(1,2)-l(1,1);

```

We define the vectors that hold the values of velocity derivative $dudy$, $ysim$ as a variable

for integration, pl as the probability vector for all eddy sizes. The vectors vit and vi hold the velocity values in the analysis region with and without the viscous region, respectively.

```
dudy = zeros(1,length(y));
ysim = zeros(1,length(y));
vi = zeros(1,length(y));
vit = zeros(1,length(yt));
pl = zeros(1,length(l));
```

Initialize the velocity profile and the turbulence intensity parameter C.

```
C=2.0;
for i=1:length(y)
vi(1,i) = (1/0.41*log(y(1,i)/delnu))+5.45;
%g*sin(a*y(1,i))+b; %(1/0.25*log(y(1,i)/delnu))+5.45;
%4*sin(10*y(1,i))+6.5; %(1/0.41*log(y(1,i)/delnu))+1;
end
vi = vi*utau;

for i=1:length(yt)
vit(1,i) = (1/0.41*log(yt(1,i)/delnu))+5.45;
%g*sin(a*yt(1,i))+b; %(1/0.25*log(yt(1,i)/delnu))+5.45;
% 4*sin(10*yt(1,i))+6.5; %(1/0.41*log(y(1,i)/delnu))+1;
end
vit = vit*utau;

% vio = vi;
```

Identify the element of yt which matches with the starting point of y. Then, substitute the velocity profile in the region where yt is less than the first element of y using the velocity data for the viscous and buffer region from visc.

```

        for p=1:length(yt)
        if (yt(1,p)>=y(1,1))
            yt1 = p;
            break;
        end
    end
end

```

```

vit(1,1:yt1) = interp1(visc(:,1)*delnu,visc(:,2)*utau,yt(1,1:yt1));
% plot(yt,vit)
% hold on

```

The main iteration loop starts here.

```

        for iter=1:10
% Initialize vii using the evolved velocity profile vi
vii = vi;
vit(1,yt1+1:end) = interp1(y,vi,yt(1,yt1+1:end));

%-----find probability of eddy : p(1) for velocity profile
%in current iteration.-----
ptot = 0;    % Total probability

% A loop over the eddy sizes to compute probability density
for k=1:length(l)
lk = l(1,k);    % Eddy size considered

% Locate the upper limit of yt where the eddy reaches
for p=1:length(yt)

```

```

    if (yt(1,p)>=lk+yt(1,1))
        yup = p;
        break;
    end
end
% Integrate vit*(2y-1)dy inside the eddy region, where the
% eddy starts at first element of yt, which is at the wall.
integ = 0;
for j=1:yup
    integ = integ + (vit(1,j)*(2*(yt(1,j)-yt(1,1))-lk))*dyt;
end
integ = abs(integ);
% Multiply the constants with the probability expression.
pl(1,k) = integ*(4/9/lk^3);
ptot=ptot+pl(1,k);
end
%-----
% Normalize probability using the total probability
pl = pl/ptot/dl;
% plot(1,pl)
% hold on

% Begin computing dudy using equation (3.14), note the constant C
for i=1:length(y)
    dudy(1,i) = 0.0;

% The index for k starts from i - thus, only the eddies
%that reach the current y location are considered.
for k=i:length(l)

```

```

lk = l(1,k);

const = C^1/(lk)*(4/9/lk^1);
dudy(1,i) = dudy(1,i) + const*vi(1,i)*(2*(y(1,i)-yt(1,1))-lk)*pl(1,k)*dl;
end

end

% With the obtained dudy, integrate dudy to find the velocity profile.

ysim(1,1) = vi(1,1);
for i=1:length(y)-1
ysim(1,i+1) = ysim(1,i)+dudy(1,i)*dy;
end
vi = ysim;
% Substitute the obtained velocity profile vsim into vi.

end

Plot the velocity profile from final and second last iteration to see the convergence.

    semilogx(y/delnu,vii/utau)
hold on
semilogx(y/delnu,vi/utau)

xlabel('y+')
ylabel('<u_1>/U_\tau')

```

A.2 Reynolds normal stresses

This code carries out the iterations to find a steady-state Reynolds normal stress profile. The code uses 'y' as the wall-normal direction.

The first few steps are identical to the procedure for computing mean-velocity profile. We begin by setting up the case in terms of kinematic viscosity (ν), boundary layer thickness (δ^*) and Taylor scale Reynolds number (kt). This is then used to find out u^+ and viscous wall unit (δ^+). Initialize the velocity profile. The vector `visc` provides the velocity profile in viscous and buffer region, which is used for velocity values before the start of the region of analysis defined later. The value "val200" is used to provide a notional point at z^+ value of 200. Typically, our analysis begins at $y=99\delta^+$ and the `visc` table is useful upto $y=99*\delta^+$.

Define the smallest eddy size l_1 and largest eddy size l_2 (which is same as δ^*). Define arrays to perform integration. The array `l` includes all eddy sizes, the array `y` starts after the viscous region. Array `yt` starts from very close to the wall, all the way to the boundary layer edge. Then we define the elements `dy`, `dvt` and `dl` to be used for integration.

```
l1 = 20*delnu;
l2 = fact*deltac;

l = linspace(l1,l2,10000);
y = linspace(l1,l2,10000);
yt = linspace(delnu,l2,20000);

dy =y(1,2)-y(1,1);
dvt = yt(1,2)-yt(1,1);
dl =l(1,2)-l(1,1);
```

We define the vectors that hold the values of induced normal stress as `vpr`, `pl` as the

probability vector for all eddy sizes. The vectors vit and vi hold the velocity values in the analysis region with and without the viscous plus buffer region, respectively.

```
vpr = zeros(1,length(yt));  
% vprt = zeros(1,length(yt));  
vi = zeros(1,length(y));  
vit = zeros(1,length(yt));  
pl = zeros(1,length(1));
```

Initialize the velocity profile and the constant C.

```
for i=1:length(y)  
vi(1,i) = (1/0.41*log(y(1,i)/delnu))+5.45;  
end  
vi = vi*utau;  
  
for i=1:length(yt)  
vit(1,i) =(1/0.41*log(yt(1,i)/delnu))+5.45;  
end  
vit = vit*utau;  
  
C = 0.1;
```

Identify the element of yt which matches with the starting point of y. Then, substitute the velocity profile in the region where yt is less than the first element of y using the velocity data from visc.

```
for p=1:length(yt)  
if (yt(1,p)>=y(1,1))  
yt1 = p;  
break;
```

```

    end
end

vit(1,1:yt1) = interp1(visc(:,1)*delnu,visc(:,2)*utau,yt(1,1:yt1));
% semilogx(yt/delnu,vit/utau)

Find the probability for eddy size l.

    ptot = 0;
%-----find probability of eddy : p(l) for velocity profile
%in current iteration.-----
for k=1:length(l)
lk = l(1,k);
for p=1:length(yt)
    if (yt(1,p)>=lk+yt(1,1))
        yup = p;
        break;
    end
end
end

integ = 0;
for j=1:yup
    integ = integ + (vit(1,j)*(2*(yt(1,j)-yt(1,1))-lk))*dyt;
end
integ = abs(integ);
pl(1,k) = integ*(4/9/lk^3);
ptot=ptot+pl(1,k);
end
%-----
pl = pl/ptot/dl;
% plot(1,pl)

```

```
% hold on
```

Find the induced normal stress at location y and integrate the effect over all relevant eddies.

```
    for i=1:length(yt)
```

```
vpr(1,i) = 0.0;
```

```
% -----
```

```
% Identify the largest eddy size
```

```
lup = fact*deltac-yt(1,1);
```

```
% Identify the range of eddies that will impact the current y location--
```

```
for p=1:length(l)
```

```
    if (l(1,p)>=yt(1,i))
```

```
        llo = p;
```

```
        break;
```

```
    else
```

```
        llo = 1;
```

```
    end
```

```
end
```

```
for p=1:length(l)
```

```
    if (l(1,p)>=lup)
```

```
        lhi = p;
```

```
        break;
```

```
    else
```

```
        lhi = length(l);
```

```
    end
```

```
end
```

```
%-----
```

```

%Compute the induced normal stresses at each y location
%using the eddies identified above.
for k=llo:lhi
lk = l(1,k);

del2 = 0;
if (yt(1,i)<yt(1,1)+1/3*lk)
    del2 = 3*(yt(1,i)-yt(1,1));
elseif(yt(1,i)>=yt(1,1)+1/3*lk && yt(1,i)<yt(1,1)+2/3*lk)
    del2 = 2*lk-3*(yt(1,i)-yt(1,1));
elseif(yt(1,i)>=yt(1,1)+2/3*lk && yt(1,i)<yt(1,1)+3/3*lk)
    del2 = -2*lk+3*(yt(1,i)-yt(1,1));
end

vpr(1,i) = vpr(1,i) + C*(del2)^2*pl(1,k)^3*d1;

end
%-----
end

Plot the normal stress profile.

semilogx(yt/delnu,sqrt(vpr)/utau)
xlabel('y+')
ylabel('<u_3^2>^{1/2}/U_\tau')

```

A.3 Reynolds shear stresses with attached eddies

This code carries out the iterations to find a steady-state Reynolds shear stress profile using only wall-attached eddies. The code uses 'y' as the wall-normal direction. We begin by setting up the case in terms of kinematic viscosity (ν), boundary layer thickness (δ_{ac}) and Taylor scale Reynolds number (kt). This is then used to find out u_{τ} and viscous wall unit (δ_{ν}). Initialize the velocity profile. The vector `visc` provides the velocity profile in viscous and buffer region, which is used for velocity values before the start of the region of analysis defined later. The value "val200" is used to provide a notional point at $z+$ value of 200. Typically, our analysis begins at $y=99\delta_{\nu}$ and the `visc` table is useful upto $y=99*\delta_{\nu}$.

Define the smallest eddy size $l1$ and largest eddy size $l2$ (which is same as δ_{ac}). Define arrays to perform integration. The array `l` includes all eddy sizes, the array `y` starts after the viscous region. Array `yt` starts from very close to the wall, all the way to the boundary layer edge. Then we define the elements `dy`, `dyt` and `dl` to be used for integration.

```
l1 = 99.0*delnu;
l2 = fact*deltac;

l = linspace(l1,l2,5000);
yt = linspace(0.1*delnu,l2,10000);

dyt = yt(1,2)-yt(1,1);
dl =l(1,2)-l(1,1);
```

We define the vectors that hold the values of induced velocity change by eddies as `vpr`, integration of `vpr` in `vprrt`, `pl` as the probability vector for all eddy sizes. The vectors `vit` and `vi` hold the velocity values in the analysis region with and without the viscous plus buffer region, respectively. The array `tim` holds the net time duration to be considered for all eddies at location `y`.

```

        vpr = zeros(1,length(yt));
vpri = zeros(1,length(yt));

tim = zeros(1,length(yt));
vit = zeros(1,length(yt));
pl = zeros(1,length(1));

```

Initialize the velocity profile and the constant C.

```

C=0.05;

for i=1:length(yt)
vit(1,i) = (1/kap*log(yt(1,i)/delnu))+6;
end

vit = vit*utau;

```

Identify the element of yt which matches with the starting point of y. Then, substitute the velocity profile in the region where yt is less than the first element of y using the velocity data from visc.

```

        for p=1:length(yt)
        if (yt(1,p)>=l1)
            yt1 = p;
            break;
        end
end
end

```

```

vit(1,1:yt1) = interp1(visc(:,1)*delnu,visc(:,2)*utau,yt(1,1:yt1));
% semilogx(yt/delnu,vit/utau)

```

Find the probability for eddy size l.

```

    ptot = 0;
%-----find probability of eddy : p(l) for velocity profile
%in current iteration.-----
for k=1:length(l)
lk = l(1,k);
for p=1:length(yt)
    if (yt(1,p)>=lk+yt(1,1))
        yup = p;
        break;
    end
end
end

integ = 0;
for j=1:yup
    integ = integ + (vit(1,j)*(2.0*(yt(1,j)-yt(1,1))-lk))*dyt;
end
integ = abs(integ);
pl(1,k) = integ*(4/9/lk^3);
ptot=ptot+pl(1,k);
end
%-----
pl = pl/ptot/dl;
% plot(1,pl)
% hold on

```

Find the induced velocity change at location y and integrate the effect over all relevant eddies.

```
    for i=1:length(yt)
vpr(1,i) = 0.0;
% tim keeps track of net duration of eddies applied at each y location
tim(1,i) = 0.0;
% -----
% Identify the largest eddy size

lup = fact*deltac-yt(1,1);

% Identify the range of eddies that will impact the current
%y location-----
for p=1:length(l)
    if (l(1,p)>=yt(1,i))
        llo = p;
        break;
    else
        llo = 1;
    end
end

for p=1:length(l)
    if (l(1,p)>=lup)
        lhi = p;
        break;
    else
        lhi = length(l);
    end
end
end
```

```

%-----
%Compute the induced normal stresses at each y location
%using the eddies identified above.
for k=llo:lhi
lk = l(1,k);

const = 1/(lk^2)*(4/9);

vpr(1,i) = vpr(1,i) + C*const*(vit(1,i)*(-2*(yt(1,i)-
yt(1,1))+lk))^1*pl(1,k)*dl; %const*abs(vi(1,i)*(2*(yt(1,i)-
yt(1,1))-lk))*

end

% To get a net duration of eddies at y, we multiply the
%p(1)^1/tau(1), with tau(1), thus giving unity with dl.
for k=1:length(l)
tim(1,i) = tim(1,i) + 1*dl;
end

end

% Integrate the velocity change induced by eddies upto the
%location y.-----
for i=1:length(yt)
vprt(1,i) = 0.0;

for pp=1:i
vprt(1,i) = vprt(1,i)+vpr(1,pp)*dyt;

```

```
end
end
```

Plot the shear stress profile.

```
plot(yt/deltac,(vpvt./tim)/utau^2)

xlabel('y/\delta_c')
ylabel('-<u_1u_3>/u^2_\tau')
```

A.4 Reynolds stresses with both attached and detached eddies included

This code carries out the iterations to find a steady-state Reynolds shear stress profile using both attached and detached eddies. The code uses 'y' as the wall-normal direction. We begin by setting up the case in terms of kinematic viscosity (ν), boundary layer thickness (δ_{tac}) and Taylor scale Reynolds number (kt). This is then used to find out u_{τ} and viscous wall unit (δ_{ν}).

Initialize the velocity profile. The vector `visc` provides the velocity profile in viscous region, which is used for velocity values before the start of the region of analysis defined later. The value "val200" is used to provide a notional point at $z+$ value of 200. Typically, our analysis begins at $y=99\delta_{\nu}$ and the `visc` table is useful upto $y=99*\delta_{\nu}$.

Define the smallest eddy size $l1$ and largest eddy size $l2$ (which is same as δ_{tac}). Define arrays to perform integration. The array `l` includes all eddy sizes, the array `y` starts after the viscous and buffer region. Array `yt` starts from very close to the wall, all the way to the boundary layer edge. Then we define the elements `dy`, `d yt` and `dl` to be used for integration.

```

l1 = 99.0*delnu;
l2 = fact*deltac;

l = linspace(l1,l2,1000);
yt = linspace(0.1*delnu,l2,2000);

dyt = yt(1,2)-yt(1,1);
dl = l(1,2)-l(1,1);

```

We define the vectors that hold the values of induced velocity change by eddies as *vpr*, integration of *vpr* as *vpri*, *pl* as the probability vector for all eddy sizes. The vectors *vit* and *vi* hold the velocity values in the analysis region with and without the viscous plus buffer region, respectively. The array *tim* holds the net time duration to be considered for all eddies at location *y*.

```

vpr = zeros(1,length(yt));
vpri = zeros(1,length(yt));

tim = zeros(1,length(yt));
vit = zeros(1,length(yt));
pyl = zeros(length(yt),length(l));

```

Initialize the velocity profile and the constant *C*.

```

C=0.015;

for i=1:length(yt)
vit(1,i) = (1/kap*log(yt(1,i)/delnu))+6;
end

```

```
vit = vit*utau;
```

```
% re_theta = vit(1,end)*2*deltac/nu;
```

Identify the element of yt which matches with the starting point of y. Then, substitute the velocity profile in the region where yt is less than the first element of y using the velocity data from visc.

```
for p=1:length(yt)
    if (yt(1,p)>=l1)
        yt1 = p;
        break;
    end
end
```

```
% vit(1,1:yt1) = interp1(visc(:,1)*delnu,visc(:,2)*utau,yt(1,1:yt1));
% semilogx(yt/delnu,vit/utau)
```

Find the probability for eddy size l and start location yin.

```
ptot = 0;
%-----find probability of eddy : p(l) for velocity profile
%in current iteration.-----
for yin=1:length(yt)
    lup = fact*deltac-yt(1,yin);
    if lup<l1
        break;
    end

    for p=1:length(l)
```

```

        if (l(1,p)>lup)
            ilup = p;
            break;
        else
            ilup = length(l);
        end
    end
end

for k=1:ilup
    lk = l(1,k);
    y1 = yt(1,yin);

    for p=1:length(yt)
        if (yt(1,p)>(y1+lk))
            yup = p;
            break;
        else
            yup = length(yt);
        end
    end
end

integ = 0.0;
for j=yin:yup
    integ = integ + (vit(1,j)*(2*(yt(1,j)-y1)-lk))*dyt;
end
integ = abs(integ);

pyl(yin,k) = integ*(4/9/lk^3);

```

```

        ptot=ptot+pyl(yin,k);

    end
end
%-----
pyl = pyl/ptot/(dl*dyt);

% [L,Yt] = meshgrid(1,yt);

% pcolor(L,Yt,pyl)
% axis([l1 1 delnu 0.25])
% xlabel('l')
% ylabel('y')
% shading interp
% colorbar

Find the induced velocity change at location y and integrate the effect over all relevant
eddies.

for i=1:length(yt)

    vpr(1,i) = 0.0;
    % tim keeps track of net duration of eddies applied at each y location
    tim(1,i) = 0.0;

    % -----
    % % Identify the range of eddies that will impact the
    %current y location-----

```

```

for xst = 1:i
    lup = fact*deltac-yt(1,xst);
    % Since the eddy is detached here in general, we need
    %to find what is the shortest size of the eddy to be
    %considered considering the current eddy start location.
    for p=1:length(l)
        if (l(1,p)+yt(1,xst)>=yt(1,i))
            llo = p;
            break;
        else
            llo = 1;
        end
    end
end

for p=1:length(l)
    if (l(1,p)>=lup)
        lhi = p;
        break;
    else
        lhi = length(l);
    end
end

end

%-----
%Compute the induced normal stresses at each y location
%using the eddies identified above.

for k=llo:lhi
    lk = l(1,k);

```

```

const = 1/(lk^2)*(4/9);

vpr(1,i) = vpr(1,i) + C * const*(vit(1,i)*(2*(yt(1,i)-
yt(1,xst))-lk))^1*pyl(xst,k)*dl;

end

% To get a net duration of eddies at y, we multiply the
%p(1)~1/tau(1), with tau(1), thus giving unity with dl.
for k=1:length(l)
tim(1,i) = tim(1,i) + 1*dl;
end

end

end

for i=1:length(yt)
vprt(1,i) = 0.0;

for pp=1:i
vprt(1,i) = vprt(1,i)+vpr(1,pp)*dyt;
end
end

Plot the shear stress profile.

plot(yt/delnu,-(vprt./tim)/utau^2)

```

```
xlabel('y/\delta_c')  
ylabel('-<u_1u_3>/u^2_\tau')
```